



INSTITUTO
SUPERIOR
TÉCNICO

UNIVERSIDADE TÉCNICA DE LISBOA
INSTITUTO SUPERIOR TÉCNICO

OIL SPILL DETECTION
USING SAR IMAGES

Sónia Antunes Pelizzari
(Licenciada)

Dissertação para obtenção do Grau de Doutor em
Engenharia Electrotécnica e de Computadores

Orientador: Doutor José Manuel Bioucas Dias

Júri

Presidente	Presidente do Conselho Científico do IST
Vogais	Doutor Paulo Alexandre Carapinha Marques
	Doutor Jorge dos Santos Salvador Marques
	Doutor Mário Alexandre Teles de Figueiredo
	Doutor José Manuel Bioucas Dias
	Doutor André Ribeiro da Silva de Almeida Marçal

Fevereiro 2011

Resumo:

A presente dissertação descreve uma metodologia para a detecção automática de derrames de hidrocarbonetos no oceano, utilizando imagens de Radar de Abertura Sintética (SAR) e foi desenvolvida no contexto do projecto “Detecção de Derrames de Hidrocarbonetos Utilizando Dados ASAR/MERIS”, financiado em parte pela Fundação para a Ciência e Tecnologia e em parte pela Agência Espacial Europeia.

O trabalho inclui o desenvolvimento e teste de uma série de algoritmos de segmentação e classificação, bem como a avaliação do seu desempenho numa base de dados de derrames, criada utilizando imagens SAR adquiridas sobre a Europa pelo satélite Envisat.

Os métodos de segmentação seguem uma abordagem bayesiana e utilizam um “prior” logístico multi-nível. A sua utilidade para segmentar assinaturas de SAR em geral e de derrames em particular é demonstrada. A possibilidade de utilizar os algoritmos noutro tipo de dados, nomeadamente imagens espectrais de média resolução é também ilustrada.

São testados diferentes classificadores e feita uma comparação dos resultados obtidos. A classificação inclui procedimentos de selecção de características, sendo consideradas duas aproximações diversas: selecção por filtragem e embebida.

A metodologia apresentada foi desenvolvida tendo como foco a sua aplicabilidade operacional, em estreita colaboração com a indústria espacial nacional.

Palavras-chave:

SAR, derrame, hidrocarboneto, segmentação, classificação, abordagem bayesiana

Abstract:

The present thesis describes a methodology for automatic detection of oil spills in the ocean using “Synthetic Aperture Radar” (SAR) images and was part of a project named “Oil Slick Surveillance Using ASAR/MERIS Data”, supported by the Portuguese “Fundação para a Ciência e Tecnologia” and by the European Space Agency.

A number of segmentation and classification algorithms is developed and tested and a complete processing chain is evaluated over an oil spill database, created on basis of a sample of SAR images over Europe, from the Envisat satellite.

The segmentation methods are developed under a Bayesian framework adopting a multi-level logistic prior. Their capability for segmenting SAR signatures in general and oil spills in particular is demonstrated. Furthermore, the possibility of using the proposed algorithms for other image types, like “Medium Resolution Imaging Spectrometer Instrument” (MERIS) images, is also illustrated.

Regarding the classification, a number of different classifiers are tested and a comparison among the delivered results for oil spill detection is given. The classification includes feature selection and two approaches are exploited: filter and embedded selection.

The presented methodology was developed with a focus on its operational applicability and in close cooperation with the national space industry.

Key Words:

SAR, oil, spill, segmentation, classification, Bayesian approach

I would like to dedicate this work to my family, which has given me their full support for the duration of this PhD: to my husband and children for their understanding, and especially to my parents, who encouraged me to continue my education and who demonstrated to me throughout their lives, the importance of hard work.

I would also like to dedicate this work to my grandmother, who regretted so much the fact that she did not have the chance to finish primary school. She was one of the most intelligent persons I have ever known.

Acknowledgements

The author wishes to express her gratitude to her supervisor, Prof. Dr. José Bioucas Dias, who helped and offered invaluable assistance, support and guidance. The author would also like to acknowledge V. Kolmogorov for the max-flow code made available to be used in the Graph-Cut and α -Expansion segmentation techniques and S. Kumar for the Loopy Belief Propagation code used for computing the two-node beliefs in the Loopy- β -Estimation EM algorithm.

The author would also like to convey thanks to the European Space Agency and “Fundação para a Ciência e Tecnologia” for partially supporting the work, as well as to the Edisoft S.A. company for the provided data and cooperation.

Furthermore, my gratitude for the advices and suggestions from Dr. Attilio Gambardella, in the classification part of this work.

Finally a special thank also to the thousands of individuals who have coded for the LaTeX project for free. It is due to their efforts that we can generate professionally typeset PDFs now.

Contents

List of Figures	vii
List of Tables	xi
1 Introduction	1
1.1 Problem Statement	1
1.2 State-of-the-Art	7
1.3 Aims and Contributions	16
1.4 Thesis Structure	18
2 Data and Methodology	19
2.1 SAR data	19
2.2 SAR missions and products	23
2.2.1 SAR Sensing of the Ocean	27
2.3 Data Set	30
2.3.1 Data Set for Segmentation	30
2.3.2 Data Set for Classification	31
2.4 Methodology	39
2.4.1 Process Chain	39
2.4.2 Extracted Features	42
3 Segmentation	47
3.1 Introduction	47
3.2 Problem Formulation	48
3.2.1 Bayesian Approach	48
3.2.2 Observation Model	49

CONTENTS

3.2.3	Prior	50
3.2.4	Maximum a Posteriori Estimate	51
3.2.5	Energy Minimization	52
3.3	EM Algorithm for Fitting a Mixture of Gamma Densities	53
3.4	Estimation of Parameter β	55
3.4.1	Least Squares Fit	55
3.4.2	Coding Method	56
3.4.3	Loopy- β -Estimation	56
3.4.4	A few Remarks about the Vector of Parametres ϕ	59
3.5	Supervised Segmentation	59
3.6	Unsupervised Segmentation	60
3.7	Results	61
3.7.1	Simulations	62
3.7.1.1	Segmentation Results with Gamma Data Term	62
3.7.1.2	EM Algorithm for Gamma Mixture	65
3.7.2	Real Images	65
3.7.2.1	Segmentation of an ERS-1 image using Algorithm-1	71
3.7.2.2	Segmentation of MERIS/ASAR pair using Algorithm-1	72
3.7.2.3	Segmentation of an ERS-1 image using Algorithm-2 and -3	73
3.7.2.4	Segmentation of an Envisat ASAR IM image using Algorithm- 2 and -3	77
3.7.2.5	Segmentation of an Envisat ASAR WSM image using Algorithm-3	78
3.7.2.6	Computational Complexity	84
4	Classification	85
4.1	Lookalikes: an Overview	85
4.2	Classification Methods	88
4.2.1	AP1	91
4.2.2	AP2	96
4.3	Experimental Results	97
4.3.1	Examples of Extracted Features	97

CONTENTS

4.3.2	AP1	99
4.3.2.1	With Wind	101
4.3.2.2	Without Wind	103
4.3.3	AP2	103
4.3.3.1	With Wind	106
4.3.3.2	Without Wind	106
5	Conclusions	111
5.1	Conclusions on Proposed Methodology for Oil Spill Detection	111
5.2	Perspectives on Oil Spill Detection	113
6	Acronyms	115
	Bibliography	117

CONTENTS

List of Figures

1.1	Oil spill detection principle	2
1.2	Example of oil spill signature in a SAR image	5
1.3	Wind shelter effect in Envisat ASAR_WSM image	5
1.4	Correlation MERIS/SAR signatures	6
1.5	Oil spill detection: block structure	8
1.6	Confusion matrix	10
1.7	European funded projects related to oil spill detection	15
2.1	Frequency bands used in radar systems	20
2.2	Side looking geometry	22
2.3	Concept of real aperture versus synthetic aperture radar	22
2.4	Side looking geometry (cont.)	23
2.5	Envisat satellite and SAR antenna	24
2.6	polarisation modes	24
2.7	Envisat modes for oil spill detection	25
2.8	Relevant SAR missions	26
2.9	Bragg scattering	28
2.10	Two-scale approximation theory	29
2.11	GUI of EOLI-SA	31
2.12	Location of SAR images used for classification	34
2.13	Example of SAR wind field	35
2.14	Wind sample data from the Portuguese Meteorological Institute.	37
2.15	MS Access database for classification	38
2.16	Envisat ASAR_WSM_1P image from the Prestige accident	41
2.17	Landmask application to Prestige image	42

LIST OF FIGURES

3.1	8-pixel-neighbourhood and cliques	51
3.2	Lattice representing the pairwise MRF.	58
3.3	Results: different segmentations for image with Gamma data term . . .	63
3.4	OA for images generated using a Gamma data term, with increasing σ values	64
3.5	Results: Gamma data term	66
3.6	Segmentation results for Image A	67
3.7	Segmentation results for Image B	68
3.8	Simulated SAR image	68
3.9	Probability functions used to simulate SAR image	69
3.10	True and estimated class densities for oil	69
3.11	True and estimated class densities for oil	70
3.12	Segmentation of ERS-1 image	71
3.13	Quicklook of MERIS/ASAR pair with oil spill	72
3.14	MERIS image segmentation using Algorithm-1	73
3.15	ASAR image segmentation with Algorithm-1	74
3.16	ERS-1 image from the Sicily Channel, Italy	74
3.17	Closer look to the sub-scenes of the ERS-1 image	75
3.18	Fitting of a mixture of Gammas in an ERS-1 image	75
3.19	Segmentation of ERS-1 subscene using Algorithm-3	76
3.20	Class Parameters Estimation for Algorithm-2.	76
3.21	Segmentation of ERS-1 subscene using Algorithm-2	77
3.22	Segmentation of ERS-1 subscene containing oil, with $\beta = 0$	77
3.23	ASAR image segmentation using Algorithm-2 and Algorithm-3	78
3.24	Prestige: location of the ASAR Envisat image	79
3.25	Prestige: full resolution image	80
3.26	Prestige: segmentation results applying Algorithm-3	81
3.27	Zoom to one tile of the Prestige ASAR image	82
3.28	Prestige: results of applying EM Gamma mixture estimation	82
3.29	Prestige: histogram and superimposed estimated Gamma mixture . . .	83
3.30	Prestige: segmentation results applying Algorithm-3 with 3 classes . . .	83
3.31	Prestige: segmentation results (cont.)	84

LIST OF FIGURES

4.1	SAR image containing bathymetry signatures	86
4.2	Physical origin of the bathymetry structures	87
4.3	SAR image containing upwelling signature	87
4.4	Chlorophyll and SST images correlating with SAR	89
4.5	Biogenic slicks in SAR image	90
4.6	Main steps undertaken in the Classification	95
4.7	Histogram of Length To Width Ratio values	97
4.8	Oil Slick: LWR example	98
4.9	Lookalike: LWR example	98
4.10	Histogram of Intensity Standard Deviation Ratio values	99
4.11	Oil Slick: ISDR example	100
4.12	Lookalike: ISDR example	100
4.13	Histogram of wind values	101
4.14	OA-test for LOGC classifier using wind information	102
4.15	OA-test for LDC classifier using wind information	102
4.16	OA-test for LOGC classifier with no wind	103
4.17	OA-test for LDC classifier with no wind	105
4.18	OA-test and OA-train from SLMR with wind	107
4.19	OA-oil and OA-lookalike from SLMR with wind	108
4.20	OA-falsePositives and OA-falseNegatives from SLMR with wind	108
4.21	Risk versus regularization, with wind	109
4.22	Number of Relevant Features versus regularization, with wind	109
4.23	SMLR: result details	110

LIST OF FIGURES

List of Tables

1.1	Summary of classification techniques proposed in the literature.	11
1.2	Further remarks on classification techniques.	12
2.1	Data Set for Segmentation-Part I.	32
2.2	Data Set for Segmentation-Part II.	33
4.1	Classification Results for AP1 with wind information	101
4.2	AP1 Best Result	104
4.3	Classification Results for AP1 without wind information	105
4.4	AP2 Best Result	107

LIST OF TABLES

1

Introduction

1.1 Problem Statement

This PhD work was developed in the framework of the “Oil Slick Surveillance Using ASAR/MERIS Data” project, supported by the European Space Agency (ESA) under the grant ESA/C1:2422 and by the Portuguese “Fundação para a Ciência e Tecnologia” (FCT) under the grant PDCTE/CPS/49967/2003. The project, in the area of remote sensing oriented for ocean monitoring, is under the coordination of Prof. José Bioucas Dias. Its main scope is the realization of an automatic detector of oil spills using “Synthetic Aperture Radar” (SAR) and “Medium Resolution Imaging Spectrometer Instrument” (MERIS) images, acquired on board of the European satellite Envisat. Hereby, a methodology for automatic detection using SAR images is proposed. The thesis was conducted in close cooperation with a private enterprise, the Portuguese Edisoft S.A., in the space industry field, and the accomplished results are directly applicable by the company in its operational marine activities/services.

The use of SAR data for oceanography is a well-established technique and encompasses applications for wave, wind and currents retrieval, as well as for ice, vessel and pollution detection [1], [2]). In fact, a wide number of oceanic and atmospheric phenomena become visible on SAR images as they are associated with a variable surface current. This current modulates the sea surface roughness and thus the Normalized Radar Cross Section (NRCS) giving rise to typical signatures and making this type of data very appealing for oceanography. Among these phenomena are gravity waves, convective cells, oceanic internal waves, current and coastal fronts, eddies, upwelling

1. INTRODUCTION

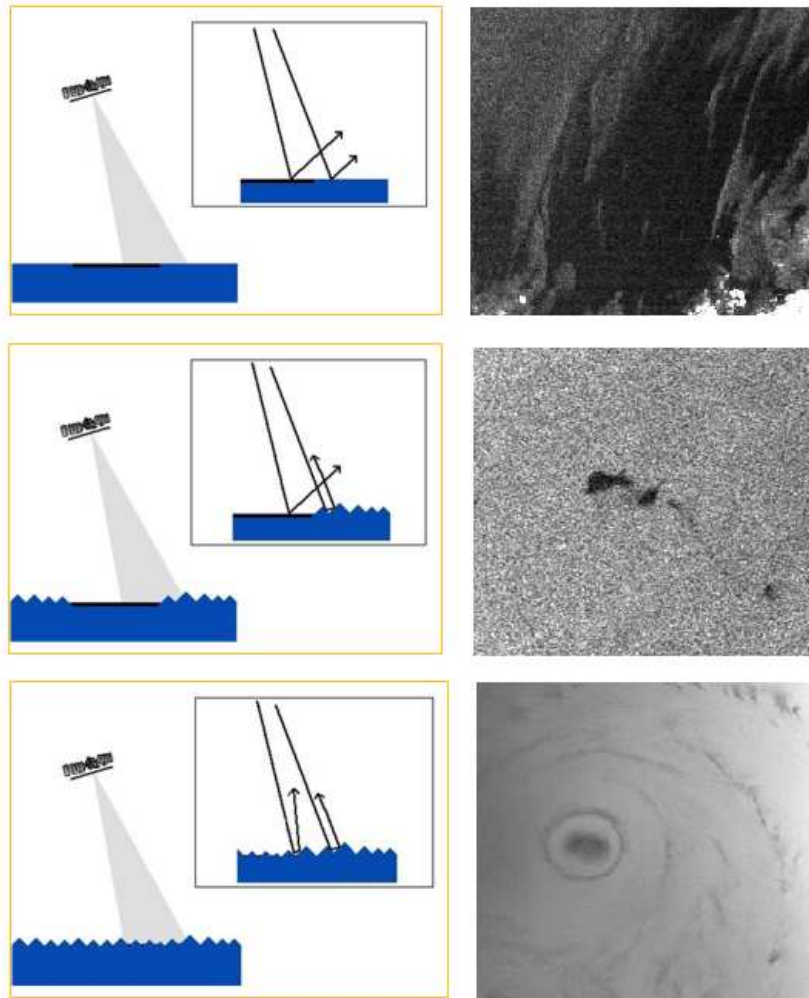


Figure 1.1: Oil spill detection principle using SAR images.

Top Image: no wind \rightarrow almost no energy reflected back to the satellite \rightarrow black images; in this example wind is ≈ 1.5 m/s.

Middle Image: calm winds \rightarrow oil spill detectable \rightarrow gray images; in this example wind is ≈ 8 m/s.

Bottom Image: rough winds \rightarrow more reflection energy returns to the satellite \rightarrow very bright images, no oil signature; in this example wind is \approx between 20 and 40 m/s (Katrina hurricane, copyright ESA).

processes, ship wakes and oil pollution [3].

In the context of pollution, oil spills have been and continue to be of utmost relevance. In fact, these events are one of the main causes of marine and coastal pollution and can be the result of naval accidents or of illegal tank cleaning, although the release of oil may be legal under certain conditions. One institution providing statistics for oil spilt quantities as well as information on major oil spills is the International Tanker Owners Pollution Federation Limited (ITOPF). Although the reports indicate a downward trend in the quantity of spilled oil, it should be taken into consideration that the vast majority of spills are small (i.e. less than 7 tonnes) and data on numbers and amounts is incomplete due to the inconsistent reporting of smaller incidents worldwide [4].

The Portuguese ocean waters are an example of a high risk area due to the great extension of its Exclusive Economic Zone (EEZ) and to the dense ship traffic passing very close to the coast and islands of the country. The need for remote sensing based oil spill monitoring systems was dramatically illustrated during the Prestige accident, where Portugal was involved in the pollution monitoring and combating actions. In special SAR has then proven to be a very effective monitoring tool due to its day-and-night and all-weather imaging capabilities. Moreover, when SAR sensors are on board of a satellite, larger coverage and higher revisit times can also be achieved, when compared for example with airborne systems. Other accidents that have occurred in the Portuguese EEZ or in near proximity were the following: Urquiola in 1976 in La Coruna, Spain; Jakob Maersk in 1975 in Oporto [4]; Cercal in 1994 in Oporto [5] and CPValour in 2005 in Azores [6].

Currently, the European Union (EU) is offering an oil spill monitoring operational system routinely to the European member states and to Norway and Iceland, through the European Maritime Safety Agency (EMSA) (see <http://www.emsa.europa.eu/>). This agency is tasked to contribute to the enhancement of the overall maritime safety system within the EU. The service for oil pollution detection is called CleanSeaNet (CSN) and has been in operation since April 2007. It should be considered in the context of the European program “Global Monitoring for Environment and Security” (GMES), in the marine environment component. The service is based on Envisat and Radarsat-1 and -2 (satellites developed by the Canadian Space Agency (CSA) in collaboration with MDA) images, although SAR data from other satellites can also be

1. INTRODUCTION

used in emergency situations. The detection itself is outsourced to the industry, and is based on semi-automatic procedures, that need the intervention of an human operator [7]. Other operational services for oil spill detection exist, like the one provided by the the Canada Center for Remote Sensing based on the Ocean Monitoring Workstation (OMW) [8]. Furthermore the importance of this issue is well illustrated by the number of recent and ongoing ESA, European, and national funded projects related to the theme (see Section 1.2).

The detection process using SAR images exploits the well-known effect of Bragg scattering of the microwave radiation coming from the sensor mechanisms and inciding on the ocean surface [1]. Envisat and Radarsat satellites operate in C-Band. For this band, the radiation ($\approx 5.6\text{cm}$) interacts with the so-called short gravity ocean waves (wave lengths in the range of 5-7 cm) that are generated by winds blowing over the ocean surface. As consequence of this phenomena, oil spills appear as dark patches in SAR images, under appropriate wind conditions [1]. Figure 1.1 shows the oil spill physical detection principle and Figure 1.2 provides an example of an oil signature on a SAR image. We note that other existing SAR systems use radiation from other bands like the X-Band (ex: TerraSAR-X and Cosmo-SkyMed) and the L-Band (ex: ALOS).

Unfortunately, a number of oceanic and atmospheric phenomena with different origins also produce very similar dark signatures on SAR images, making the detection a complex process and very particular to each concrete ocean region. These phenomena are denominated “lookalikes” and give raise to false alarms [2]. Figures 1.3 and Figure 1.4 provide two examples. A way for better discrimination of lookalikes is to use auxiliary information such as meteorological and oceanic data, like wind and wave, as well as static data layers like bathymetry and electronic nautical charts. Also the fusion with other data types (optical or multispectral), like MERIS images, from Envisat and Moderate Resolution Imaging Spectroradiometer (MODIS) images, from the Terra (EOS AM) and Aqua (EOS PM) satellites, in sun-glint conditions, can in principle be an aid. In the practice however, and in special for operational services, they are not useful due to cloud coverage and low co-location with SAR acquisitions [9].

Due to the intrinsic complexity of the process, in current operational oil spill detection services, the ultimate discrimination between oil spill and lookalike is left to the responsibility of experienced operators, thus involving a certain degree of subjectivity.



Figure 1.2: Example of oil spill signature in a SAR image. A ship traveling northward (bright spot at the end of the dark line) discharging oil can be seen. The oil trail is more than 80 km long and disperses in time becoming wider. This is an ERS-1 scene, acquired on the 20th May 1994 at 14:20 UTC over the Pacific Ocean (from [1]).

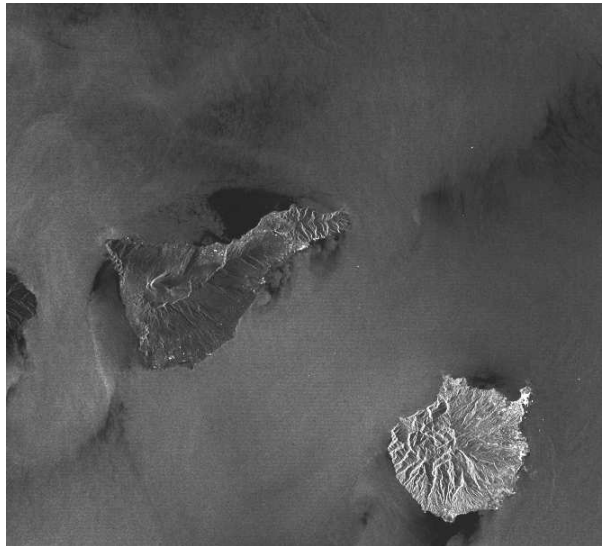


Figure 1.3: In this image, the large dark patches are due to the wind shelter effect behind the islands. This is a part of an Envisat ASAR_WSM scene acquired on the 7th June 2009 at 22:59 over the Canary Islands (courtesy from Edisoft).

1. INTRODUCTION



Figure 1.4: In this image from the 31st October 2002 (copyright ESA) we can see the correlation between the cloud patterns observed in the MERIS image and the signatures observed in the SAR image (see ESA web pages: The power of two - Envisat demonstrates combined imagery from dual sensors).

The operators are aided by graphical tools for selecting the possible oil spills and support their decision in internal guidelines [7]. The guidelines normally consist in a set of empirical rules that evaluate geometrical and intensity features of the patch (like contrast) and auxiliary information (like wind speed) and other contextual information (like vessels or coast proximity). Nevertheless, often operators have to use their “feeling” in complicate scenarios, or unobvious situations, to take a decision if they should report a dark patch as oil spill or not. The process usually also foresees the assignment of a confidence level to the detection.

When considering most existing and proposed oil spill detection systems, normally their processing chain shares a common pipeline structure (see Figure 1.5), differing in the steps undertaken inside each block (example, see [10]). The main blocks in the chain are usually the segmentation and the classification. The segmentation step computes a set of regions defining an image partition, where the features of each region, for example the gray levels, are *similar* in some sense. The classification then focus on the regions with lower backscattering, often using a number of features extracted from these regions including shape, moments, scale parameters, etc. based on which a decision on whether the region corresponds to oil or lookalike is taken.

Although this paradigm seems to be very well established in the field of oil spill detection, some few examples of systems deviating from this structure also exist like for example kernel-based anomaly detectors [11]. Other important typical steps in the chain are the initial pre-processing of data, that may include radiometric normalization and the landmasking. Procedures included in these steps will be later described in detail.

1.2 State-of-the-Art

There have been so far many approaches to the problem of oil spill detection using SAR images. We stress that although SAR data actually contain intensity and phase information, for the special purpose of oil spill detection most proposed methodologies only take intensity into account. Furthermore, although most SAR sensor mechanisms allow the acquisition of dual or even multi-polarisation data, most studies on this subject have been conducted on single-polarisation data. This was in part due to the fact that this type of imagery was more easily available because of planning and acquisition

1. INTRODUCTION

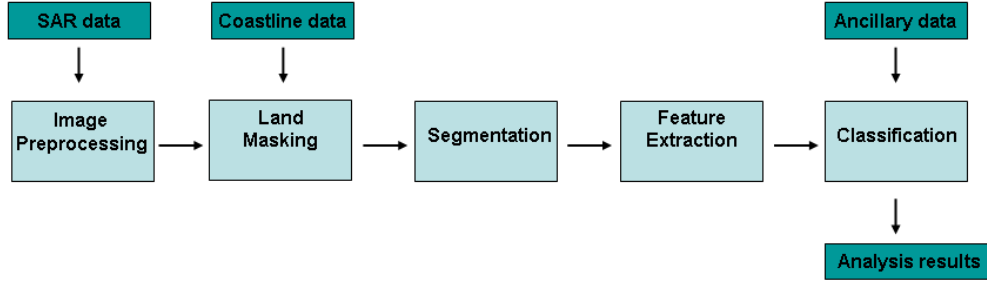


Figure 1.5: Common block structure of most proposed oil spill detection methodologies.

constraints of the SAR instruments. Single polarisation images are also typically characterized by higher radiometric resolution [12]. On the other hand, with the arrival of satellites like Radarsat-2, Terrasar-X and CosmoSkymed, multipolarisation techniques are becoming more relevant. In Sub-section 5.2 we provide some references to up-to-date improvements in the field of oil spill detection methodologies, including also techniques using multi-polarisation data. Finally, a list and summary of the main European funded projects that are directly related with oil spill detection is also given at the end of this section.

A review of SAR segmentation techniques for oil spill detection can be found in [13]. Most approaches to the problem of oil spill segmentation are built on off-the-shelf segmentation algorithms such as the *adaptive image thresholding* and the *hysteresis thresholding*. Entropy methods based on the Maximum Descriptive Length (MDL) and wavelet based approaches have also been proposed. Another recently proposed segmentation methodology applies Hidden Markov Chains (HMC) to a multiscale representation of the original image [14]. Hereby the wavelet coefficients are statistically characterized by the Pearson system and by the generalized Gaussian family. When other SAR products are available, for example polarimetric data, other methods have been described in the literature, like constant false alarm rate filters [15].

An example of an elaborated adaptive thresholding technique is provided by [13]. In this method, an image pyramid is created by averaging pixels in the original image.

From the original image, the next level in the pyramid is created with half the pixel size of the original image. A threshold is then computed for each level based on local estimates of the roughness of the surrounding sea and on a look-up table containing experimental values obtained from a training data set.

Hysteresis thresholding has been used as the base for detecting oil slicks in [16]. The method includes two steps: applying a so-called Directional Hysteresis Thresholding (DHT) and performing the fusion of the DHT responses using a Bayesian operator. The MDL technique, which basically consists in applying information theory in order to find the image description which has the lowest complexity, has been applied in [17] to segment speckled SAR images, namely those containing oil slicks. This segmentation method describes the image as a polygonal grid and determines the number of regions and the location of the nodes that delimit the regions. The two-dimensional wavelet transform, used as a bandpass filter to separate processes at different scales, has also been adopted to oil slick detection in the framework of an algorithm for automated detection and tracking of mesoscale features from satellite imagery. [18]. In spite of the existence of so many different segmentation techniques, in practice only some of them have been applied and tested in the framework of a complete detection process, as we shall see in the remaining of this subsection.

Regarding classification, we refer the recent publications [19] and [20] providing an extensive and deep review on the different used methodologies and correspondent results. The classifiers are evaluated as part of a detection process, in association with a specific segmentation method. In these reviews in fact (and in the relevant literature in general) the reported performance is the one of the whole detection system, including segmentation and classification, and there are not surveys that assess the classification performance per se, decoupling it from the remaining of the chain. Table 1 and Table 2 give an overview of the different classification methods (in the context of a specific detection process) used in oil spill detection that are referred to in the literature. In order to provide a performance measure of the classifier, which is then also considered by extension to be the performance of the whole detection system, normally two Overall Accuracies (OA) are used in the literature: the oil spill detection rate (OA-oil) and the lookalike detection rate (OA-lookalike). Occasionally, the total accuracy (OA-test) is also mentioned. These accuracies are defined by the following expressions, which make

1. INTRODUCTION

	Dark Patch classified as Lookalike	Dark Patch classified as Oil Spill
Dark Patch is Lookalike	Number of True Negative a	Number of False Positive b
Dark Patch is Oil Spill	Number of False Negative c	Number of True Positive d

Figure 1.6: Confusion matrix for the two-class classification case.

use of the entry values a , b , c and d of the so-called confusion matrix, displayed in Figure 1.6:

$$\text{OA-oil} = \frac{d}{\text{nr of oil spills}} \times 100$$

$$\text{OA-lookalike} = \frac{a}{\text{nr of lookalikes}} \times 100$$

$$\text{OA-test} = \frac{a+d}{\text{total nr of dark patches}} \times 100.$$

Furthermore, we also use the false negative and false positive rates defined respectively as:

$$\text{OA-fN} = \frac{c}{\text{nr of oil spills}} \times 100$$

$$\text{OA-fP} = \frac{b}{\text{nr of lookalikes}} \times 100.$$

Table 1.1: Summary of classification techniques proposed in the literature.

Author	Proposed Technique	Data Set Size	OA oil(%)	OA lookalike(%)
Espedal and Walh [21]	Direct analysis + wind history	Three case studies	NA	NA
Kubat et al. [22]	Neural network	41 oil spills + 896 lookalikes	76	86
Solberg et al. [10]	Statistical modeling with rule-based approach	71 oil spills + 6980 lookalikes	94	99
Solberg et al. [23]	[10] + sensor specific rules	37 oil spills + 12110 lookalikes	78	99
Del Frate et al. [24]	MLP neural network	71 oil spills + 68 lookalikes	82	90
Del Frate et al. [25]	[24] + adding wind to network input	111 oil spills + 78 lookalikes	NA	NA
Del Frate et al. [26]	same approach as in [25]	20 dark areas	NA	NA
Fiscella et al. [27]	Mahalanobis classifier	80 oil spills + 43 lookalikes	92	51
Fiscella et al. [27]	Compound probability classifier	80 oil spills + 43 lookalikes	85	67
Marghany [28]	Textural analysis	NA	NA	NA
Nirchio et al. [29]	Fisher discriminant analysis	153 oil spills + 237 lookalikes	74	NA
Nirchio et al. [30]	Fisher discriminant analysis	714 images (not clear how many dark areas)	NA	NA
Girard-Arduin et al. [31]	Ocean backscatter model	NA	NA	
Keramitsoglou et al. [32]	Fuzzi logic classifier	28 images	88	NA
Topouzelis et al. [33]	Multi-scale segmentation + neural network	69 oil spills + 90 lookalikes	91	87
Topouzelis et al. [34]	Combination of neural networks and genetic algorithms	69 oil spills + 90 lookalikes	85	84
Stathakis et al. [35]	Genetic algorithm	69 oil spill + 90 lookalikes	81	88
Gambardella et al. [20]	one-class linear programming method	X-Band: 16 oil spills + 40 lookalikes ERS-SLC: 43 oil spills + 110 lookalikes	98	99

Table 1.2: Further remarks on classification techniques.

Author	Image Type	Remarks
Espedal and Walh [21]	ERS PRI	procedure was foreseen for visual inspection by an operator method is thus not appropriate for automatization wind analysis requires too much time
Kubat et al. [22]	ERS PRI and Radarsat (not clear which type)	no wind information usage
Solberg et al. [10]		method incorporates wind information and information about vessel/platform proximity
Solberg et al. [23]	ASAR-WS and Radarsat (not clear which type)	experimental results only given for ASAR-WS in detail For Radarsat only % of detections of verified oil slicks was provided
Del Frate et al.	ERS-PRI	no wind information used
Del Frate et al. [25]	ERS-PRI	use wind, 3 dark patches out of 60 have been misclassified
Del Frate et al. [26]	ASAR IM	OA-test is 85%, data set very small result indicative of algorithm independence from sensor
Fiscella et al. [27]	ERS-PRI	Author considered a third class: uncertain. Due to this third class it is not very clear how to compute performance of algorithm wind information not used
Marghany [28]	Radarsat Fine Mode	indicative study that showed that texture entropy, energy and homogeneity features provided good detection of oil spills
Nirchio et al. [29]	ERS-PRI	no wind information has been used for the classification
Nirchio et al. [30]	ASA-WSM and ASA-IM	algorithms from [29] have been redesigned for Envisat images and an appropriate incidence angle compensation angle has been applied overall accuracies have not been given, only mentioned they were similar to those for ERS-PRI images
Girard-Arduin et al. [31]	ASA-WSM	only one image was used, as a test case
Keramitsoglou et al. [32]	ERS-PRI	no wind information used
Topouzelis et al. [33]	ERS-PRI	no wind information used
Topouzelis et al. [34]	ERS-PRI	no wind information used feature selection using genetic algorithms
Stathakis et al. [35]	ERS-PRI	
Gambardella et al. [20]	ERS-SLC and X-Band airborne images	feature selection performed no wind information used different one and two-class standard classifiers tested and compared

Although all approaches have surely contributed to the advance of the state-of-the-art in oil spill detection, there are still a number of aspects that can be improved or remain open in this issue, in special in what concerns the operational application of the proposed algorithms. The following conclusions can be drawn by analyzing the state-of-the-art in oil spill detection:

1. Most of the so far proposed methodologies are not completely automatic. In special the segmentation part often requires the specification or tuning of some kind of parameter, on the algorithm itself or as part of the post-processing of the segmentation results before they are further provided to the Classifier.
2. Most of the so far proposed Classifiers have been designed for one special type of SAR images - ERS (a satellite developed by ESA) PRI or ASAR IM, with ≈ 30 m resolution, 100×100 km swath - and experimental results are available for databases of those images. On the other hand, images with other properties in coverage and resolution, namely Envisat ASAR Wide Swath (WS) with ≈ 150 m resolution and 400×400 km swath, have proven to be more adequate for operational purposes.
3. Even though some of the methods have been adapted to Envisat ASAR WS images, the correspondent experimental tests have been carried on a very small dataset, only for preliminary assessment.
4. All the algorithms use features extracted from the dark patches or from its context, but only a few authors [34] and [20] have made an effort to evaluate the effectiveness of the selected features for the classification task. In all the other cases, the feature set has been chosen empirically. Even those authors who adopted feature selection, used an initial feature set that missed some of the features proposed in the literature.
5. Many of the proposed methodologies are not completely automated or are too complex.
6. Only a fraction of the methods use wind information directly, although it is an evidence that wind strongly influences oil spill detection.

1. INTRODUCTION

7. Because the training and evaluation data sets are different for every author, in size and content, it is very difficult to compare the obtained results. One example is the case when oil spills included in a database often occurred near oil platforms or ships. In this scenario a classification method that uses a context feature like “distance to the nearest bright object”, results in accuracies that are surely higher than without such a feature.

For concluding the state-of-the-art survey, a list of the main European projects related to Oil Spill Detection using SAR data is given in Figure 1.7.

Acronym Start/End Date	Description	Prime Contractor	Link
MARCOAST [2005 - 2007]	The main goal of this project was to establish a durable network of marine and coastal information services at the European scale. Two groups of services were covered: Oil Spill Monitoring and Water Quality assessment in coastal areas.	Alcatel Alenia Space, France	http://www.gmesmarcoast.com/
OCEANIDES [2003-2005]	This project aimed at identifying and bringing together the knowledge required to establish a harmonized and effective monitoring and reporting system for illicit marine oil pollution in European waters.	Joint Research Centre, EC	http://oceanides.jrc.cec.eu.int/
DISMAR [2002-2005]	The overall objective was the development of an advanced information system for monitoring and forecasting the marine environment based on a web-based distributed architecture. Analysed data included not only satellite images, but also coastal radar and aerial multi-sensor data. Different supervised and automatic methods have been tested and compared.	Nansen Environmental and Remote Sensing Center	http://www.nersc.no/Projects/dismar/
ROSES [2003-2004]	The primary objective of this project was to build on already existing precursor services to deliver an operational and autonomous European capacity for global monitoring of the marine environment. Oil spill detection and forecasting were included and evaluated over four European areas.	Alcatel Alenia Space, France	http://www.gmesroses.info/
MARSAIS [2001-2003]	In this project, a generic Marine SAR Analysis and Interpretation System (MARSAIS) prototype, containing oil spill detection applications among others, was developed.	Nansen Environmental and Remote Sensing Center	http://marsais.ucc.ie/index.htm
Clean Seas [1997-1999]	This project provided the first statistics on oil spills in Europe, clearly demonstrating the correlation pollution/shipping routes and the severity of the problem.	Satellite Observing System, United Kingdom	http://www.satobsys.co.uk/CSeas/

Figure 1.7: Main European funded projects related with Oil Spill Detection using SAR images.

1.3 Aims and Contributions

In this work, we explore the possibility of using automatic segmentation and classification techniques for operational oil spill detection. By adopting a fully automated process, we aim at obtaining a method free of subjectivity and less time consuming. We conducted experiments on different SAR image types but finally focused on ASAR Wide Swath images, which are currently one of the main input products for operational services due to its coverage properties.

We approached oil spill segmentation using a Bayesian framework and a “Multi-Level Logistic” (MLL) [36] prior. Several methods in the same vein have been proposed since the seminal work of Geman and Geman [37], see *e.g.*, [38]. Applications of these ideas in the segmentation of SAR images can be found, *e.g.*, in [39], [40], [41].

The main contributions of this work to the state-of-art in oil spill segmentation are the following:

- the development of a “Expectation Maximization” (EM) [42] algorithm to estimate the parameters of a mixture of a pre-defined number of Gamma distributions, in order to model the intensities in a SAR image.
- the development of an EM algorithm called “Loopy- β -Estimation”, using “Belief Propagation” (BP) [43] to estimate the smoothness parameter in the “Markov Random Field” (MRF) [36] used as prior in our framework.
- the application of recent graph-cut techniques for solving the energy minimization problem that arises from the followed Bayesian methodology.
- the design of supervised and unsupervised algorithms for oil spill segmentation supported on the referred tools.

The images used for testing the segmentation algorithms mainly came from the FCT/ESA funded project OILSAR.

We then explore different classification methods for oil spill detection using Envisat ASAR WS Images. The classification was then evaluated as part of a complete detection system. For this purpose, a database of oil spills and lookalikes extracted from these type of images, has been built. The used images are from the CSN service and the dark patch extraction was based on the detection CSN reports, produced by Edisoftware.

operators. When building the database we aimed at inserting oil spills and lookalikes corresponding to a maximum of diversity in its features and origins, as found in real scenarios. The implementation of feature extraction routines was also part of the work developed in this PhD. Calibration and radiometric normalization were also undertaken in the processing chain before the classification step.

Moreover, we have made an effort to evaluate the effectiveness of the selected features and also to use a start feature set as complete as possible, including wind information. We also assess the relevance of wind information for the classification process by training and running the classifiers with and without wind information.

We adopted the Leave-One-Out method [44] in order to be able to use the same data set for training and for testing the classifiers.

The main contributions of this work to the state-of-art in oil spill classification are the following:

- As far as we know, these are the first results on automatic oil spill detection using such an extensive sample number of ASAR Wide Swath Images.
- It is also the first time that feature selection methods have been applied to ASAR WSM images and with a so an extended possible start feature set.
- We have also for the first time applied a pre-processing radar normalization technique adapted to ASAR WSM images on a systematic classification study.
- We have tested a new classification approach, namely the “Sparse Multinomial Logistic Regression” (SMLR) algorithm [45] and compared it to state-of-the-art classifiers.

Furthermore, the following articles have been presented/published in conferences, or have been submitted to international journals:

- S. Pelizzari and José M. B. Dias, “Bayesian Adaptive Oil Spill Segmentation of SAR Images via Graph Cuts”, in Proceedings of the SeaSAR, 2006. 17.
- S. Pelizzari and José M. B. Dias, “Oil Spill Segmentation of SAR Images via Graph Cuts”, poster in Confetele 2007.

1. INTRODUCTION

- S. Pelizzari and José M. B. Dias, “Bayesian Oil Spill Segmentation of SAR Images via Graph Cuts”, in Proceedings of the IbPRIA, 2007, vol. 2, pp. 637644. 18.
- S. Pelizzari and José M. B. Dias, “Oil Spill Segmentation of SAR Images via Graph Cuts”, in Proceedings of the IGARSS, 2007, pp. 1318 1321. 18.
- S. Pelizzari and José M. B. Dias, “Bayesian Oil Spill Segmentation of SAR Images”, IEEE Transactions on Geoscience and Remote Sensing, submitted.
- S. Pelizzari and José M. B. Dias, “Operational Automatic Classification of Oil Spills in ASAR-WSM Images”, International Journal of Remote Sensing, submitted.

1.4 Thesis Structure

The contents of this thesis are organized in the following way: Section 1 provides an introduction to the considered problem, containing a review of the state-of-the-art in oil spill detection, with a mention to relevant research European projects in this field. The aims and contributions of the work are also stated; Section 2 focus on the description of the used data and methodology, giving also a brief introduction to the SAR sensing mechanism and available sensors. The proposed complete processing chain is also depicted and the features used in the classification step are listed. Section 3 contains the theoretical basis and formulation of the proposed segmentation algorithms, as well as significative results when they have been applied to SAR data. One example of the use with MERIS data is also showed as an indication of the possibility of applying the techniques to a broader range of data types. In Section 4 the results of the different classification approaches are given. Moreover, the section also contains an a brief description with examples of some typical lookalike sources. Finally, Section 5 gives the conclusions and highlights important issues for future improvement in oil spill detection techniques. The thesis also contains an acronym list and bibliography.

2

Data and Methodology

The main data type used in this work are SAR images from ESA missions ERS-1, ERS-2, and Envisat. For demonstrating the applicability of the segmentation algorithms to other type of data, one MERIS image from Envisat was also used.

This section contains a brief introduction to SAR in general and a description of the SAR missions and products relevant for oceanography, with special emphasis on the missions related with the PhD. After that, the used data set is listed and an overall picture of the applied methodology is provided.

2.1 SAR data

A synthetic aperture radar, or SAR, is a coherent radar system that generates high-resolution remote sensing imagery by means of advanced signal processing techniques. Active radar systems illuminate the scene with their own electro-magnetic energy by transmitting a pulse and then record the strength and travel-time of the returned signals. This allows the range (or distance) of the reflecting objects to be determined [46]. SAR usually operates in the microwave portion of the electromagnetic spectrum, ranging from 1mm to 1 meter (300GHz to 300 MHz) [47], (see Figure 2.1).

SAR systems can be mounted on board of aircrafts or satellites and have a side-looking geometry as illustrated in Figure 2.2 and 2.4.

Most satellites, including ERS-1, ERS-2, and Envisat, are right-side looking. Figure 2.5 depicts the Envisat satellite, which carries a number of instruments on board, among which there is the Advanced SAR (ASAR) instrument, which main element is a 1.3×10

2. DATA AND METHODOLOGY

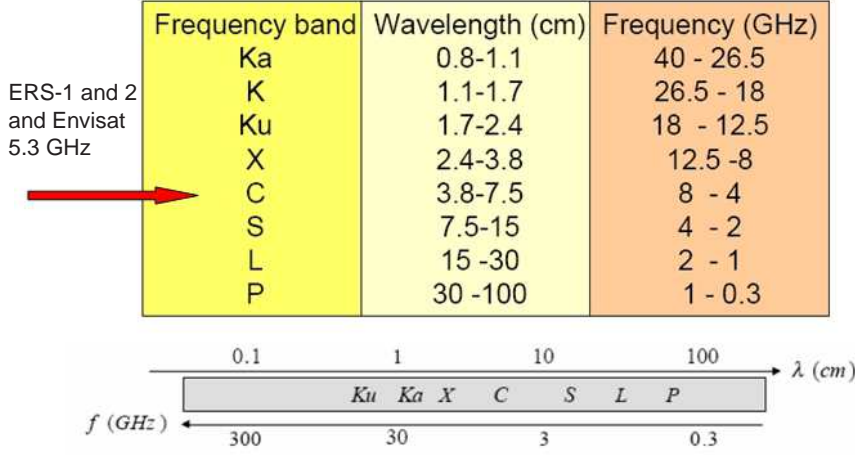


Figure 2.1: Frequency bands used in radar systems (from [47]). Consider that $f = c/\lambda$, where f is the frequency, c is the light speed ($3 \times 10^8 \text{ms}^{-1}$) and λ is the wavelength.

m length antenna, and the MERIS instrument. The satellite is orbiting the earth every hundred minutes, in a near-Earth polar orbit (800 km mean altitude) and moving at a velocity of more than seven kilometers per second. Signal processing of SAR data uses magnitude and phase of the received signals over successive pulses from elements of a synthetic aperture to create an image. The radar antenna beam illuminates the ground to the right side of the satellite and due to the satellite motion and the along-track (azimuth) beam width of the antenna, each target element only stays inside the illumination beam for a short time.

As part of the on-ground processing, the complex echo signals received during this time are added coherently, making use of the Doppler history of the radar echoes. Within the wide antenna beam, returns from features in the area ahead of the platform will have upshifted, or higher, frequencies resulting from the Doppler effect. Conversely, returns from features behind the platform will have downshifted, or lower, frequencies. Returns from features near the centerline of the beam width (the so-called zero-Doppler line) will experience no frequency shift. This process is equivalent to having a long antenna (so called synthetic aperture) illuminating the target. The synthetic aperture L_s is equal to the distance the satellite traveled during the integration time. This is the area on the ground covered by a single transmitted electromagnetic pulse, known as the radar footprint. The result is an increase in azimuthal resolution in the final

image, despite a physically (real) small antenna [46]. To understand this, consider that the azimuth resolution ρ_a is proportional to the expression given in 2.1

$$\rho_a \propto \frac{\lambda R}{L}, \quad (2.1)$$

where L is the length of the radar antenna, R is the nominal slant range and λ is the radar wavelength (see Figure 2.3). When the real aperture is substituted by a synthetic aperture $L_s = 2R_a$, where R_a is half of the azimuth beamwidth, then the new azimuth resolution ρ'_a is given by expression 2.2

$$\rho'_a = \frac{\lambda R}{2R_a} = \frac{L}{2}. \quad (2.2)$$

It would take a conventional antenna of length $2L_s$ to obtain the same resolution without SAR processing[48].

In the case of Envisat, ERS-1, and ERS-2, the radar footprint is on the order of 8.5 km long in the along-track (azimuth) direction. The nominal real-aperture resolution would be 4.25 km, which is very poor. By assembling a synthetic aperture as described before, the azimuth resolution is increased approximately a thousand times, when compared to the real aperture radar, providing a synthetic aperture of about 10 km and an improved resolution of circa 5 m. Note, however, that in the practice several “looks” are averaged to improve the quality of the amplitude image [46], so that the final azimuth resolution is about 25 m.

Regarding the across-track or range resolution, this is a function of the transmitted radar bandwidth, which is inversely proportional to the pulse duration. In SAR systems, pulse compression techniques are used to improve the performance taking into account the instrument peak power capability. The use of a so-called matched filter and of a wide-band (e.g. a chirp) allows the lower intensity, and thus lower power requirements. The used illuminating signal is a sinusoidal wave that increases in frequency linearly with the time, a so-called chirp, and the matched filter avoids the overlapping in time of records coming from adjacent points. The filter delays the different components of the recorded echo signal by a determined value so that they are all compressed into a short spike [51].

From this brief description of the main steps in SAR signal processing, it should be clear that the involved algorithms are heavy and complex. The fully description of SAR

2. DATA AND METHODOLOGY

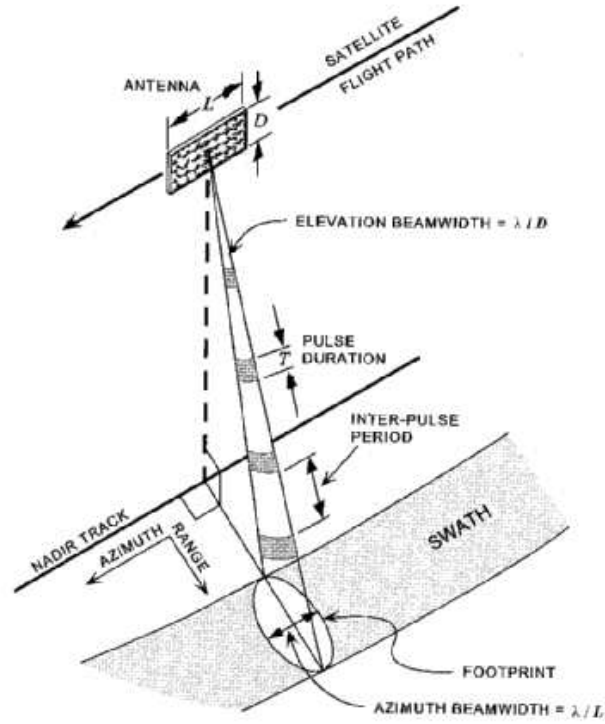


Figure 2.2: Side Looking geometry of a SAR system mounted on board of a satellite (from [49]).

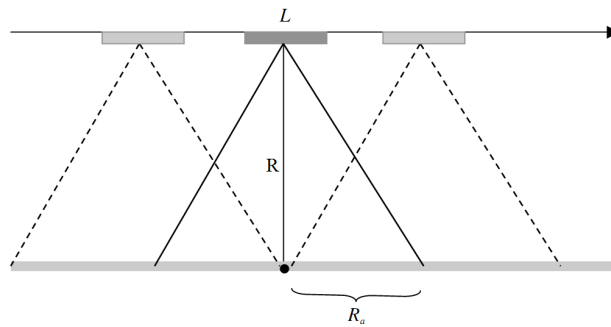


Figure 2.3: Concept of real aperture versus synthetic aperture radar.

L = length of radar antenna (real aperture);

R = nominal slant range (distance to target);

R_a = half of the azimuth beamwidth (radar footprint);

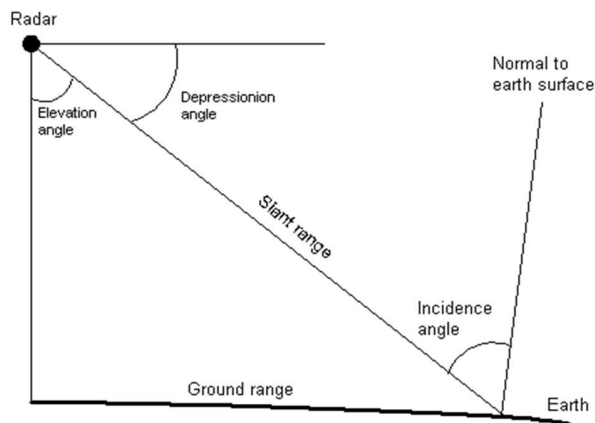


Figure 2.4: Side looking geometry (cont.) (from [50]).

processing is far away from the scope of this work, and the interested reader is referred to [48], to [46], or to [51] among other valuable resources. In this section, the focus will be on giving a description of the main features of SAR data intensity products, after being processed, from the point of view of operational oil spill detection.

2.2 SAR missions and products

There is a vast number of missions operating SAR systems, capable of providing SAR data for many applications, including oceanographic applications, and in special for oil spill detection [52]. Some of these missions are still operative, other have stopped but data is accessible through archives.

Furthermore, SAR systems have the capability to operate at different modes, each one giving raise to products with different characteristics. In modern satellites the beam is steerable, meaning it can be pointed out to the ground dynamically during the satellite pass, resulting in different ground scanning strategies and introducing an extra level of complexity in the processing algorithms [46].

Scanning strategy is one of the issues that specifies the measurement mode. For ERS there is only one scanning mode, the stripmap, but Envisat offers also the scanSAR technique. Moreover, recent missions like Terra-SAR-X also support a third mode of operation, called Spotlight, which we will not describe further here. Another feature that characterizes a SAR image is polarisation. In fact, although older satellites like the

2. DATA AND METHODOLOGY

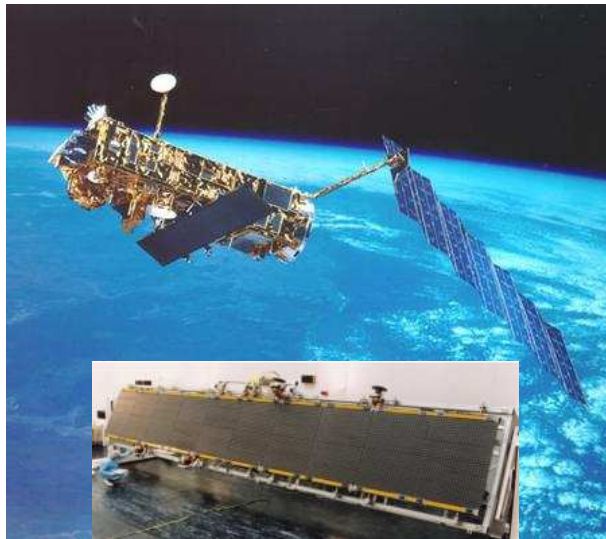


Figure 2.5: Picture of Envisat satellite and of the SAR antenna that is on board the satellite, as main part of the ASAR instrument. It is an active phased array antenna, which allows independent control of the phase and amplitude of the transmitted radiators from different regions of the antenna surface, (ESA copyright).

ERS generation and Radarsat-1 are only operated with radiation at a fixed polarisation (vertical and horizontal polarisation, respectively), modern satellites have the possibility to transmit and/or received in with different polarisation types and even alternate between them. Figure 2.6 provides a closer look to these different possibilities in SAR. Still other factors that distinguish measurement modes can be data rate (implying that data may be subsampled on board of the satellite), and dimensions and information content.

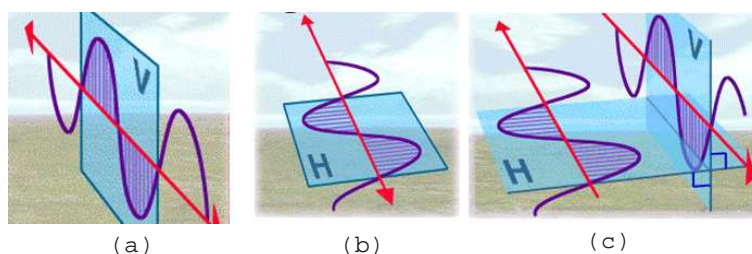


Figure 2.6: (a) VV-Like polarisation: Vertical Transmission/Vertical Reception, (b) HH-Like polarisation: Horizontal Transmission/Horizontal Reception and (c) VH-Cross polarisation: Vertical Transmission/Horizontal Reception (from [46]).

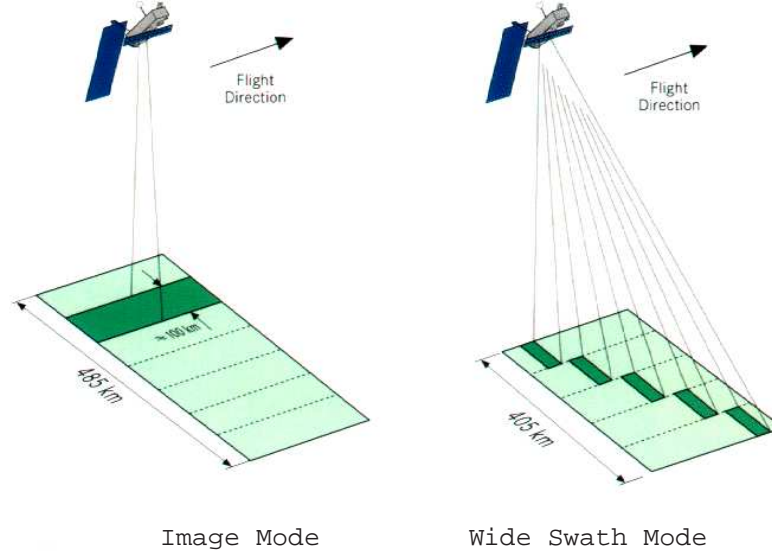


Figure 2.7: Envisat modes for oil spill detection: Image Mode- uses stripmap technique, VV or HH polarisation, 30 m resolution, 100km swath, incidence angle selectable; Wide Swath- uses scanSAR technique, VV or HH polarisation, 150 m resolution, see [46].

In general, the different modes of operation of an imaging system give rise to data acquired with different swaths, incidence angles (defined as the angle), resolution and polarisation. Furthermore, there is a trade-off between coverage and geometric resolution, implying that higher swaths have lower resolutions. Different SAR systems also have different revisit capabilities, depending on the orbiting parameters and give rise to data with different quality.

In respect to the missions that have been used in this PhD, ERS missions were carrying a so-called Active Microwave Instrument (AMI), this combined the functions of a SAR and a wind scatterometer (SCATT). When operating as a SAR sensor, it could be in two measurement modes: Image Mode and Wave Mode. In Image Mode, the instrument acquires highly detailed images of a 100 km wide strip, in Wave Mode it continuously provides information on the direction and shape of ocean wave patterns [53]. Envisat represented an evolution of the measurement capabilities, offering five distinct measurement modes: Image mode (IM), Alternating Polarisation mode (AP), Wide Swath mode (WS), Global Monitoring mode (GM) and Wave mode (WV). IM, AP, and WS modes are designated as high rate modes, and have a downlink rate of 100

2. DATA AND METHODOLOGY

Mission	Product Name /ID	Approx. Coverage (range x azimuth)	Spatial resolution (range x azimuth)	Revisit Frequency	Band/ Polarisation
ERS-1/2	Image Mode Precision /ERS.SAR.PRI	100km x100km	25m x 25m	35 days	C-Band/ VV
Envisat	Image Mode Precision /ASA_IMP_1P	56-100km x 100km	30m x 30m	35 days	C-Band/ VV
	Wide Swath Standard /ASA_WSM_1P	400km x 400km	150m x 150m		
Radarsat-1/2	Standard Mode	50kmx50km	8mx8m	24days	RSAT-1: HH RSAT-2: HH or VV
		100kmx100km	25mx25m		
	Wide Mode	150kmx150km	27 x 27		
	ScanSar Wide	500kmx500km 300kmx300km	100mx100m 50mx50m		
TerraSAR-X	ScanSAR Image	100km x150km	18m x 18m	11 days	X-Band/ VV or HH
CosmoSkyMed 4-spacecraft constellation	ScanSAR Wide Region	100km x 100km	30m x 30m	5 days each satellite	X-Band/ HH, VV, HV, or VH
	ScanSAR Huge Region	200km x 200km	100m x 100m		

Figure 2.8: Most relevant missions and SAR products for oil spill detection.

Mbps. GM and WV are low rate modes and have a data generation rate of 0.9 Mbps. Figure 2.7 depicts the two modes that are normally used for oil spill detection: IM and WS [46].

Moreover, after acquiring data on a specific mode, the data can be processed to different levels, giving raise to a number of distinct final product types. Data can be delivered to the end user after undergoing different processing stages, corrections and transformations, and in different geometries (ex: in slant range, in ground range, projected or orthorectified). When choosing a product, the user has to take into consideration the final application, because the requirements on the data, even for oceanographic applications, are often incompatible. The type of product chosen also determines the available information. For some products, the phase is retrievable; for others, only the amplitude of the SAR data is available.

For operational oil spill detection, the following requirements are recommendable (see for example [11]):

- Wavelength: C-Band, X-Band and Ku-Band have shown the greatest contrast oil slick/water. The C-Band seems to be the most suitable frequency.
- Incidence Angle: small (steep) incidence angles are preferably, due to the stronger Bragg scattering at those angles.
- polarisation: it has been experimentally demonstrated, using artificial slicks, that VV polarisation seems to be most suitable for C-Band.
- High revisit time.
- Wide Coverage: wide swath modes, acquired using the scanSAR principle, provide the best trade-off between spatial resolution and monitored area.

The requirement of wide coverage is to be understood in the context of a routine monitoring system. In fact, in case of an emergency, where an oil spill has already been identified and one wants to continue targeting it, high resolution images, which imply narrower swaths, are also adequate.

We note that some of the requirements are in conflict with other ocean applications, like vessel and ice detection. In this case, HH polarisation and high (incidence angles) have proved to be more effective.

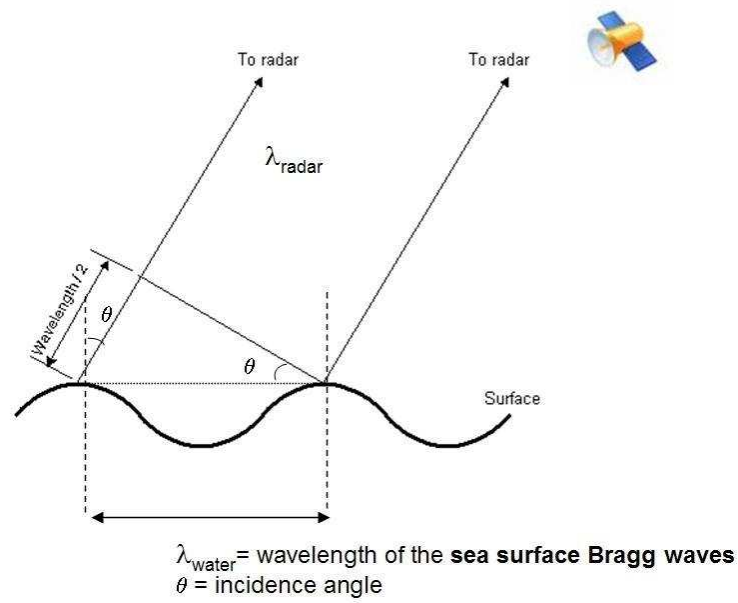
Figure 2.8 shows a list depicting the main SAR missions currently available, with some of the product's specifications.

2.2.1 SAR Sensing of the Ocean

The pixels in a SAR image are backscatter measurements that are associated with the interaction of the radiation with the target/material. In order to interpret the image, we have, thus, to understand these physical processes. In general, many factors affect the strength of a radar signal backscattered from a given material, for a given incident wave power, from which we highlight the following:

- the radar-target distance
- the incident power

2. DATA AND METHODOLOGY



**Bragg Resonance
Condition**

$$\lambda_{\text{water}} = \frac{\lambda_{\text{radar}}}{2 \sin \theta}$$

Figure 2.9: Bragg scattering of SAR radiation on the ocean surface, see see [46].

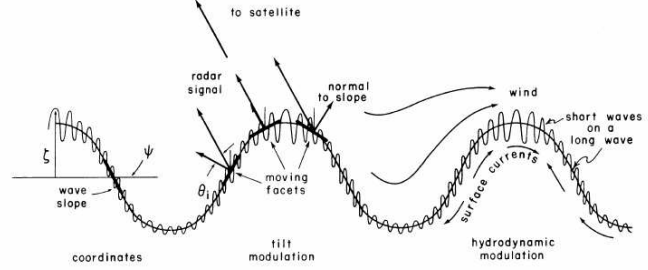


Figure 2.10: Two-scale approximation theory of longer/shorter wave interaction in the ocean (from [1]).

- the roughness of the material (rougher => higher backscatter => brighter image).
- the dielectric constant of the material (wetter => higher).
- the local incidence angle α (smaller => high).
- the radar wavelength and polarisation.
- the shape and orientation of the materials.
- the terrain geometry.

In SAR sensing of the ocean, the primary scattering mechanism, when the incidence angle ranges between 20 and 45, is the Bragg resonance Mechanism [11] (see Figure 2.9). When the radar wavelength, λ , projected onto the surface matches a periodic structure on the surface, there is a resonance effect causing a strong backscatter termed Bragg scattering. This means that the most important factor affecting the backscatter return is the surface roughness on the scales of the Bragg waves (the ones meeting the Bragg resonance condition). For C-Band radar, these are the so-called short gravity waves (wave lengths in the range of 5-7 cm) that are generated by winds blowing over the ocean surface [50]. The amplitude of the Bragg waves can mainly be modulated by the local wind speed and direction with respect to the line-of-sight direction of the radar antenna, and by longer gravity waves. The interaction of short and long ocean waves and how these interactions affect the radar backscattering is referred to as the two-scale approximation” and can be visualized in Figure 2.10 [50].

2. DATA AND METHODOLOGY

As a consequence of these interactions, although the SAR “sees” only the “Bragg waves”, these waves can be modulated by a large number of upper ocean and atmospheric boundary layer phenomena. This is the reason why lookalikes become visible in SAR images.

In Section 4.1, examples of some relevant lookalikes are given.

2.3 Data Set

The data used in this PhD can be divided in two main groups: the data set used for developing and testing the segmentation algorithms and the data set used for developing and testing the classification.

2.3.1 Data Set for Segmentation

The image data set used to develop the segmentation algorithms was ordered in the framework of the already referred “Oil Slick Surveillance Using ASAR/MERIS Data” project.

In order to identify the relevant images, a survey was undertaken. Images have been identified from relevant research articles, tutorials, and project websites, as well as from public available oil spill databases. The following references were considered reliable sources for selecting the data set and for getting background information on the scenario:

- ESA oil slick earth watching web pages [5]: collection of oil spill case studies around the world.
- MDA pages [54]: collection of use cases for SAR applications.
- NOAA tutorial [1]: a SAR tutorial sponsored by the NOAA/NESDIS.
- Oceanides database [55]: oil spill database that was built in the context of the Oceanides project, by the Joint Research Center.
- Tropical and subtropical ocean viewed by ERS SAR [3]: website illustrating range of oceanic and atmospheric phenomena visible in SAR.

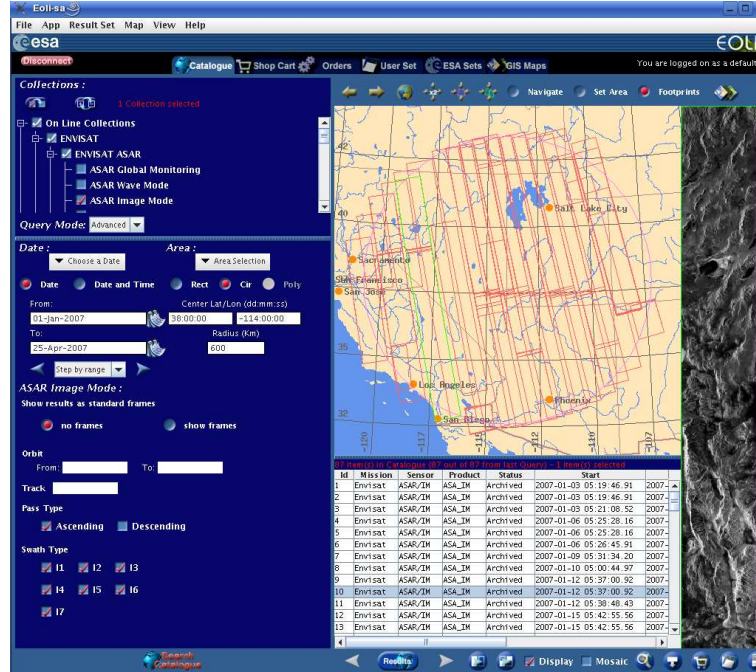


Figure 2.11: GUI of EOLI-SA (ESA copyright).

- Cearac web page [56]: oil spill database from the “Coastal Environmental Assessment Regional Activity Centre” (CEARAC), which is part of the regional seas program of the “United Nations Environment Program” (UNEP).

After being identified, images have been ordered using the “Earth Observation Link Stand Alone” (EOLI-SA) application, from ESA. This is a java client for Earth Observation Catalogue and Ordering Services for browsing the metadata and preview Earth Observation (EO) data acquired by ESA (ERS and Envisat) and many third part satellite missions, like Landsat, IKONOS, ALOS, SPOT, JERS, and Terra/Aqua. This application can be downloaded for free from <http://eoli.esa.int/geteolisa>.

Because many images in the literature are not fully identified, the process of ordering was oft complicated and needed visual screening of quicklooks and further investigations.

2.3.2 Data Set for Classification

The part of this PhD regarding the evaluation of different classification approaches has been performed in cooperation with Edisoft S.A, a private Portuguese company. This

Table 2.1: Data Set for Segmentation-Part I.

Description	Product Type	Identification	Comment	Reference Source
Cercal accident in Douro plume	ERS-1 SLCI	Date: 04-Oct-1994 Orbit: 16838 Frame: 2781	Acquired two days after the accident at the Leixoes harbor	ESA oil slick Earth Watching web pages
Prestige accident in Galicia	ASA_WSM_1P	Date: 17-Nov-2002 Orbit: 3741	most popular SAR image documenting the Prestige accident	Sample data from ESA
Prestige accident in Galicia	ERS-2 SLCI	Date: 16-Dec-2002 Orbit: 40028 Frame: 2727	effect on Spanish coast	International Charter Space and Major Disasters
Prestige accident in Galicia	ASA_WSM_1P	Date: 16-Dec-2002 Orbit: 4156	effect on Spanish coast	International Charter Space and Major Disasters
Acquisition between Cyprus and Lebanon	MER_FR_2P	Date: 19-Jul-2004 Orbit: 11785 Track: 208	There is a ASAR image of the same date and place	Oceanides database
Acquisition between Cyprus and Lebanon	ASA_IMP_1P	Date: 19-Jul-2004 Orbit: 12471 Frame: 2943	There is a MERIS image of the same date and place	Oceanides database
	ASA_WSM_1P	Date: 01-Jun-2004 Orbit: 11792		Oceanides database
Gotland Island case	ASA_WSM_1P	Date: 09-May-2005 Orbit: 16687	97-kilometer oil slick of unknown source	ESA oil slick Earth Watching web pages
Sicily Channel case	ERS-1 SLCI	Date: 30-Jan-1992 Orbit: 2828	ship wake, natural film and current features also present	ESA oil slick Earth Watching web pages
Philippines	ASA_WSM_1P	Date: 24-Aug-2006 Orbit: 23432 Time: 01:44:31	oil spill from a sunken tanker spread threatening rich fishing grounds	ESA oil slick Earth Watching web pages
North Sea	ERS-1 SLCI	Date: 30-Oct-1994 Orbit: 17211 Frame: 2367	suspicious slicks in Norwegian and British platforms	in article [21]
Mediterranean Sea northwest of Port Said	ERS-1 SLCI	Date: 01-Jun-1992 Orbit: 4589 Frame: 2961		in proceedings [57]
Coast of Lebanon	ASA_IMP_1P	Date: 21-Jul-2006 Orbit: 22949 Time: 07:49:03	spill due to air strikes that on July 13 and 15 2006 hit the oil-fueled power plant of Jiyeh	MDA web pages
led power plant of Jiyeh				

Table 2.2: Data Set for Segmentation-Part II.

Description	Product Type	Identification	Comment	Reference Source
Yellow Sea	ERS-2 SLC	Date: 05-Jul 2003 Orbit: 42900 Frame: 2979	contains also ships, internal waves and low wind features	Cearac web page
Japan/East Sea	ERS-1 SLC	Date: 08-Nov 1993 Orbit: 12100 Frame: 2763	biogenic and man-made slicks	Cearac web page
Korea/Ulleung	ASA_WSM_1P	Date: 14-Apr 2004 Orbit: 11093	oil slicks and biogenic films building eddies configurations	Cearac web page
	ASA_WSM_1P	Date: 14-Apr 2004 Orbit: 11093	contains 2 oil spills	Cearac web page
northwestern Japan-East Sea	ASA_WSM	Date: 16-Oct 2003 Orbit: 8502	contains 2 oil spills	Cearac web page
Southeast coast of Sicily	ERS-1 SLC	Date: 26-May 1994 Orbit: 14957 Frame: 2871	contains 2 oil spills and many lookalikes	NOAA tutorial
Coast of Malaysia	ERS-2 SLC	Date: 4-Apr 1997 Orbit: 10221 Frame: 3519	oil pollution in busy shipping lane busy shipping lane	NOAA tutorial
Indian Ocean	ERS-2 SLC	Date: 6-Apr 1999 Orbit: 20700 Frame: 3393	“feathered structure” of an oil trail	NOAA tutorial
South China Sea	ERS-1 SLC	Date: 15-Apr 1996 Orbit: 24841 Frame: 3555		Tropical and subtropical ocean viewed by ERS SAR
South China Sea	ERS-2 SLC	Date: 13-Jul 1997 Orbit: 11652 Frame: 3483		Tropical and subtropical ocean viewed by ERS SAR

2. DATA AND METHODOLOGY

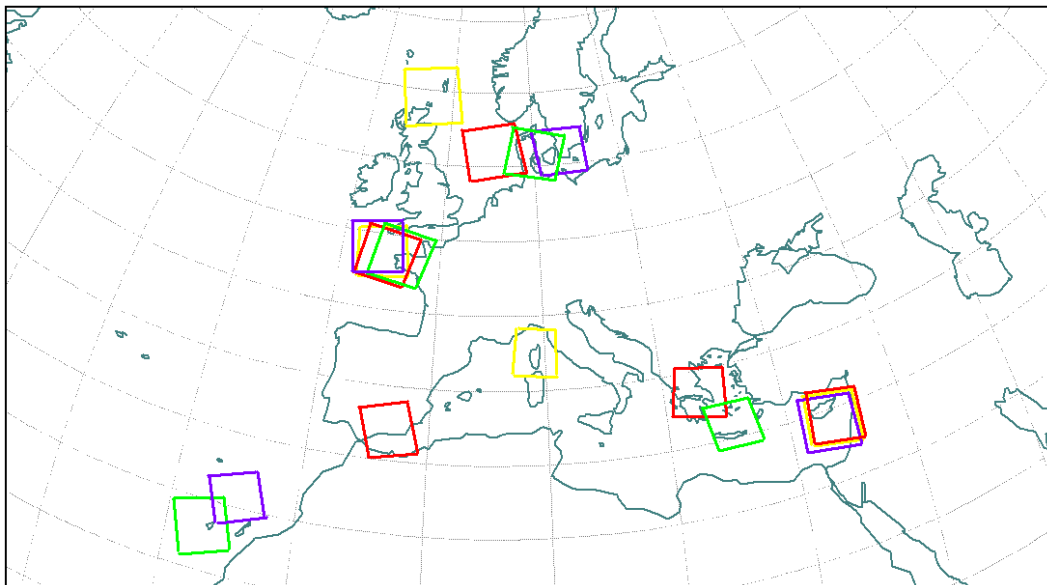


Figure 2.12: Location (footprints) of the 17 SAR images used for classification.

is a software development and services company with a space department under which in recent years a number of different projects oriented to ocean remote sensing are running. In particular, Edisoft has taken part in the MARCOAST project, referred to in Figure 1.7, and is one of the service providers of the EMSA CSN service as described at the beginning of this thesis.

Edisoft has a group of well trained oil spill detection operators and is responsible for the management and operation of a dual-mission Station: the ESA Tracking Station and EDISOFTs Earth Observation Station at Santa Maria, in Azores. The company has established an agreement with the “Instituto de Telecomunicações”, under which SAR images have been provided, as well as the oil detection results and associated auxiliary data, for the scope of evaluating our automatic classification approaches. A total of 17 Envisat ASAR.WSM.1P images have been provided, covering a number of different European coastal areas: Portugal, Spain, Italy, France, Cyprus, Turkey, Greece, Germany, Sweden, Denmark, and United Kingdom.

The images have been analyzed by experienced oil spill detection operators, which identified 70 oil spills, 8 of which have been verified and confirmed in-situ. Furthermore, 70 lookalikes have also been identified in the scenes and used to build a database containing a total of 140 dark spots (70 oil spills + 70 lookalikes). Figure 2.12 gives

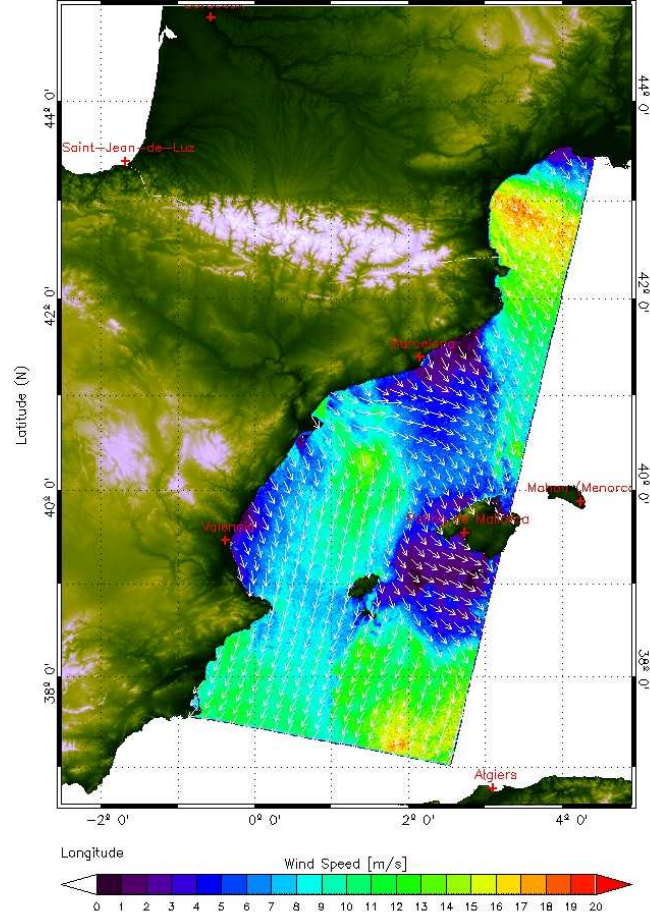


Figure 2.13: Example of wind field retrieved from SAR by SARTool (CLS/BOOST copyright).

an overview of the location of the images. Images have been acquired over different geographical areas, aiming at developing a classifier as general as possible and not tuned to specific sources of lookalikes. In fact, an effort was made to include lookalikes with different oceanographic and atmospheric origins, thus related to diverse SAR signatures. In Section 4.1, an overview of the different sources of lookalikes is given. The choice of the oil spills has also been done keeping in mind that there are different types of signatures [10] depending on their origin and environmental actors, and ensuring that all these types were present in the database.

Although some of the images contain verified oil spills, for others no validation was available, so that the operator’s analysis was considered as ground-truth. The opera-

2. DATA AND METHODOLOGY

tors' analysis was documented in form of a report, containing the center coordinates of the dark patches that had been considered to be oil spills, as well as the confidence assigned to this assessment and some descriptive features regarding the shape, edges, contrast, and homogeneity of the spill surroundings, for corroborating their decision.

We have then segmented the images using Algorithm-1, introduced in Section 3.5, and have considered the dark patches as oil or as lookalike, for building the training data set, based on the operator's evaluation. We assumed that any dark signature on the image that was not reported as an oil spill was considered to be a lookalike.

Furthermore, we also had access to wind estimations retrieved from each one of the SAR images. For extracting this information, the company is running a software tool called SARTool, from the Boost company, now integrated within the French CLS company. The tool is an IDL-based GUI which enables to read, visualize and process any type of path-oriented SAR images. The advantage of using SAR retrieved wind is the higher spatial resolution when compared to meteorological models or scatterometer data. Moreover, also meteorological data were delivered for the data set. The meteorological data were generated by models run by the "Portuguese Meteorological Institute". In the following, a list of the used data for classification is given:

- SAR data: 17 ASA_WSM_1P images covering different parts of the European waters.
- SAR retrieved wind: the SAR wind retrievals are based on the combined use of CMOD-IFREMER2 [58] and HIRLAM [59]. CMOD-IFREMER2 is an inversion empirical algorithm to estimate wind speed from calibrated data (σ^0) and needs an initial wind direction as input. This initial wind estimation is given by the HIRLAM model. HIRLAM provides wind fields with accuracy of about 2 m/s and +/- 10 degrees. The final derived wind field products have a 2 km spatial resolution but also depend on the model errors. Validation analysis indicate a resulting root mean square (rms) error of the SAR derived wind speed of about 2.0 m/s in speed and 27° in direction for ASAR wide swath. The files are provided in "Network Common Data Form" (NetCDF) format [60]. Figure 2.13 shows an example of an wind field retrieved from SAR by SARTool.
- meteorological wind: EDISOFT oil spill detection chain obtains daily wind information from the Portuguese Meteo Office (<http://www.meteo.pt>). Wind speed

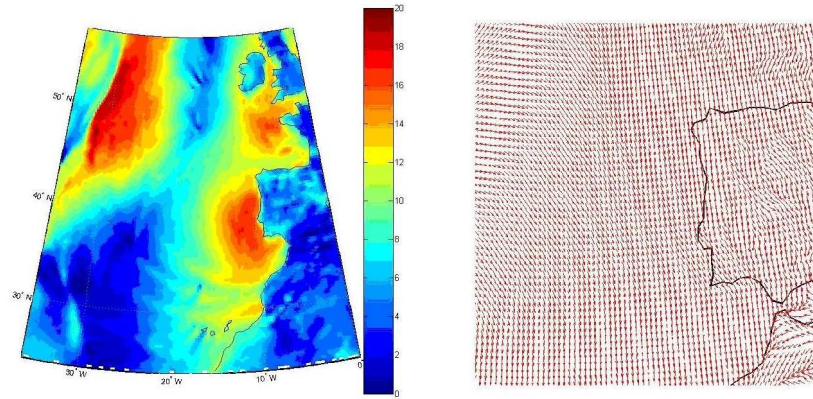


Figure 2.14: Wind sample data from the Portuguese Meteorological Institute.

and direction predictions at 10 meters are generated once a day by an ECMWF model with a 0.25° spatial resolution in latitude and longitude. The temporal resolution is 3 hours, and the forecast range is 24 hours. Figure 2.14 shows an example of generated wind field data. Edisoft provided wind model data interpolated to the image acquisition times, for each data set.

- meteorological wave: EDISOFT also obtains daily wave information from the Portuguese Meteo Office. The used model is the MAR3G that provides sea-state data: significant wave height, mean wave direction, and mean wave period. It is a deep-water model that applies a Mercator cartographic projection on the North Atlantic zone with a special resolution of 1° in latitude and longitude. The model is run four times daily and generates one prediction with a forecast range of 12 hours. Edisoft provided wave model data interpolated to the image acquisition times, for each data set.
- oil spill detection reports: the reports provided by Edisoft contain the result of the semiautomatic analysis done by the operator. In summary the information delivered for each oil spill are: center coordinates, confidence, region affected, area, width, length, slick orientation, possible source coordinates, model wind and wave values, SAR wind values, and slick visual evaluation of the geometry, contrast and surroundings characteristics.
- validation information: for some of the spills ($\approx 15\%$), we also had validation

2. DATA AND METHODOLOGY

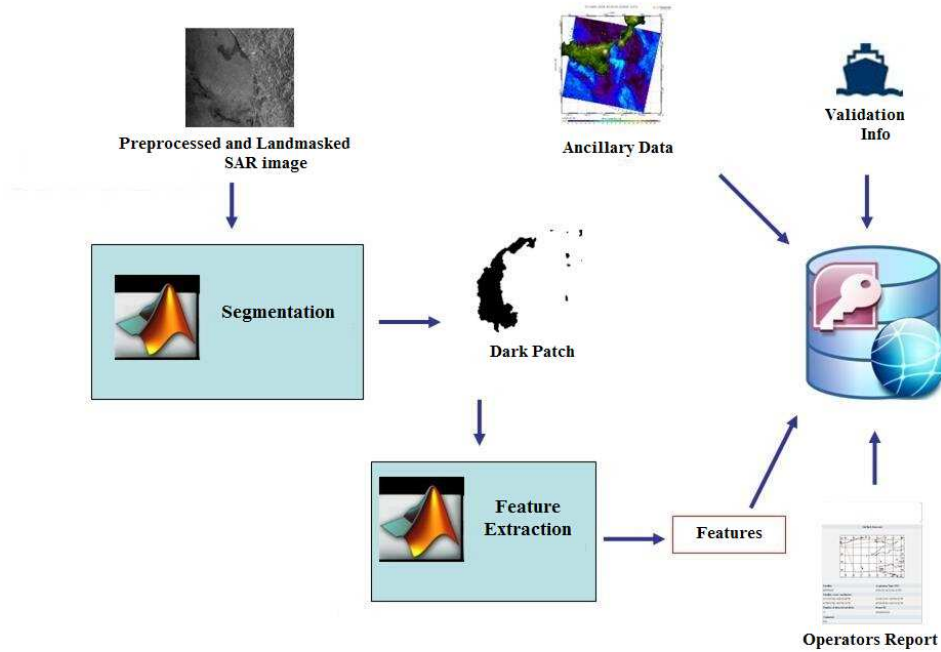


Figure 2.15: Database: an MS Access database was built, containing the extracted features and other information of interest obtained from meteorological data sources and from the operators’ and validation reports.

information, like in-situ verified lengths and widths of the detections. Although we injected this data into the database with the final scope of incorporating this evidence in the algorithms, we have not used it in this work.

SAR retrieved wind, meteorological wind and meteorological wave are denominated here after ancillary data.

For each image, relevant information has been stored in an MS-Access database developed during the PhD. The database contained metadata regarding the images and information for each oil spill and lookalike retrieved from the data set provided by Edisoft (ancillary data and report). Apart from the information provided by Edisoft, we also stored there on a later stage the results of the Feature Extraction step, which we will explain in detail in the next section. Figure 2.15 depicts the data types that have been stored in the developed database. The database has been used for managing all the information needed for training and testing the classification algorithms.

For each oil spill and lookalike, ancillary data, information contained in the reports, and validation information have been stored. In fact, although in our tested classification methods we only used the wind speed and the matlab calculated features, we think the rest of the information can be of interest in the future for other approaches or improvements.

2.4 Methodology

We have followed in general the common pipeline structure depicted in Figure 1.5. For testing the segmentation approaches, we have performed the first 2 steps: Image Pre-processing and LandMasking. For testing the classifiers, we applied the whole chain.

In the following, we give more details on the steps undertaken. The segmentation and classification steps, as they are the core of this work, are described in dedicated sections in the remaining of this text.

2.4.1 Process Chain

We have adopted a processing chain following the typical structure of an oil spill detector, as already described and depicted in Figure 1.5.

1. **Image Preprocessing** Two preprocessing steps have been undertaken: the images have first been calibrated in order to retrieve the radar backscattering (σ^0) and then an incidence angle compensation technique has been applied. For retrieving σ^0 we have used a free available ESA provided software called BEST (<http://earth.esa.int/services/best/>). This is a collection of executable software tools that has been developed to facilitate the use of ESA SAR data. At the end of this PhD, a new, more advanced, free toolbox for SAR data processing has been made available by ESA: NEST. The acronym stands for Next ESA SAR Toolbox. Among many improvements in comparison to BEST, the tool allows the visualization and processing of third part SAR data, like Radarsat and TerraSAR-X data. The use of calibrated data was important due to the fact that we are using some features based on the digital values of the pixels. For doing so, the digital values have to be comparable and relate to the same physical parameter. The BEST calibration routine implements the steps described by

2. DATA AND METHODOLOGY

ESA in the document [61]. To perform a precise absolute image calibration and derive the radar backscattering coefficient for the type of products we are using, detected ground range products, a detailed knowledge of the local slope (i.e. local incidence angle) would be in fact required. Since this information is usually not available at the processing time, a “flat terrai” is assumed during processing (based on the ellipsoid WSG84) and the final intensity image is therefore proportional to the radar brightness of the illuminated scene. The processing is basically a division by a constant and a multiplication by the sinus of the incidence angle. The relationship between the value of the image pixels (DN), the radar brightness (β^0) and the radar backscattering coefficient (σ^0) can be written as given in the following equation [61]:

$$\text{DN}^2 = K\beta^0 = K\frac{\sigma^0}{\sin(\alpha)} = \text{Cte}(\alpha)\sigma^0 \quad (2.3)$$

where α is the incidence angle, K is denominated “absolute calibration constant” and Cte is a constant depending on α .

K is derived -in the ASAR case- from measurements over precision transponders. This factor is dependent on the processor and product type, and might change between different beams for the same product type.

On the other hand, we also had the need to compensate the incidence angle effect on the σ^0 value itself, from the point of view of the scattering physical mechanism associated with the oil presence. For this we adopted a technique described in [30]. In this work, the author refers that due to the wide extension of the ASAR WS image swath, the scattering mechanism is mixed: for small incidence angles the specular mechanism is stronger and for higher incidence angles the Bragg mechanism dominates. In absence of an analytic expression for the radar backscattering, the authors derived an exponential fit directly from data. It is this exponential fit that we applied in this work.

2. **Landmasking** For the landmasking, the freely available coastline data from the “Global Self-Consistent High-Resolution Shoreline Database” (GSHHS) [62], in its higher resolution mode and shapefile format, has been imported into matlab and used to mask the land. GSHHS is developed and maintained by the University

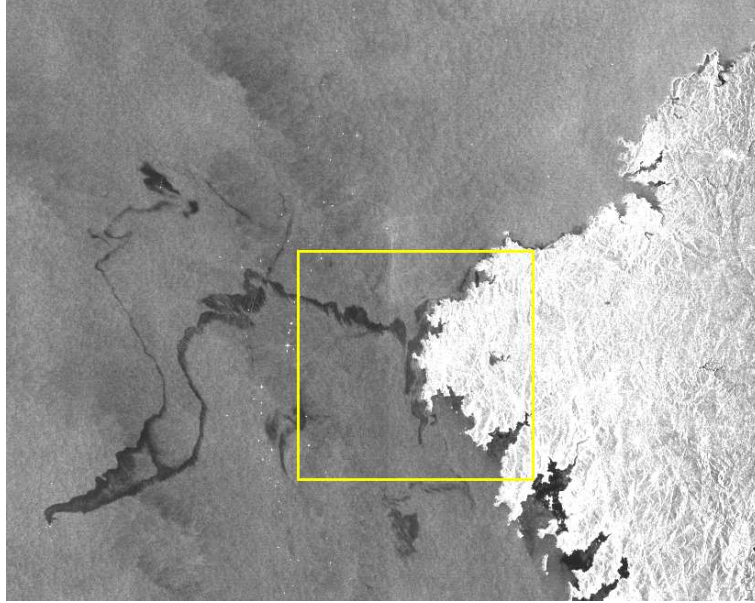


Figure 2.16: Envisat ASAR_WSM_1P image acquired on the 11th November 2002 from the Prestige accident. This is a sample data from ESA and is freely downloadable from ESA’s site. The displayed yellow rectangle is used for demonstrating the landmasking, in Figure 2.17.

of Hawaii and by the NOAA Laboratory for Satellite Altimetry. Figure 2.17 which is a zoom of Figure 2.16 gives an idea of the resolution of the used coastline. We note that this data set does not take into account very small islands or rocks but this is in fact worst for automatic vessel detection algorithms. What is more problematic for oil spill detection are sandbanks, due to its “dark appearance” that makes them typically lookalikes, and these are also not described in the coastline. In order to get information on sandbanks, and bathymetry in general, the so-called Electronic Nautical Charts (ENCs) may be used. ENCs contain other relevant information for oil spill detection, like vessel traffic separation schemes, which may be used to develop risk maps for oil spill detection. ENCs must be updated because some of the information they contain, like for example sandbank location, is dynamical. This information is particularly important for zones with low bathymetry, where the tide effect is stronger. Dark patches from sandbanks have been included in the training data set we used for the classification algorithms.

2. DATA AND METHODOLOGY

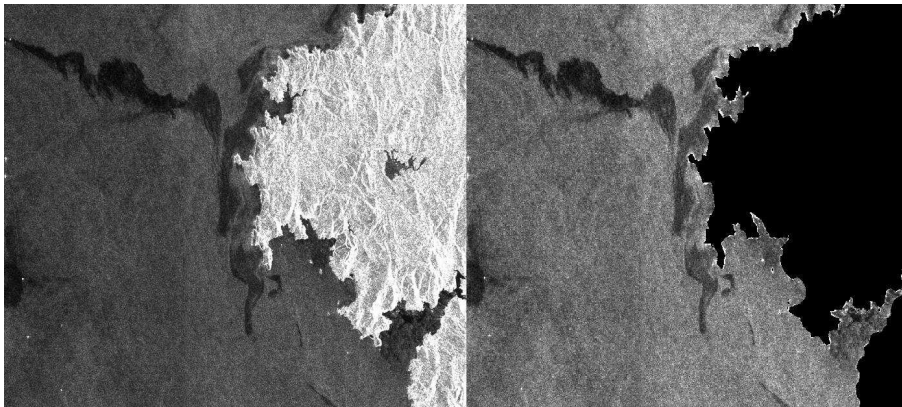


Figure 2.17: Zoom of the Prestige Envisat image, showing the effect of applying a land-mask based on the GSHHS coastline.

3. **Segmentation** We have applied one of the algorithms developed in this work, namely Algorithm-1, described in detail in Section 3.5. This algorithm has been chosen only due to practical reasons, as it is the fastest of the proposed segmentation methods.
4. **Feature Extraction** We have developed and run different matlab routines in order to calculate a number of features, both from the dark patch as also from a 150x150 pixel window from the surroundings. The complete list of extracted features is given in detail below, Section 2.4.2. The features have then been stored in the database, together with other complementary information.
5. **Classification** In the classification step, we have run all the classifiers described in detail in Section 4.2.

2.4.2 Extracted Features

A total of 35 features have been considered for classification. An attempt was made to extract as many features as possible from those referred in the state-of-the-art literature (see Section 1.2).

These features have all been extracted from the segmented dark patch, except for the wind information, which was overtaken from the ancillary data or from the operators reports. The used features can be divided in four main groups: geometrical, backscatter, texture and ancillary data features.

1. Geometrical Features:

- Area (A)
- Perimeter (P)
- Complexity (C), defined as

$$C := \frac{P}{2\sqrt{\pi A}}.$$

This feature will take a small numerical value for regions with simple geometry and larger values for complex geometrical regions.

- Length (L): sum of skeleton edges (obtained by Delaunay triangulation), that build the main line.
- Width (W): mean value of Delaunay triangles which are crossed by main line.
- Length To Width Ratio (LWR), defined as

$$LWR := \frac{L}{W}.$$

- Compactness (Comp), defined as

$$Comp := \frac{LW}{A}.$$

- First Invariant Planar Moment (FIPM), defined as

$$FIPM := \frac{1}{n^2} \sum_{i=1}^n \left[(x_i - x_c)^2 + (y_i - y_c)^2 \right]$$

with

$$x_c := \frac{1}{n} \sum_{i=1}^n x_i, \quad y_c = \frac{1}{n} \sum_{i=1}^n y_i,$$

and n the number of points in the dark patch contour.

- Ellipse-Length (EL): value of main axe of an ellipse fitted to the data.
- Ellipse-Width (EW): value of minor axe of an ellipse fitted to the data.
- Ellipse-Asymetry (EA), defined as

$$EA := 1 - \frac{EW}{EL}.$$

2. DATA AND METHODOLOGY

- Form Factor (FF): represents the dispersion of the dark patch pixels from its longitudinal axis, when a line is fitted; it is calculated as norm of residuals after line fit to the dark patch pixels.
- Spreading (S): this feature is derived from the principal component analysis of the vectors whose components are the coordinates of the pixels belonging to the dark patch (see [24] for details). Feature S will be low for long and thin objects and high for objects closer to a circular shape.

2. Backscatter Features:

- Inside Slick Radar Backscatter (μ_{obj})
- Inside Slick Standard Deviation (σ_{obj})
- Outside Slick Radar Backscatter (μ_{sce})
- Outside Slick Standard Deviation (σ_{sce})
- Intensity Ratio ($\frac{\mu_{obj}}{\mu_{sce}}$)
- Intensity Standard Deviation Ratio ($\frac{\sigma_{obj}}{\sigma_{sce}}$)
- Intensity Standard Deviation Ratio Inside (ISRI), defined as

$$\text{ISRI} := \frac{\mu_{obj}}{\sigma_{obj}}.$$

- Intensity Standard Deviation Ratio Outside (ISRO), defined as

$$\text{ISRO} := \frac{\mu_{sce}}{\sigma_{sce}}.$$

- ISRI ISRO Ratio
- Min Slick Value (MinObj)
- Max Slick Value (MaxObj)
- Max Contrast (ConMax): difference (in dB) between the background mean value and the lowest value inside the object, defined as

$$\text{ConMax} := \mu_{sce} - \text{MinObj}.$$

- Mean Contrast (ConMe): difference (in dB) between the background mean value and the object mean value, defined as

$$\text{ConMe} := \mu_{sce} - \mu_{obj}.$$

- Max Gradient (GMax): maximum value (in dB) of border gradient magnitude, calculated using Sobel operator.
- Mean Gradient (GMe): mean border gradient magnitude (in dB).
- Gradient Standard Deviation (GSd): standard deviation (in dB) of the border gradient magnitudes.

3. Texture Features:

Texture is a combination of repeated patterns with a regular frequency and texture analysis has often proved to be effective for oil spill classification (see [28], [20] and [34]). We have used gray level co-occurrence matrices (GLCM) to specify texture measures (see [63]) and have used the following measures:

- GLCM Homogeneity
- GLCM Contrast
- GLCM Entropy
- GLCM Correlation
- GLCM Dissimilarity

4. Ancillary Data Features:

- Wind Speed

A fifth group, of so-called context features, is also referred to in the literature, but was not used by us. This group includes features like:

- Distance from land
- Distance to large dark areas
- Distance to next bright spot (vessel, platform)
- Number of bright spots nearby
- Number of dark Objects in the vicinity

2. DATA AND METHODOLOGY

We note that many of the extracted features are related to the same slick characteristics and are correlated. For example the features “Spreading”, “Compactness” and “LengthToWidthRatio”, both describe how long and thin objects are. In the same way, the features “First Invariant Planar Moment”, “Form Factor” and “Ellipse Assimetry” can all be considered to give an indication to the general shape of the object. In our work we wanted to examine as much of the features referred to in the literature as possible.

As a remark, it is important to say that all features have been standardized before being further used in the classification step. This is necessary because features can have different scales although they refer to comparable objects [64]. Consider for instance, a pattern $x = [x_1, x_2]$ where x_1 is a width measured in meters and x_2 is a height measured in centimeters. Both can be compared, added or subtracted but it would be unreasonable to do it before appropriate normalization. We have used the following classical centering and scaling procedure of the data : $x \text{ norm}_i = (x_i - \mu_i)/\sigma_i$, where μ_i and σ_i are the mean and the standard deviation of feature x_i over the training examples.

3

Segmentation

3.1 Introduction

In the following, we present algorithms that have been developed for the segmentation of dark signatures in oceanic SAR images, following a Bayesian approach. The algorithms have been developed aiming at oil spill detection but, as we will also show at the end of the chapter, they can also be used to segment other type of signatures, and also more than one type of signatures at the same time. The adopted technique uses as data model a finite Gamma mixture, with a given predefined number of components, for modeling each class density. In fact, this density is well suited to filtered intensity SAR images as shown, *e.g.*, in [65], [66]. By using a mixture of densities, we aim at describing the continuous backscattering variability that may be observed in the SAR sea data. Moreover, a mixture is able to describe densities presenting more than one maximum, as it is the case of oceanic multi-look SAR images histograms. This cannot be achieved by none of the statistical models for SAR intensities proposed in the literature, like for example any of the Pearson distributions [67].

In this work, we propose two supervised and one unsupervised algorithms. In the supervised algorithms, the user manually selects a region containing pixels from the dark signature of interest and a region containing water pixels. These regions should be statistically representative and can be made up of non-connected parts. The unsupervised algorithm is an improvement of the supervised ones and is completely automatic.

To estimate the parameters of the class conditional densities, a new EM method

3. SEGMENTATION

was developed. Details are described in Section 3.3. When segmenting small sub-scenes of the image, a simplified data model with only one Gamma function per class can be used.

The prior used to impose local homogeneity is a multi-level logistic (MLL) model Markov random field (MRF) [36], with 2nd order neighborhood. To infer the prior smoothness parameter controlling the degree of scene homogeneity, we develop an EM algorithm that uses loopy believe propagation (LBP) [43]. We have also exploited different classic estimation methods, namely the least squares fit (LSF) and the coding method (CD) (see [36] for details) for comparison.

To infer the labels, we adopt the maximum a posterior (MAP) criterion, which we implement efficiently and exactly with graph-cut techniques [68].

Although the segmentation of oceanic dark patches is typically based on the assumption of two classes, we have generalized the problem to an optional number of classes. The underlying integer optimization problem is now attacked with the graph-cut based α -Expansion algorithm [69].

To evaluate the accuracy of the proposed algorithms, different simulations addressing both the referred Gamma model as well as intensity images corrupted with Gaussian noise have been carried out for error rate assessment.

The algorithms have also been applied to real SAR images containing well documented oil spills. For doing so, the scenes are divided in tiles and segmented individually. Moreover, the described Bayesian algorithm may be also applied to other type of data, like the case of MERIS images. To do so, only the data model needs to be adapted to the data.

3.2 Problem Formulation

3.2.1 Bayesian Approach

Let $\mathcal{L} := \{1, \dots, c\}$ be a set of c classes and $\mathcal{P} := \{1, 2, \dots, N\}$ be the set of N pixels (sites) where measurements $y := \{y_1, y_2, \dots, y_N\}$, the SAR intensities, are available. A labeling $x := \{x_1, x_2, \dots, x_N\}$ is a mapping from \mathcal{P} to \mathcal{L} , *i.e.*, it assigns to each pixel $p \in \mathcal{P}$ a label $x_p \in \mathcal{L}$. Any labeling x can be uniquely represented by a partition of image pixels $P := \{P_l | l \in \mathcal{L}\}$, where $P_l = \{p \in \mathcal{P} | x_p = l\}$ is the subset of pixels to which the label l has been assigned. Since there is an one-to-one correspondence between labelings

x and partitions P , we use these notions interchangeably. By applying a segmentation algorithm to the image y , we get $\hat{x} := \{\hat{x}_1, \hat{x}_2 \dots \hat{x}_N\}$, where \hat{x}_i is the inferred label for the pixel $i \in \mathcal{P}$.

3.2.2 Observation Model

In our problem formulation, we assume conditional independence of the measurements given the labels, *i.e.*,

$$p(y|x) = \prod_{i=1}^N p(y_i|x_i) = \prod_{l=1}^c \prod_{i \in \mathcal{P}_l} p(y_i|\phi^l), \quad (3.1)$$

where $p(\cdot|\phi^l)$ is the density corresponding to class l and ϕ^l the correspondent vector of parameters. The adopted density is a finite Gamma mixture given by

$$p(y_i|\phi^l) := \sum_{s=1}^K \alpha_s^l p(y_i|\theta_s^l), \quad (3.2)$$

where K is the number of Gamma modes in the mixture, i indexes the pixel, θ_s^l is the vector of parameters of the Gamma mode s and class l , and α_s^l is the a priori probability of mode s . We denote $\theta^l := (\theta_1^l, \dots, \theta_K^l)$, $\alpha^l := (\alpha_1^l, \dots, \alpha_K^l)$, and $\phi^l := (\alpha^l, \theta^l)$.

Given that $p(y_i|\theta_s^l)$ is Gamma distributed, we have then

$$p(y_i|\theta_s^l) := \frac{(\lambda_s^l)^{a_s^l}}{\Gamma(a_s^l)} y_i^{a_s^l-1} \exp(-\lambda_s^l y_i), \quad y_i \geq 0, \quad (3.3)$$

where $\theta_s^l := (a_s^l, \lambda_s^l)$. The mean and variance of a random variable with the density (3.3) is, respectively, a_s^l/λ_s^l and $a_s^l/(\lambda_s^l)^2$.

The mixture parameters θ^l are estimated from the data by applying the EM Gamma mixture estimation algorithm described in Section 3.3. The procedure is the same both for the supervised and for the unsupervised approaches.

We now make a brief comment on our choice of the Gamma mixture for modeling the observation densities. Under the assumption of fully developed speckle, the complex radar amplitude is zero-mean circular Gaussian distributed [70]. The average intensity computed over a number of independent random variables with the same density is, thus, Gamma distributed. It happens, however, that in sea SAR imaging one or more of the above assumptions may fail, rendering the Gamma density a poor model for SAR intensity [14]. A line of attack to obtain better models is to use more flexible

3. SEGMENTATION

parametric families, such as the Pearson System [67], [66]. However, in our problem each class density exhibits much more variability than that of accommodated by the the Pearson System. We have very often, for example, multi-modal densities. We should resort, therefore, to a mixture of Pearson System densities, what would lead to complex learning procedures. We have experimentally observed, however, that the Gamma mixture yields very good fittings for real SAR histograms, obtained with a moderately complex learning algorithm. For this reason, we have adopted the Gamma mixture model.

When applying the described Bayesian algorithm to MERIS images, we only need to replace the data model $p(y_i|\theta^l)$ by a multivariate Gaussian density given by:

$$p(y_i|\theta^l) := \frac{1}{(2\pi)^{N/2} |\sum_l|^{1/2}} \exp \left(-\frac{1}{2} (y_i - \mu_l)^T \sum_l^{-1} (y_i - \mu_l) \right) \quad (3.4)$$

In definition 3.4, $y_i := [y_{i1}, y_{iN}]$ are the values of the MERIS channels ($N = 13$, for level 2 processing) and $\theta_l = [\mu_l, \sum_l]$ are the data model parameters. For the MERIS segmentation described in this work, the model parameters have been learned in a supervised way by defining regions representing the classes and computing ML estimators.

3.2.3 Prior

A second assumption we are making is of a local smoothness of the labels in a statistical sense. It is more likely to have neighboring sites with the same label than the other way around. We model this local smoothness with a second order MRF, more specifically, by an MLL model (Ising model in the case of two classes [36]). The Markov property states that

$$p(x_i | x_j, j \in \mathcal{P}) = p(x_i | x_j, j \in \mathcal{N}_i), \quad (3.5)$$

where \mathcal{N}_i is the set of neighbors of site i [36] (see Figure 3.1). If $p(x_i | x_j, j \in \mathcal{N}_i) > 0$, then the Hammersley-Cliffords Theorem states that $p(x)$ has the form of the Gibbs distribution

$$p(x) = \frac{1}{\mathcal{Z}} \exp^{-U(x)}, \quad (3.6)$$

where \mathcal{Z} is the so called partition function and U is the energy function

$$U(x) = \sum_{cl \in C} V_{cl}(x), \quad (3.7)$$

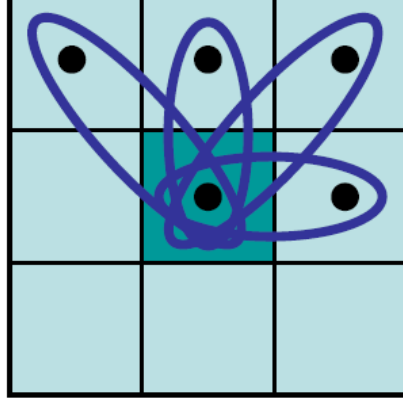


Figure 3.1: 8-pixel-neighbourhood (light green) of pixel i (dark green), with four 2-pixel-cliques represented as blue ellipses.

where C is the set of cliques and $V_{cl}(x)$ is the clique potential defined over clique cl . In this work, we have pair-wise cliques defined on a second-order neighborhood (8 pixels). That is, $C = \{(i, j) : i \in \mathcal{N}_j, j \in \mathcal{N}_i, i > j\}$.

In these conditions, the MLL clique potentials, in the isotropic case, are given by

$$V_{cl}(x_r, x_s) = -\beta \delta(x_r - x_s), \quad (3.8)$$

where $r, s \in cl$, $\delta(x) := I_0(x)$ is the indicator function of set $\{0\}$, and parameter $\beta > 0$ controls the degree of scene homogeneity.

3.2.4 Maximum a Posteriori Estimate

The posterior of the labeling given the observed data is

$$p(x|y) \propto p(y|x)p(x). \quad (3.9)$$

In order to infer x , we adopt the MAP criterion. This amounts to maximize the posterior density of the labeling given the observed data:

$$\hat{x} = \arg \max_x p(x|y), \quad (3.10)$$

3. SEGMENTATION

and is equivalent to minimize the negative logarithm of (3.9). In this sense, we may rewrite the problem in the following way:

$$\hat{x} = \arg \min_x E(x_1, \dots, x_n), \quad (3.11)$$

where

$$E(x_1, \dots, x_N) = -\log p(x|y) + c^{te}, \quad (3.12)$$

and c^{te} denotes an irrelevant constant. From equation (3.9), we have

$$E(x_1, \dots, x_N) = \sum_{p=1}^N E^i(x_i) + \sum_{i,j \in cl} E^{i,j}(x_i, x_j), \quad (3.13)$$

with

$$E^i(x_i) = -\log p(y_i|x_i) \quad (3.14)$$

$$E^{i,j}(x_i, x_j) = -\beta \delta(x_i - x_j). \quad (3.15)$$

3.2.5 Energy Minimization

As already stated, we are concerned with the minimization of $E(x_1, \dots, x_N)$ given by (3.13), which we term energy. For two classes, (*i.e.*, $c = 2$), the global minimum of $E(x_1, \dots, x_N)$ can be computed exactly by applying the graph-cut algorithm described in [68]. This is a consequence of energy being graph-representable, *i.e.*, $E^{i,j}(0,0) + E^{i,j}(1,1) \leq E^{i,j}(0,1) + E^{i,j}(1,0)$ (for details see [68]). For more than two classes, the solution of (3.10) can be approximately computed by the α -Expansion technique [69], also based on graph-cut concepts. This algorithm finds the local minimum of the energy within a known factor of the global minimum.

We now give a brief description of the α -Expansion algorithm. Given a label α , a move from a partition P (with correspondent labeling x) to a new partition P' (with correspondent labeling x') is called an α -Expansion if $P_\alpha \subset P'_\alpha$ and $P'_l \subset P_l$ for any label $l \neq \alpha$. In other words, an α -Expansion move allows any set of image pixels to change their label to α . The algorithm cycles through the labels in \mathcal{P} in some fixed or random order and finds the lowest α -Expansion move from the current labeling. If the expansion move has lower energy than the current labeling, then it becomes the current labeling. The algorithm terminates when no α -Expansion move exist corresponding to a local minimum of the energy.

3.3 EM Algorithm for Fitting a Mixture of Gamma Densities

As stated in the main text of this work, when segmenting real SAR images, the adopted data model for each class is a finite Gamma mixture. For completely defining the data model for each class (for lightness of the notation we have dropped the class index), we need to estimate $2K$ Gamma parameters, $\theta = (\theta_1, \dots, \theta_K)$, with $\theta_s = (a_s, \lambda_s)$, and K a priori probabilities $\alpha = (\alpha_1, \dots, \alpha_K)$. We infer $\phi = (\alpha, \theta)$ by computing its ML estimate from a training set. The ML estimate is computed via an EM algorithm [42]. Fitting a Gamma mixture is addressed in [71]. However, the authors consider N -look SAR images meaning that the underlying random variables are the average of N independent and identically distributed exponential random variables, thus, having a Gamma density but with just one parameter free; if the mean is μ , then the variance is given by μ^2/N . We estimate both the mean and the variance for each Gamma distribution in the mixture, rendering the algorithm more adaptable to real measurements.

The key point in the EM technique is the introduction of the so called missing data z , such that $p(y|\phi) = \int p(y, z|\phi) dz$ and $p(y, z|\phi)$ is easier to manipulate than $p(y|\phi)$. In the particular case of a mixture of densities, we will use as missing data a random variable, z_i , per site, with distribution $p(z_i = s) = \alpha_s$. The missing variables are interpretable as the probability that the s -th Gamma mode is selected at pixel i . The EM algorithm alternates between two steps: the E-step computes the conditional expectation of the logarithm of the complete a posteriori probability function, with respect to the missing variables, based on the actual parameter value. The M-step updates the values of the parameters, by maximizing the expression obtained in the E-step with respect to each parameter on turn, *i.e.*,

$$\text{E-step : } Q(\phi; \phi^t) = E \{ \log p(y, z|\phi) | y, \phi^t \} \quad (3.16)$$

$$\text{M-step : } \phi^{t+1} = \arg \max_{\phi} Q(\phi; \phi^t) \quad (3.17)$$

Denoting

$$w_{si}^t = P(z_i = s | y_i, \phi^t) \quad (3.18)$$

3. SEGMENTATION

and taking into account that $\sum \alpha_s = 1$, then ϕ^{t+1} can be found among the stationary points of the Lagrangean

$$\mathcal{L}(\phi) = \sum_{i=1}^N \sum_{s=1}^K L_{si}(\theta_s, \alpha_s) w_{si}^t + \tau \left(\sum_{s=1}^K \alpha_s - 1 \right), \quad (3.19)$$

with

$$\begin{aligned} L_{si}(\theta_s, \alpha_s) &= \log(\lambda_s^{a_s}) - \log[\Gamma(a_s)] \\ &\quad + \log(y_i^{a_s-1}) - \lambda_s y_i + \log(\alpha_s), \end{aligned} \quad (3.20)$$

where τ denotes a Lagrange multiplier. The expression for w_{si}^t (see [72]) is given by

$$w_{si}^t = \frac{\alpha_s^t p(y_i | \theta_s^t)}{\sum_{r=1}^K \alpha_r^t p(y_i | \theta_r^t)}. \quad (3.21)$$

In the M-step, we obtain a closed solution for the updating of the a priori probabilities α_i 's, by differentiating \mathcal{L} in order to the unknown parameters and setting the derivatives to zero. Numerical iteration is needed, however, for determining parameters a_i 's and λ_i 's of the Gamma densities. Expression (3.22) gives the update expression for α_i 's.

$$\alpha_s^{t+1} = \frac{1}{N} \sum_{i=1}^N w_{si}^t. \quad (3.22)$$

Equation (3.23) and (3.24) give the update expressions for the parameters λ_i 's and a_i 's.

$$\lambda_s^{t+1} = \frac{a_s^t \sum_{i=1}^N w_{si}^t}{\sum_{i=1}^N y_i w_{si}^t}, \quad (3.23)$$

$$a_s^{t+1} = \Psi^{-1} \left[\frac{\log(\lambda_s^t) \sum_{i=1}^N w_{si}^t + \sum_{i=1}^N \log(y_i) w_{si}^t}{\sum_{i=1}^N w_{si}^t} \right], \quad (3.24)$$

where

$$\Psi(a_s) = \frac{\Gamma'(a_s)}{\Gamma(a_s)}, \quad (3.25)$$

is the psi function. We refer to the Appendix B of [73] for a very fast Newton procedure to compute the inverse of the psi(\cdot) function. Expressions (3.23) and (3.24) are iteratively recomputed until convergence is obtained, starting from initial values computed from the observed data y . The initial parameter values are calculated in such a way, that the initial probability function is a sum of equidistant Gammas that span the most representative data range. The EM scheme converges in a few tens of iterations.

3.4 Estimation of Parameter β

In this work, we consider three different techniques to determine the smoothness parameter β : a new EM method hereafter introduced that uses loopy belief propagation (LBP) and the classical LSF and CD methods. Because LSF and CD assume the existence of labeled data, we have conceived an iterative labeling-estimation scheme, which alternates between a labeling step and an estimation step until the convergence of β is attained. On the contrary, the EM estimation algorithm, that we have called “Loopy- β -Estimation”, is a one-shot technique. In the following sections, we briefly review the LSF and CD methods and provide a detailed description of the Loopy- β -Estimation method. In this section, the class parameters $\phi := (\phi^1, \phi^2, \dots, \phi^c)$ are assumed known.

3.4.1 Least Squares Fit

This procedure for parameter estimation in MRF, described in detail in [36], is based in the following equation that holds for the MLL model, for every pixel p , with neighborhood \mathcal{N}_p , and for every label pair $x_p, x'_p \in \mathcal{L}$:

$$\begin{aligned} \beta [n(x_p) - n(x'_p)] &= \log \left(\frac{p(x_p | x_{\mathcal{N}_p}, y)}{p(x'_p | x_{\mathcal{N}_p}, y)} \right) \\ &\quad - (E^p(x'_p) - E^p(x_p)), \end{aligned} \quad (3.26)$$

where $n(x_p)$ is the number of pixels in the set \mathcal{N}_p with the same label as x_p and $x_{\mathcal{N}_p} := \{x_i, i \in \mathcal{N}_p\}$. We use histograms to estimate the joint probabilities $p(x_p | x_{\mathcal{N}_p}, y)$ and $p(x'_p | x_{\mathcal{N}_p}, y)$ in (3.26): assuming that there are a total of M distinct 3x3 blocks in the image lattice with a given label configuration $x_{\mathcal{N}_p}$, then we take

$$\hat{p}(x_p | x_{\mathcal{N}_p}, y) = \frac{\mathcal{H}(x_p | x_{\mathcal{N}_p}, y)}{M}, \quad (3.27)$$

where $\mathcal{H}(x_p | x_{\mathcal{N}_p}, y)$ is the number of times that a particular 3x3 configuration $(x_p | x_{\mathcal{N}_p}, y)$ occurs. The expression is then evaluated for a number of distinct combinations of x_p, x'_p and $x_{\mathcal{N}_p}$ in order to obtain an over-determined linear system of equations that is solved in order to β .

3. SEGMENTATION

3.4.2 Coding Method

In this method the key idea (see [36]) is to partition the set \mathcal{P} into sets $\mathcal{P}^{(k)}$, called codings, such that no two sites in one $\mathcal{P}^{(k)}$ are neighbors. In the present work, the neighborhood \mathcal{N}_p is of 2nd order thus yielding four codings. As the pixels in $\mathcal{P}^{(k)}$ are not neighbors, the variables associated with these pixels, given the labels at all other pixels, are mutually independent under the Markovian assumption. The following simple product is thus obtained for the likelihood:

$$p^{(k)}(x|\beta, y) = \prod_{p \in \mathcal{P}^{(k)}} p(x_p | x_{\mathcal{N}_p}, \beta, y), \quad (3.28)$$

Maximizing (3.28) in order to β gives the coding estimate $\hat{\beta}^{(k)}$. Although it is not clear how to combine the results optimally, the arithmetic average, as suggested in [36], is an intuitive scheme that was adopted in this work.

3.4.3 Loopy- β -Estimation

We are seeking $\hat{\beta}_{ML} = \arg \max_{\beta} p(y|\beta)$, the ML estimate of the smoothness parameter β . Based on the fact that the marginal density $p(y|\beta)$, the so-called evidence, is a sum over the missing labels x , *i.e.*,

$$\begin{aligned} p(y|\beta) &\equiv \sum_x p(y, x|\beta) \\ &= \sum_x p(y|x) p(x|\beta), \end{aligned} \quad (3.29)$$

we develop an EM algorithm [42] for the ML estimation of the parameter β . The EM algorithm alternates between two steps: the E-step computes the conditional expectation of the logarithm of the complete a posteriori probability function, with respect to the missing variables, based on the actual parameter value; the M-step updates the value of the parameter, by maximizing the expression obtained in the E-step with respect to that parameter. We now derive the E-step and the M-step.

E-step:

$$Q(\beta; \beta_t) = E[\log p(y, x|\beta)|y, \beta_t] \quad (3.30)$$

$$= E[\log p(y|x)|y, \beta_t] \quad (3.31)$$

$$+ E[\log p(x|\beta)|y, \beta_t]. \quad (3.32)$$

Recalling that the MLL prior is given by

$$p(x|\beta) = \frac{1}{\mathcal{Z}(\beta)} \exp \left[\beta \sum_{i,j \in cl} \delta(x_i - x_j) \right], \quad (3.33)$$

with

$$\mathcal{Z}(\beta) = \sum_x \exp \left[\beta \sum_{i,j \in cl} \delta(x_i - x_j) \right], \quad (3.34)$$

we obtain, up to an irrelevant constant,

$$Q(\beta; \beta_t) = -\log \mathcal{Z}(\beta) + \beta \sum_{i,j \in cl} E[\delta(x_i - x_j) | y, \beta_t]. \quad (3.35)$$

M-step:

$$\beta_{t+1} = \arg \max_{\beta} Q(\beta, \beta_t). \quad (3.36)$$

The stationary points of \mathcal{Q} are the solution of

$$\begin{aligned} \frac{\partial Q}{\partial \beta} &= -\frac{\partial \log [\mathcal{Z}(\beta)]}{\partial \beta} \\ &+ \sum_{i,j \in cl} \sum_{x_i, x_j \in \mathcal{L}} \delta(x_i - x_j) p(x_i, x_j | y, \beta_t) = 0. \end{aligned} \quad (3.37)$$

By introducing expression (3.34) into (3.37) and if we consider that $\delta(x_i - x_j)$ takes non-zero values only for equal labels, we obtain

$$\begin{aligned} \frac{\partial Q}{\partial \beta} &= \sum_{i,j \in cl} \sum_{k=1}^c p(x_i = k, x_j = k | y, \beta_t) \\ &- p(x_i = k, x_j = k | \beta_t) = 0. \end{aligned} \quad (3.38)$$

Since computing exact marginal distributions is infeasible in our case, we replace them by pseudo-marginals using BP. This approach has been successfully applied in problems of approximate parameter learning in discriminative fields [74]. BP is an efficient iterative algorithm in which local messages are passed in graphical models.

3. SEGMENTATION

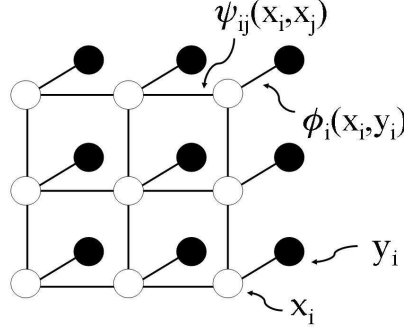


Figure 3.2: Lattice representing the pairwise MRF.

For singly-connected (loop free) pairwise MRFs, the two-node beliefs will correspond to the exact two-node marginal probabilities. In our case, however, the graph that corresponds to the MRF contains cycles, preventing the basic BP algorithm to be applied. We resort to a slightly modified version called loopy belief propagation. In practice, this algorithm has often delivered good results [43]. We approximate the marginal probabilities with the two-node beliefs $b_{ij}(x_i, x_j)$ and $b_{ij}^y(x_i, x_j)$. These will provide approximations respectively for the marginals $p(x_i, x_j|\beta_t)$ and $p(x_i, x_j|y, \beta_t)$. By doing so, the M-Step of our EM algorithm is given by the sum of the differences between the two node beliefs that take the evidence y into consideration and those that do not make use of y :

$$\frac{\partial Q}{\partial \beta} = \sum_{i,j \in cl} \sum_{k=1}^c b_{ij}^y(k, k) - b_{ij}(k, k) = 0. \quad (3.39)$$

Figure 3.2 depicts the graph that represents our pairwise MRF for computing the two-node beliefs. In the square lattice, $\psi_{ij}(x_i, x_j)$ stands for the interaction potential that penalizes every dissimilar pair of neighboring labels, and $\phi(x_i, y_i) = p(y_i|x_i)$ represents the statistical dependency between the labels x_i and the measurements y_i . For computing $b_{ij}(x_i, x_j)$, $\phi(x_i, y_i)$, is set to a constant value, making the result independent of the data values y .

We solve (3.39) by a line search type algorithm, ensuring that $\frac{\partial^2 Q}{\partial^2 \beta} \leq 0$, thus corresponding to a maximum of Q .

3.4.4 A few Remarks about the Vector of Parametres ϕ

In the previous section, we have considered that the class parameter vector ϕ is known and only the smoothness parameter β is to be inferred. However, still using the beliefs computed by LBP, the vector ϕ could have been inferred simultaneously with β by including in the Q function the additive term (3.31) corresponding to the class densities. We would have obtained

$$\begin{aligned} Q(\phi; \phi_t, \beta_t) &= E[\log p(y|x)|y, \phi_t, \beta_t] \\ &= \sum_{i=1}^N \sum_{l=1}^c \log p(y_i|\phi^l) p(x_i = l|y, \phi_t, \beta_t), \end{aligned}$$

where the probabilities $p(x_i = l|y, \phi_t, \beta_t)$ are given by the LPB method. The **M-step** would consist then in two decoupled maximizations; one with respect to β and another with respect to ϕ . This approach is, however, beyond the scope of this work. Nevertheless, we present in Section 3.6 an unsupervised algorithm, which is suboptimal but faster than the LBP based EM algorithm aimed at the inference of both the parameters β and ϕ .

An alternative to the proposed EM scheme based on LPB is using Monte Carlo techniques to cope with the difficulty in computing the **E-step** and the partition function Z [75], [76], [77]. Supported on the performance of the LBP, we believe, however, that the EM scheme based on LPB is, for the present problem, much more faster than the Monte Carlo based techniques.

3.5 Supervised Segmentation

In this section, we introduce two supervised algorithms aimed at the segmentation of sea SAR images. In both algorithms, the first step is the estimation of the class parameters used in the data model. This is done by asking the user to define representative regions of interest (ROI) in the image. Once the regions are defined, different approaches may be followed: if a Gamma mixture is assumed for the observed data, as in the case of SAR images, the EM class parameters estimation algorithm described in Section 3.3 is applied to infer the class conditional densities. If we are segmenting small sub-scenes and the radar range spreading loss has been compensated in the underlying SAR images, one single Gamma function per class often provides a good modeling for the

3. SEGMENTATION

SAR intensities. In this case, a common ML Gamma estimator is used instead of the EM procedure. After this step, the data model is considered to be known and is used thereafter.

The pseudo-code for two supervised algorithms is presented in Algorithm-1 and Algorithm-2. Algorithm-1 is of generalized likelihood type [78] implementing an iterative labeling scheme with two steps being performed alternately: the β -Estimation and the segmentation. Algorithm-2 is a one-shot procedure that performs β -Estimation using the Loopy β -Estimation method described in Section 3.4.3.

Algorithm 1 Supervised Segmentation Using LSF/CD β -Estimation

Require: Initial parameter $\hat{\beta} = \beta_0$ and estimated class parameters $\hat{\phi}$

- 1: Compute $\text{eLabel} = E^p(x_p)$ for every pixel p using $\hat{\phi}$
 - 2: **while** $|\Delta\hat{\beta}| \leq \delta$ or $\text{nrIterations} < \text{NrIterationsMax}$ **do**
 - 3: Compute $\hat{x} = \alpha\text{-Expansion}(\hat{\beta}, \text{eLabel})$
 - 4: Compute $\hat{\beta} = \beta\text{-Estimation}(\hat{x}, \text{eLabel})$ {LSF or CD}.
 - 5: **end while**
 - 6: **return** $(\hat{x}, \hat{\beta})$
-

Algorithm 2 Supervised Segmentation Using Loopy- β -Estimation

Require: estimated class parameters $\hat{\phi}$

- 1: Compute $\text{eLabel} = E^p(x_p)$ for every pixel p using $\hat{\phi}$
 - 2: Compute $\hat{\beta} = \text{Loopy-}\beta\text{-Estimation}(\text{eLabel})$
 - 3: Compute $\hat{x} = \text{GraphCut-Segmentation}(\hat{\beta}, \text{eLabel})$
 - 4: **return** $(\hat{x}, \hat{\beta})$
-

3.6 Unsupervised Segmentation

The unsupervised method, stated in “Algorithm-3” is an improvement of the supervised algorithms described in the previous sections. The main difference is that the data model is not considered to be known but is also iteratively estimated along with the smoothness parameter and the segmentation. The scheme needs a rough initialization of the data model parameters. We computed this initialization by fitting an EM Gamma mixture to the complete data.

As our EM algorithm automatically eliminates unnecessary modes, we start with an overestimate of K , the number of modes in the mixtures. In our experiments with real data, the maximum number of modes we got was four.

Then, different strategies are possible. In the experiments reported in the next section, when considering $c = 2$ classes, we have assigned the mode with a lower mean value to one of the classes and the remaining modes to the other class.

In each iteration, we compute the ML estimate of the vector ϕ based on the previous segmentation, compute the new segmentation, and finally the new value of β . The algorithm may use any of the three β -parameter estimation methods and is applicable to an optional number of classes. The algorithm stops when both the parameter β and the class parameters ϕ converge to stable values.

Algorithm 3 Unsupervised Segmentation

Require: arbitrary parameter $\hat{\beta} = \beta_0$, initial class parameters $\hat{\phi} = \phi_0$ (EM Gamma Mixture Estimation)

- 1: Compute $eLabel_0 = E^p(x_p)$ for every pixel p , using ϕ_0
 - 2: Compute initial labeling
 $\hat{x} = x_0 = \alpha\text{-Expansion}(\beta_0, eLabel_0)$
 - 3: **for** stop criterium is not met **do**
 - 4: Compute $\hat{\phi} = \text{ML-Estimation}(\hat{x})$
 - 5: Compute $eLabel = E^p(x_p)$ for every pixel p , using $\hat{\phi}$
 - 6: Compute $\hat{x} = \alpha\text{-Expansion}(\hat{\beta}, eLabel)$
 - 7: Compute $\hat{\beta} = \beta\text{-Estimation}(\hat{x}, eLabel)$ {use LSF, CD or Loopy}.
 - 8: **end for**
 - 9: **return** $(\hat{x}, \hat{\beta}, \hat{\phi})$
-

3.7 Results

This section presents results of applying the proposed methodology to simulated and real SAR images, as well as some considerations regarding time complexity of the algorithms.

3. SEGMENTATION

3.7.1 Simulations

We have performed simulations corresponding to Gamma data terms with two classes, and evaluated the overall accuracies of the obtained segmentations using Algorithms-1, -2 and -3. We also illustrate in detail the EM Gamma mixture estimation algorithm, by applying it to an example of simulated data.

3.7.1.1 Segmentation Results with Gamma Data Term

In order to compare the performance of the three proposed methods, we have tested Algorithms 1, 2 and 3 on simulated data generated accordingly to the model defined in 3.2. We used two classes ($c = 2$), and one Gamma mode ($K = 1$) for each class. Figure 3.3 (a) represents the image of the classes. The parameters of the Gamma mode for each class, $\theta^1 = (a^1, \lambda^1)$ and $\theta^2 = (a^2, \lambda^2)$, where chosen in order to obtain a mean value of $\mu^1 = 5$ and $\mu^2 = 9$, respectively (with $\mu = a/\lambda$ as described in Section 3.2.2). Then, the parameters were changed a number of times, generating a set of simulated data, in order to increase the difficulty of the segmentation process. The parameters were changed in a way that the mean values remained the same, but the variances $\sigma^2 = a/(\lambda^2)$ were successively increased. We applied Algorithm-1, with LSF and CD methods, Algorithm-2, and Algorithm-3 with Loopy- β -Estimation to each simulated data. Furthermore, for comparison, the images were also segmented tuning the beta value manually, and for the case that no prior was used ($\beta = 0$). Figure 3.3 shows the segmentation results obtained for the specific simulated data with a value of $\sigma = 2.6$. As we can see from the $\beta = 0$ result, this is a hard problem, on which LSF and CD fails the inner structures, but Loopy- β -Estimation provides better results, both in the supervised as in the unsupervised approach. This behavior is further confirmed by the results in Figure 3.4. The graphic depicts the OA's obtained with the six different segmentation processes referred above, when applied to the set of simulated data. Each simulated data corresponds to a different σ value.

We have also tested the proposed algorithms in images generated by adding Gamma noise to a ground-truth similar to an oil patch (see Figure 3.5). Two images, Image A and Image B, with the histograms depicted in Figure 3.5, corresponding to different segmentation difficulty levels are segmented. The best segmentation possible in this framework, achieved by tuning the β value manually, and the segmentation obtained

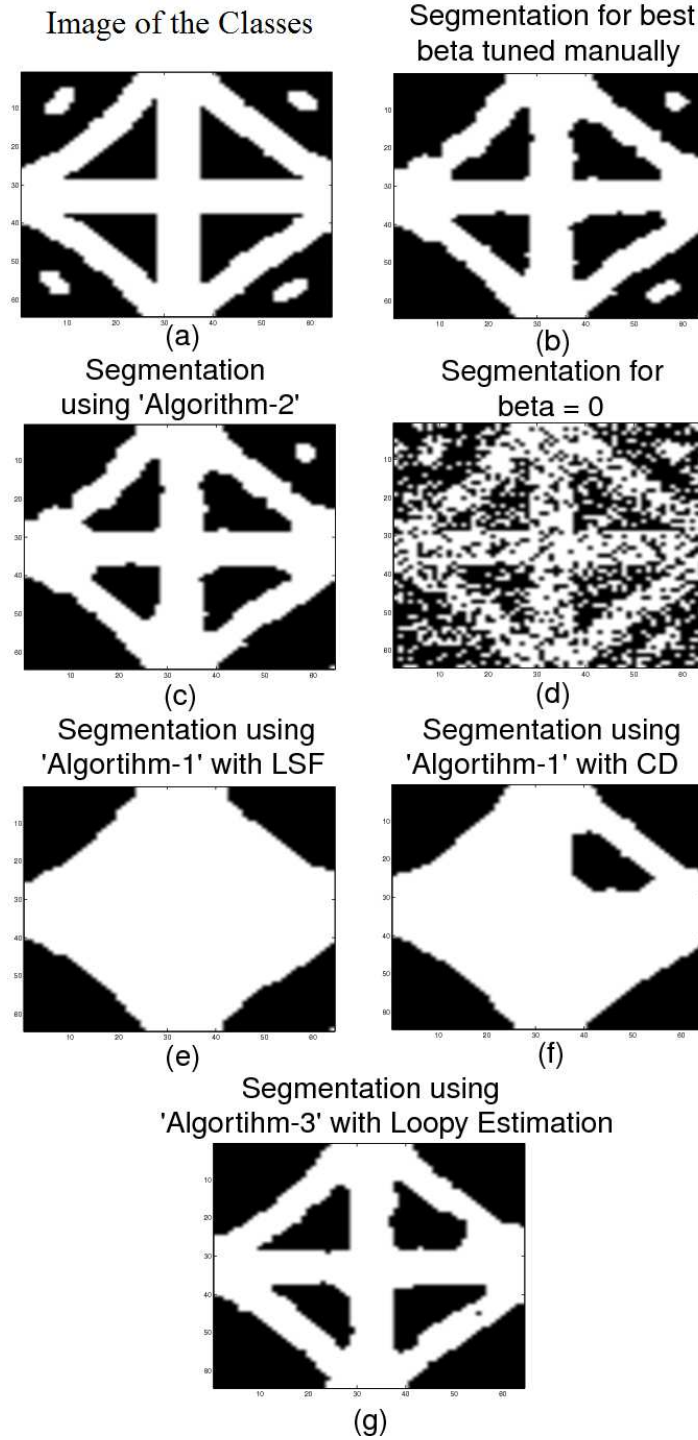


Figure 3.3: Image of the classes, and results of different segmentation processes, for an image generated using a Gamma data term with one mode for each class. The parameters of the Gamma modes, $\theta^1 = (a^1 = 3.695, \lambda^1 = 0.739)$ and $\theta^2 = (a^2 = 11.982, \lambda^2 = 1.331)$, where chosen in order to obtain $\mu^1 = 5$, $\mu^2 = 9$, and $\sigma^1 = \sigma^2 = 2.6$. Notice the good performance of Algorithm-2 and Algorithm-3, implementing the Loopy- β -Estimation.

3. SEGMENTATION

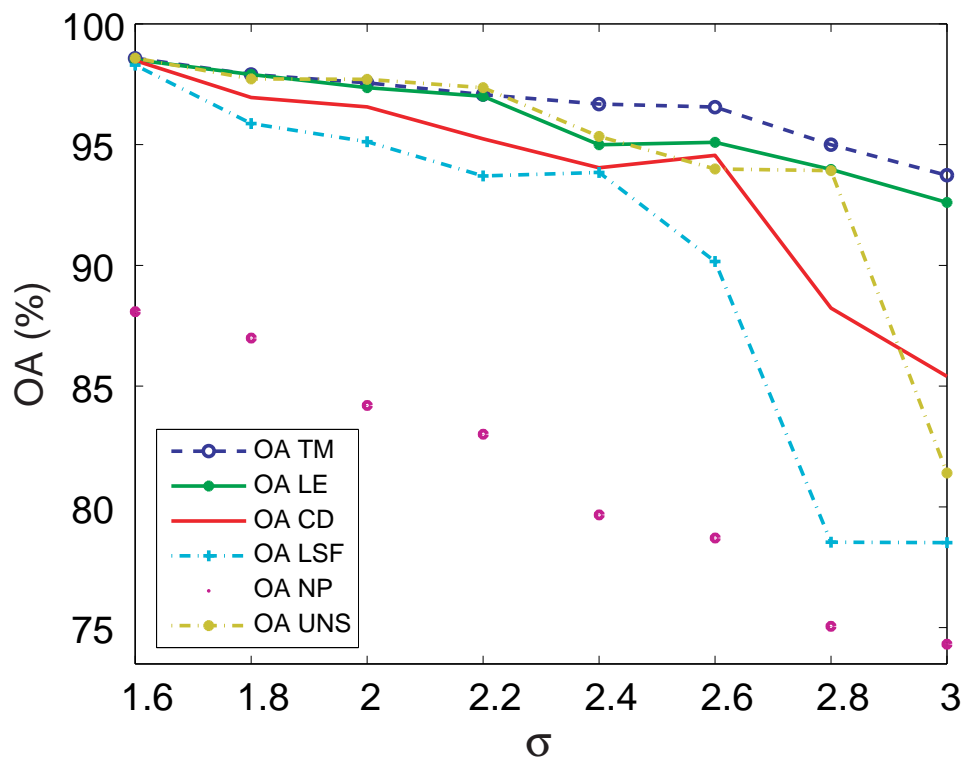


Figure 3.4: OA for images generated using a Gamma data term, with increasing σ values: TM := for β tuned manually; LE := Algorithm 2, using Loopy Estimation; LSF := Algorithm-1 using LSF; CD := Algorithm-1 using CD, NP := no prior and UNS := Algorithm-3 using Loopy Estimation.

with no prior information (setting $\beta = 0$) are also displayed for comparison. Figure 3.6 shows the results obtained for Image A and Figure 3.7 the results obtained for Image B. For Image A, the segmented images using Algorithm-1, with CD and with LSF, are not shown, as they are almost equal to the image segmented with Algorithm-2. For Image B, Algorithm 3 has not provided good results and the segmentation is not displayed. The bad performance of Algorithm-3 in this case is caused by a poor initialization of the class parameters, due to the complete overlapping from the oil and the water histograms.

3.7.1.2 EM Algorithm for Gamma Mixture

In this subsection, we illustrate the behavior of the EM algorithm designed to infer Gamma mixtures. For details on the theoretical issues, we refer to Section 3.3. In Figure 3.8, we can see the ground-truth used for simulating the image and the generated image, according to the densities shown in Figure 3.9. The two classes, oil and water have been modeled respectively by a mixture of two Gamma functions ($K = 2$) and a mixture of three Gamma functions ($K = 3$). For this particular case, we have selected a “Region of Interest” (ROI) containing 178 pixels for representing the water and a ROI containing 142 pixels for representing the oil. After 20 iterations of the EM algorithm, we obtained the approximations for the probability distributions depicted in Figure 3.10 and Figure 3.11. The obtained results are quite reasonable having in mind the low number of samples used.

3.7.2 Real Images

We first illustrate the application of Algorithm-1 in two different scenarios, both regarding the segmentation of more than two classes in marine images. In the first scenario, the scene covers several oil platforms in the Norwegian and British sector of the North Sea, and we could segment the oil spill, the water and the platform. In the second scenario the algorithm has been applied to a pair of simultaneously acquired Envisat MERIS/ASAR images containing an oil spill, and a third class, related to high concentrations of chlorophyll could also be identified.

We have then tested the proposed methodology with three real SAR images for the special purpose of oil spill detection. For this type of application, an unsupervised

3. SEGMENTATION

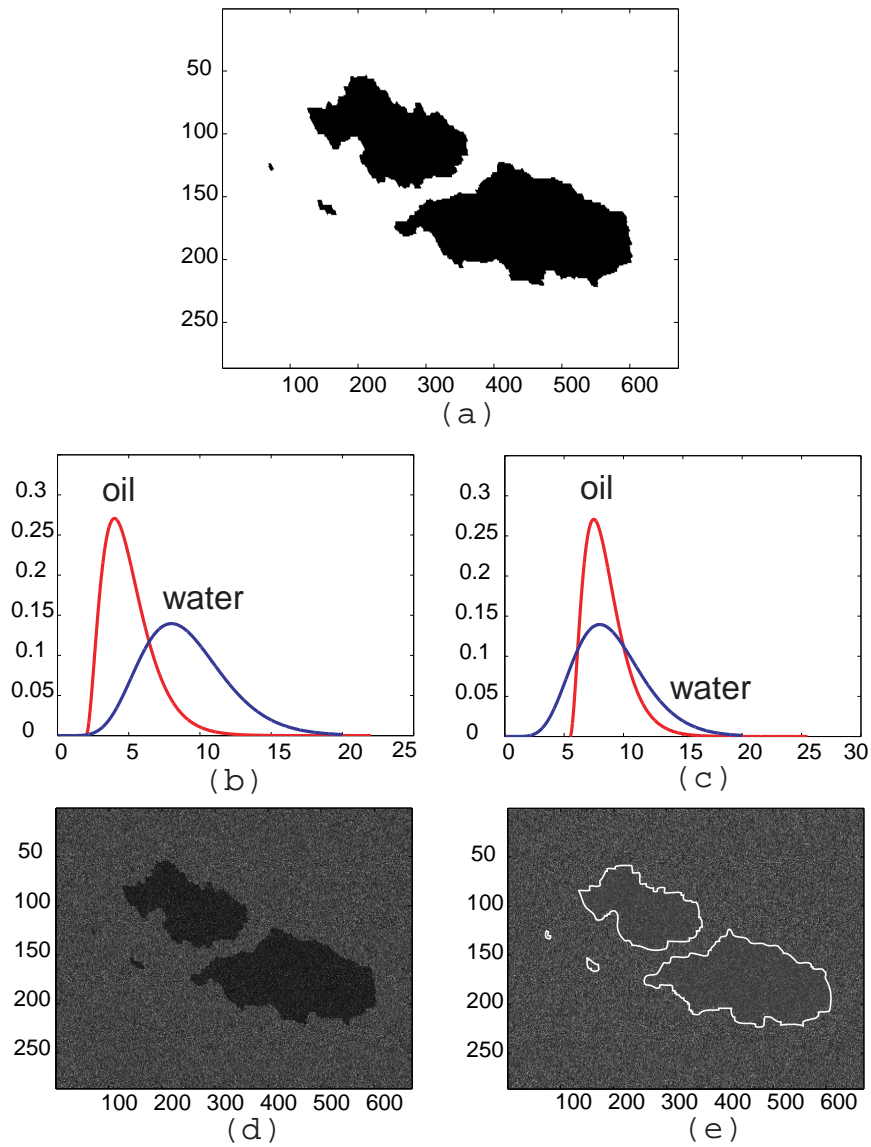


Figure 3.5: Gamma data term: (a) Image of classes, (b) Histogram of Image A, with one mode ($K = 1$), (c) Histogram of Image B, with one mode ($K = 1$), (d) Image A, (e) Image B with superimposed delimiting line, for better visualization.

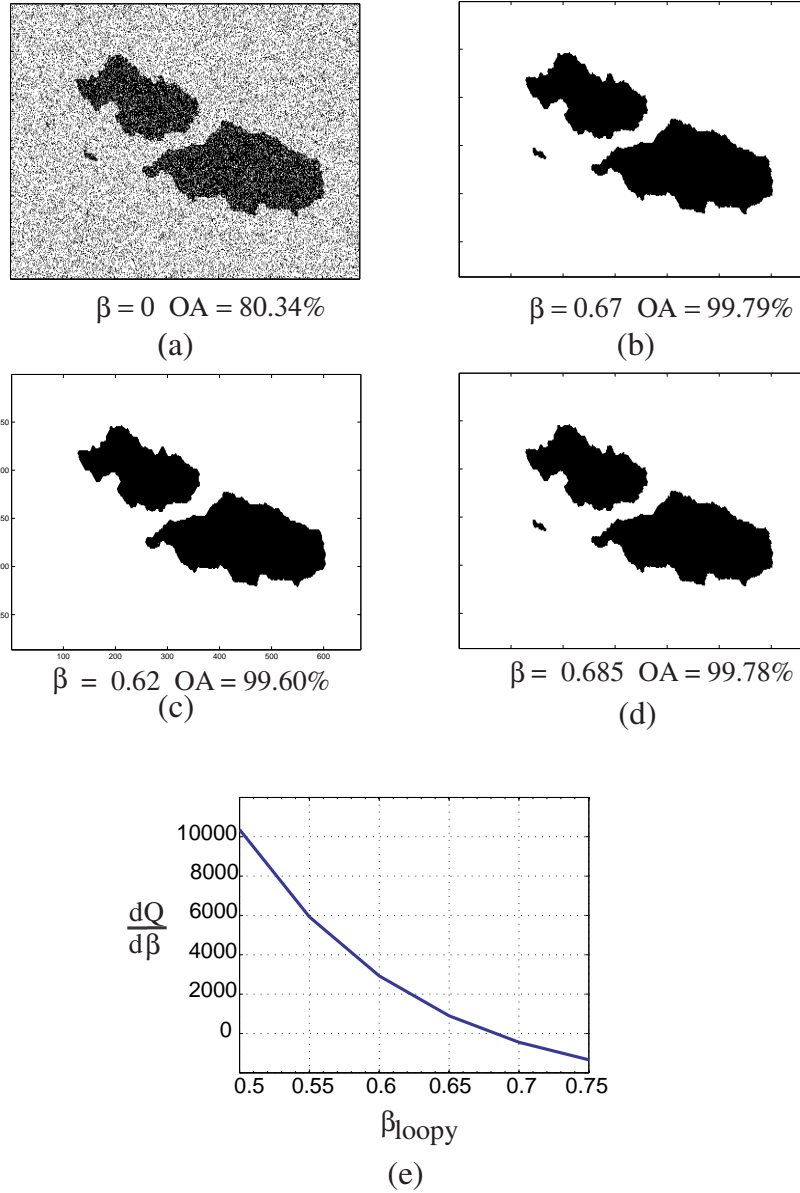


Figure 3.6: Segmentation results for Image A: (a) No prior information, (b) β value tuned manually, (c) Segmentation using Algorithm-3 with Loopy- β -Estimation, (d) Segmentation using Algorithm-2 (Algorithm-1 provided the same results with only 0.1% difference in OA), (e) graph depicting the β estimation in Algorithm-2.

3. SEGMENTATION

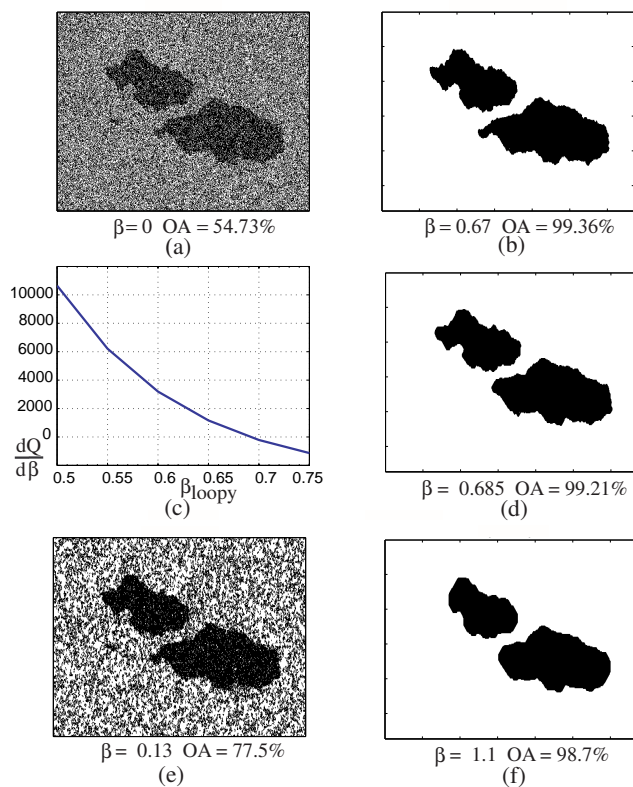


Figure 3.7: Segmentation results for Image B: (a) No prior information, (b) β value tuned manually, (c) graph depicting β estimation using Algorithm-2, (d) Segmentation using Algorithm-2, (e) Segmentation using Algorithm-1 with LSF and (f) Segmentation using Algorithm-1 with CD.

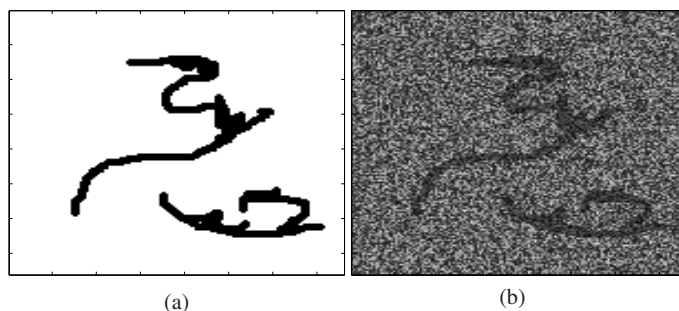


Figure 3.8: (a) Image of the classes used for simulating an oil spill. Black represents oil and white water; (b) Simulated SAR image.

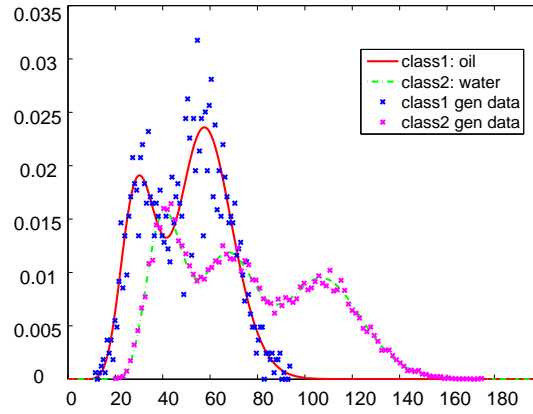


Figure 3.9: Probability functions used to generate the simulated image depicted in Figure 3.8 (b), with superimposed histogram of generated data set. A three modes ($K = 3$) function for water and two modes ($K = 2$) function for oil was used.

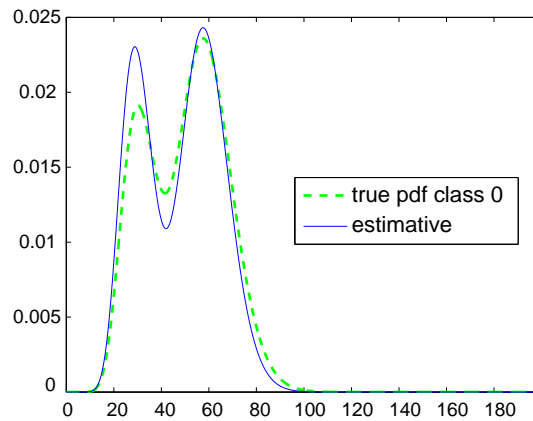


Figure 3.10: True and estimated class densities for oil, when using a ROI of 142 samples.

3. SEGMENTATION

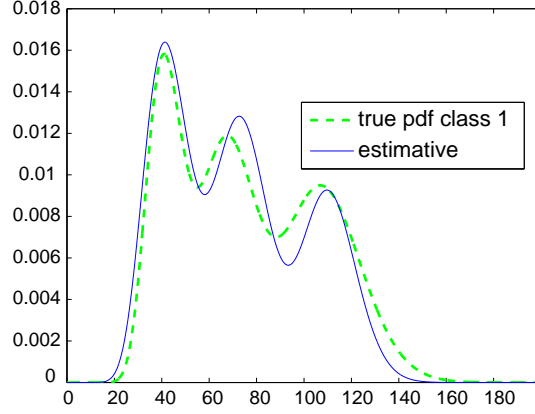


Figure 3.11: True and estimated class densities for water, when using a ROI of 178 samples.

algorithm is more indicated, and so we decided to apply Algorithm-3. Because Loopy Estimation has proven to be an effective method in the simulations, we have chosen Algorithm-3 with Loopy Estimation. Nevertheless, in order to have a comparison, the unsupervised approach versus the supervised approach, we also applied Algorithm-2 to two of the images. In oil spill detection, the number of classes is typically set to $c = 2$, although more classes can be considered if we are interested in distinguishing other phenomena occurring at the same time in the region of interest. The application of the algorithms is straightforward: the key idea, like in most state-of-the-art oil spill detection methods (see for example [13]), is to partition the image in tiles and run the algorithm separately for each part. This step is preceded by the application of a landmask to the image, what can be done using external coastline information or by adopting some coastline self-extraction procedure. After the segmentation of each tile, a procedure for grouping patches detected on the tile borders should be carried on. Another possibility to increase segmentation coherency in the borders is to define overlapping tiles or to force continuity to some degree on the estimated class and/or smoothness parameters from one tile to the next. Nevertheless, at the moment we are not doing this and these are considered future possible improvements to our methodology. We segmented oil spills contained in three different scenes, described in the following subsections.

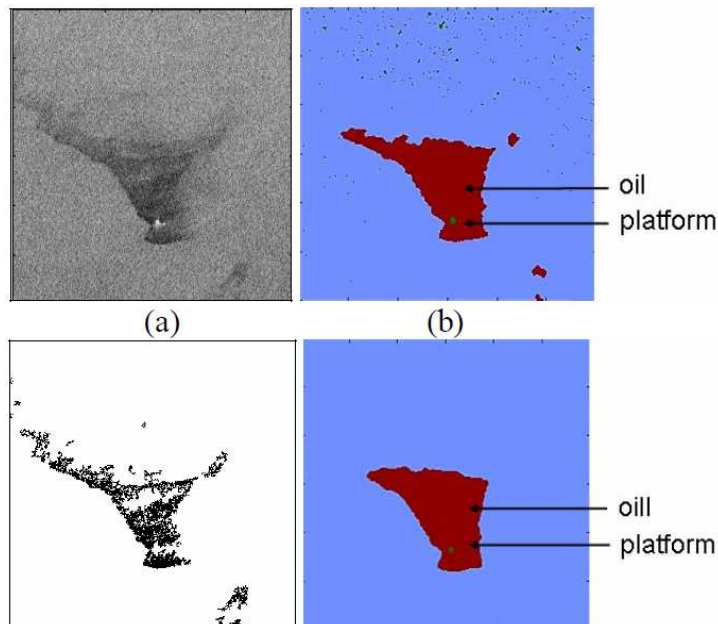


Figure 3.12: (a) ERS-1 image: intensity values (b) Segmentation with LS; (c) Segmentation using “Adaptive Thresholding” followed by morphological operations (as described in [23]) (d) Segmentation with CD.

3.7.2.1 Segmentation of an ERS-1 image using Algorithm-1

We segmented a real ERS-1 SAR image fragment (frame 2367, orbit 17211) that has been acquired on the 30th October 1994 over the North Sea. A class has been assigned to “oil”, a class to “water” and a class to “platform” and then the class parameters have been learned using the supervised method described in [3]. Figure 3.12 displays the obtained results after applying Algorithm-1.

The image has also been segmented by applying the method described in [23] for comparison. Following the described method, an image pyramid of two levels was created and the threshold was set adaptively based on the PMR value calculated in a local window of 100 pixels x 100 pixels. After the thresholding, and following the methodology proposed in [23], morphological operators have been applied in order to remove segmented patches with area less than 50 pixels.

3. SEGMENTATION

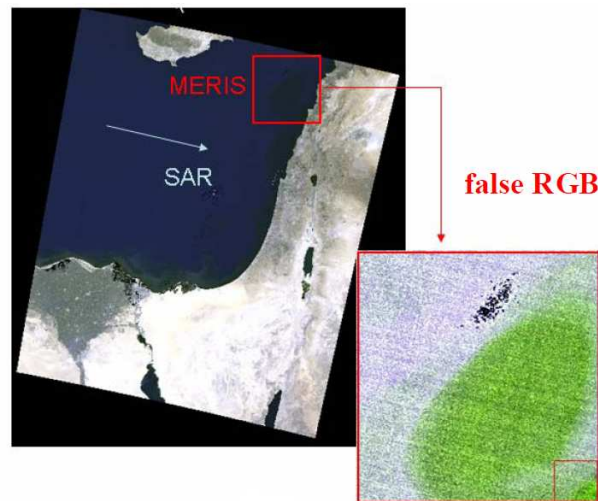


Figure 3.13: Quicklook of the MERIS image acquired in simultaneous with an ASAR image. The picture shows the center of the collocated ASAR scene, as well as a zoom of the area of interest of the MERIS image, namely the part containing the possible signature of the oil spill. The zoom of the area of interest is displayed in RGB, where the three channels are coded based on a mixture of the MERIS bands.

3.7.2.2 Segmentation of MERIS/ASAR pair using Algorithm-1

In the following, the results of applying “Algorithm-1” to a pair of simultaneously acquired Envisat MERIS/ASAR images containing an oil spill are also depicted. The image pair, a MERIS Full Resolution level 2 and an ASAR Image Mode image has been acquired on the 19th July 2004, in the ocean between Cyprus and Lebanon (see Figure 3.13). The occurrence of the oil spill (centered on $\approx 33^\circ\text{N}$, $33^\circ39'\text{E}$) was documented on the Oceanides project database and it was expected to find evidence of the circa 10 km long dark patch in the cloud-free MERIS image. In fact, a dark patch of the expected size, form and orientation was detected on the MERIS image (see zoom of Figure 3.13) but centered on $\approx 34^\circ28'\text{N}$, 35°E . The pixels flagged as clouds have been masked before the segmentation process. Although we can not conclude that the segmented patch is the oil spill due to the location difference, the segmentation results are reported in Figure 3.14 and Figure 3.15.

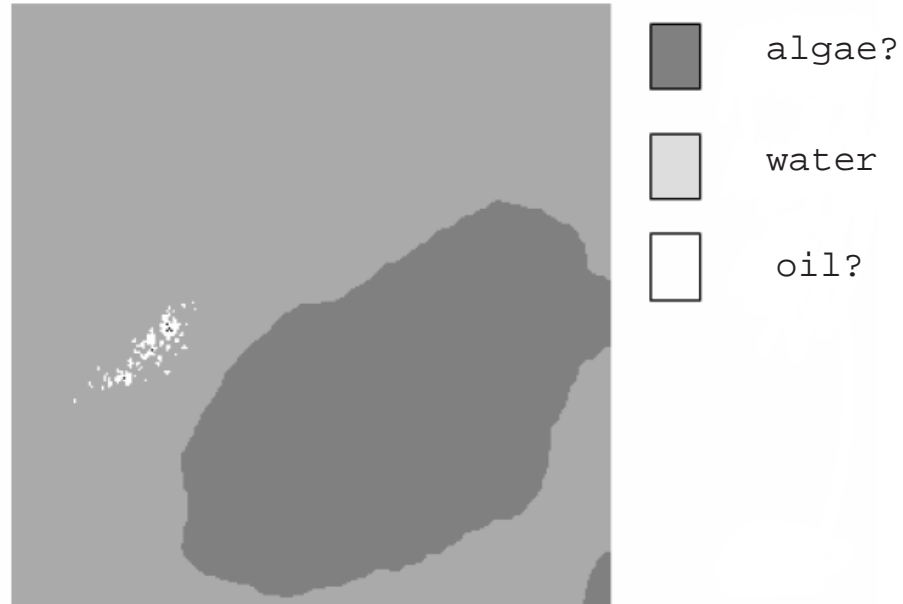


Figure 3.14: MERIS image segmentation using Algorithm-1 using multivariate Gaussian distribution as data model.

3.7.2.3 Segmentation of an ERS-1 image using Algorithm-2 and -3

We have segmented part of an ERS-1 image from the Sicily Channel, Italy, that has been acquired on the 30th January of 1992. This image is referred in the ESA web pages regarding oil slicks http://earth.esa.int/ew/oil_slicks/ and contains three oil slicks, along with information regarding wind direction and intensity and existence of ships, ship wakes, natural oil films and currents.

Figure 3.16 provides a quicklook of the scene with two squares superimposed: the larger representing the part to be segmented and the smaller representing a part used for wind estimation. Figure 3.17 provides zooms of the referred squares. By applying the Radon Transform [79] to the smaller square, a rough estimation of the direction has been calculated and is depicted in the image. The direction was consistent with the measured value reported in the url site and is at the origin of the well-known “feathering” effect that can be observed in this linear spill. We have computed the backscattering values of the image, by performing calibration using the ESA provided BEST software (<http://earth.esa.int/services/best/>) and then applied Algorithm-3 with Loopy-

3. SEGMENTATION

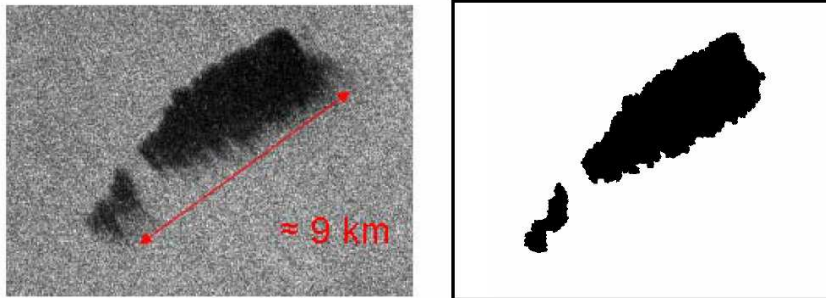


Figure 3.15: ASAR image segmentation with Algorithm 1 using Gamma mixture data model.

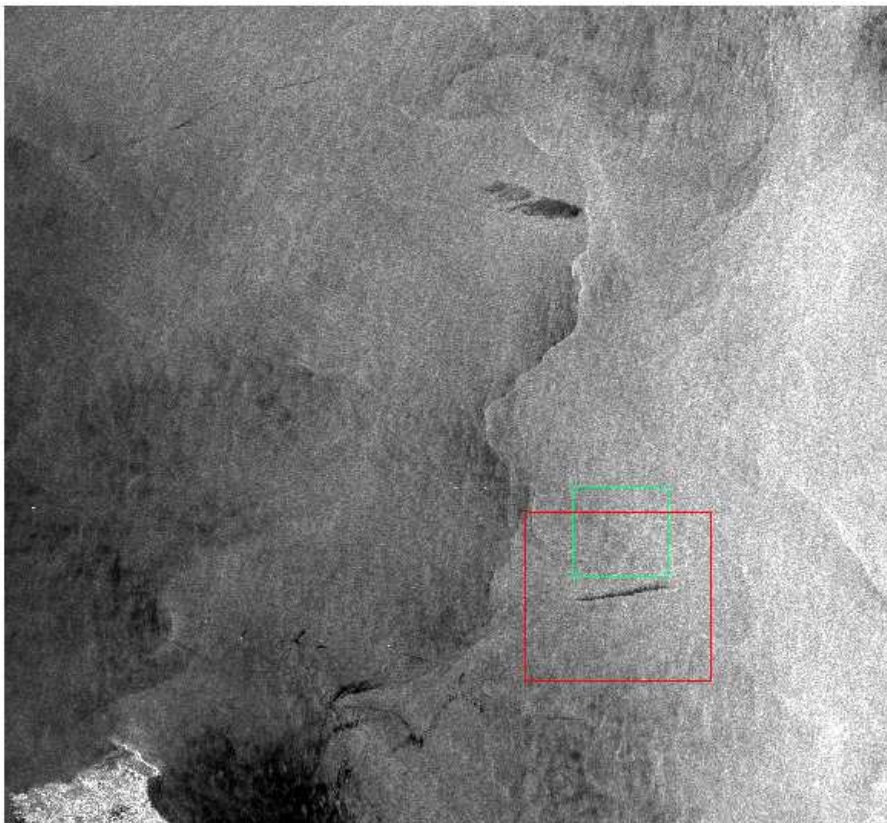


Figure 3.16: ERS-1 image from the Sicily Channel, Italy, acquired on the 30th January 1992. The smaller and larger squares are sub-scenes that have been used respectively to estimate the wind direction and to apply our algorithm.

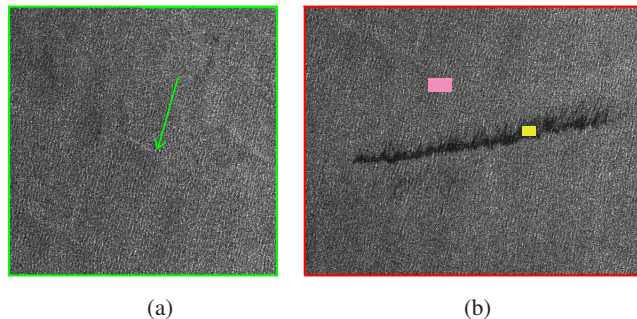


Figure 3.17: Closer look to the sub-scenes of the ERS-1 image. Part (a) is used for wind direction estimation; the estimated direction has been overlapped as a green arrow. Part (b) contains an oil spill. The colored regions correspond to the ROI's selected for class parameter estimation in the supervised algorithm.

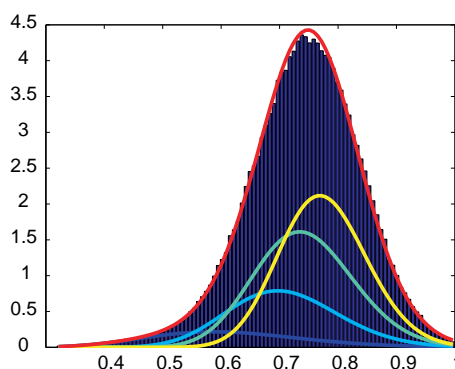


Figure 3.18: Fitting of a mixture of Gammas to the data from the red square in the ERS-1 image.

β -Estimation. The result of the Gamma mixture estimation, in the initialisation of the algorithm, is depicted in Figure 3.18. After only three iterations, both the class parameters and the smoothness parameter have converged. A β value equal to 1.4 was estimated. The segmentation is displayed in Figure 3.19. We also applied Algorithm-2: we selected two ROI's (160 pixels for water and 77 for oil) in the image (shown in Figure 3.17) and computed ML Gamma Estimators for the two classes (see Figure 3.20). We then applied the algorithm and obtained an estimated β value equal to 1.44. The segmentation result is given in Figure 3.21 and is similar to the result obtained with Algorithm-3.

For comparison, we also provide the segmentation obtained with no prior (corre-

3. SEGMENTATION

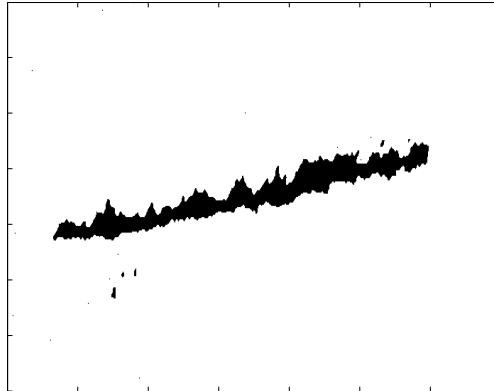


Figure 3.19: Segmentation of ERS-1 subspace containing oil with $\beta = 1.4$, estimated using Algorithm-3 with the Loopy- β -Estimation method.

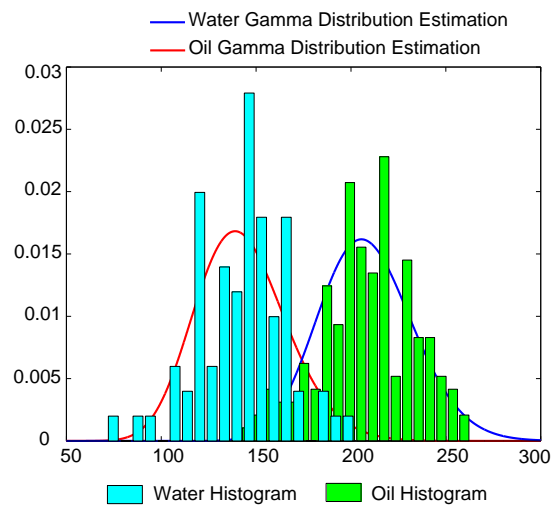


Figure 3.20: Class Parameters Estimation for Algorithm-2.

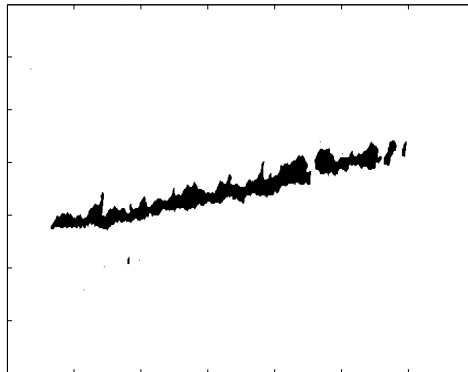


Figure 3.21: Segmentation of ERS-1 subscene containing oil with $\beta = 1.44$, estimated using Algorithm-2.

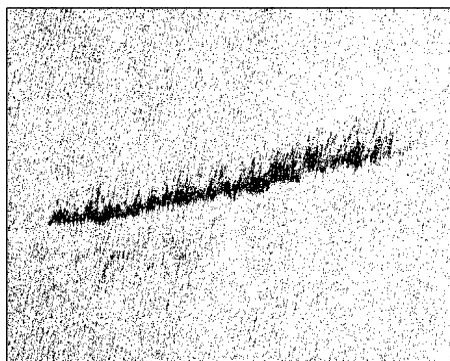


Figure 3.22: Segmentation of ERS-1 subscene containing oil, with $\beta = 0$.

sponding to $\beta = 0$) in Figure 3.22. In practice, the estimated value has proved to deliver a good segmentation. When lower β values were used, the result was noisier and for higher β values, the details of the spill disappeared.

3.7.2.4 Segmentation of an Envisat ASAR IM image using Algorithm-2 and -3

We have also applied Algorithm-2 and Algorithm-3 to the same ASAR Image Mode image used in Section 3.7.2.2 After six iterations, we achieved convergence of the β and θ values. The segmentation result is given in Figure 3.23, corresponding to a estimated $\beta = 1.83$. The unsupervised segmentation result is compared with the one provided by Algorithm-2, where the user provided ROI's for water and for oil that were used to

3. SEGMENTATION

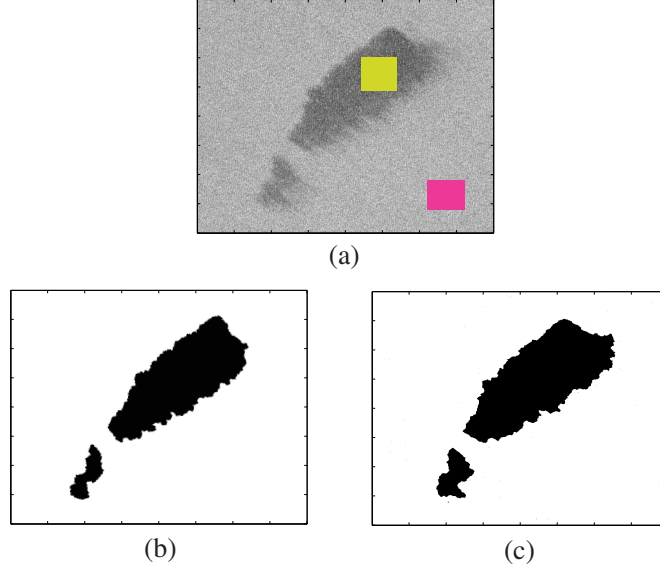


Figure 3.23: (a) ASAR image fragment with colored regions for class parameter estimation in Algorithm-2; (b) Segmentation result applying Algorithm-2; (c) Segmentation result applying Algorithm-3 with Loopy- β -Estimation.

estimate the class parameters at the beginning of the process (see Figure 3.23). In this case a $\beta = 1.75$ was obtained.

3.7.2.5 Segmentation of an Envisat ASAR WSM image using Algorithm-3

In this subsection, we demonstrate the viability of applying Algorithm 3 to an ASAR_WSM scene. We have chosen a very well known image of a confirmed oil spill, namely the Prestige case. This accident took place in November 2002, in Galicia (Spain), when a tanker carrying more than 20 million gallons (around 67,000 tons) of oil split in half off the northwest coast of Spain on 19 November 2002, threatening one of the worst environmental disasters in history. Figure 3.24 shows the location of the acquired scene. This image is freely available from the ESA web pages as SAR sample data, so that it can be easily used for testing and comparing algorithms.

For segmenting the image, we have first partitioned it in tiles of 600×600 pixels and then applied "Algorithm-3" to each one of the tiles independently. No post-processing of the borders or "clean-up" operations, like morphological ones has been carried out.



Figure 3.24: Location of the ASAR Envisat image acquired on the 17th of November 2002 during the Prestige accident in Galicia.

Figure 3.25 shows the most representative part of the ASAR image that has been segmented, namely the part containing the oil spill, and Figure 3.26 shows the concatenation of the segmentation results. As we can see, they are in general very good, with only a discrepancy on the border between some of the tiles.

For initializing the algorithm, the EM Gamma mixture estimation procedure was applied with four modes ($K = 4$). In fact this number is sufficient to provide a good fitting of the intensity data of the SAR image. On the other hand, our EM algorithm allows us to start with a higher mode number, and decreases this number automatically. We depict the results of this fitting on one of the tiles(depicted in Figure 3.27), by showing the histogram of the referred tile with the superimposed estimated Gamma mixture (see Figure 3.28 (a)). As we have explained, the mode corresponding to the lower mean value is assigned to the oil class and the others to the water class, providing an initialization to the class parameters. The estimations of these parameters are actualized along the algorithm and, after nine iterations, we obtain the distributions shown in Figure 3.28 (b).

To fully demonstrate the possibilities of our algorithm, we again run it on the chosen tile, but this time setting the number of classes to $c = 3$. By doing so, we hope to be able to segment a third ambiguous zone, corresponding to intermediate radiometry levels and probably due to atmospheric conditions originating a front. In this case we choose to fit a Gamma mixture of c modes to the data for initializing the

3. SEGMENTATION

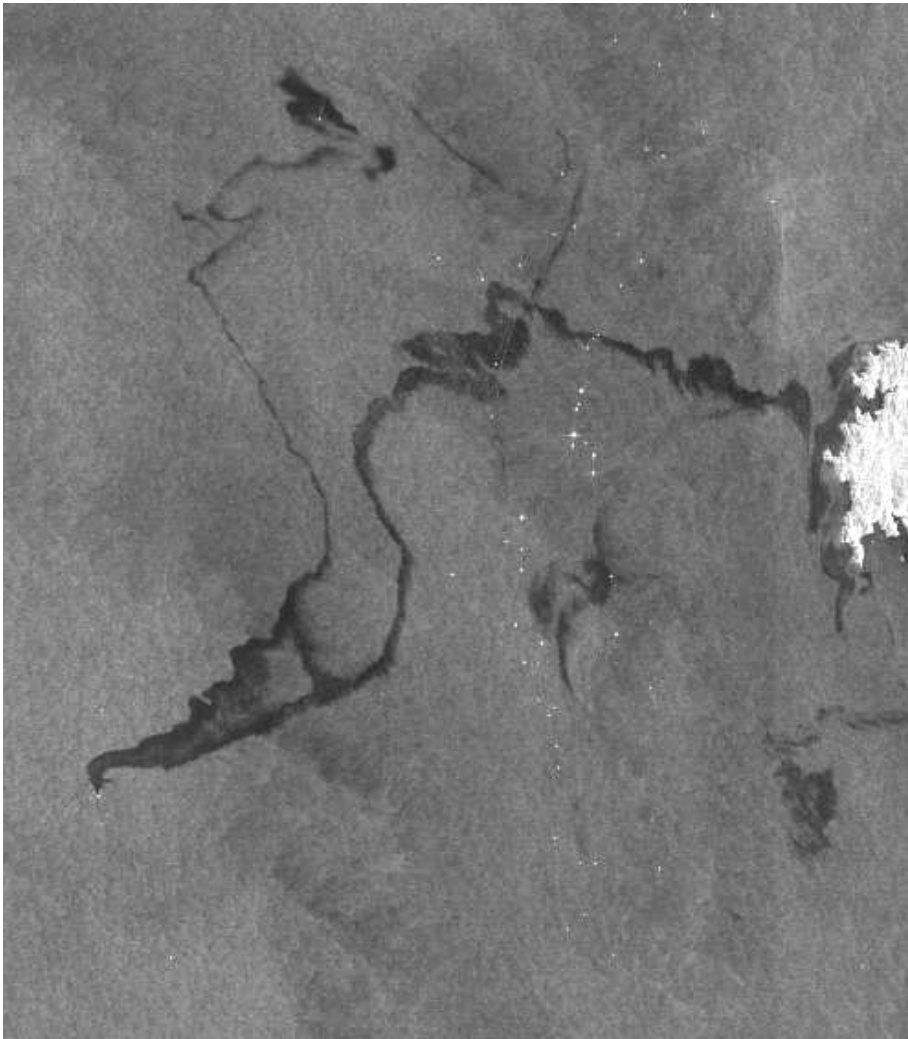


Figure 3.25: Display of the ASA_WSM full resolution image of the Prestige accident.

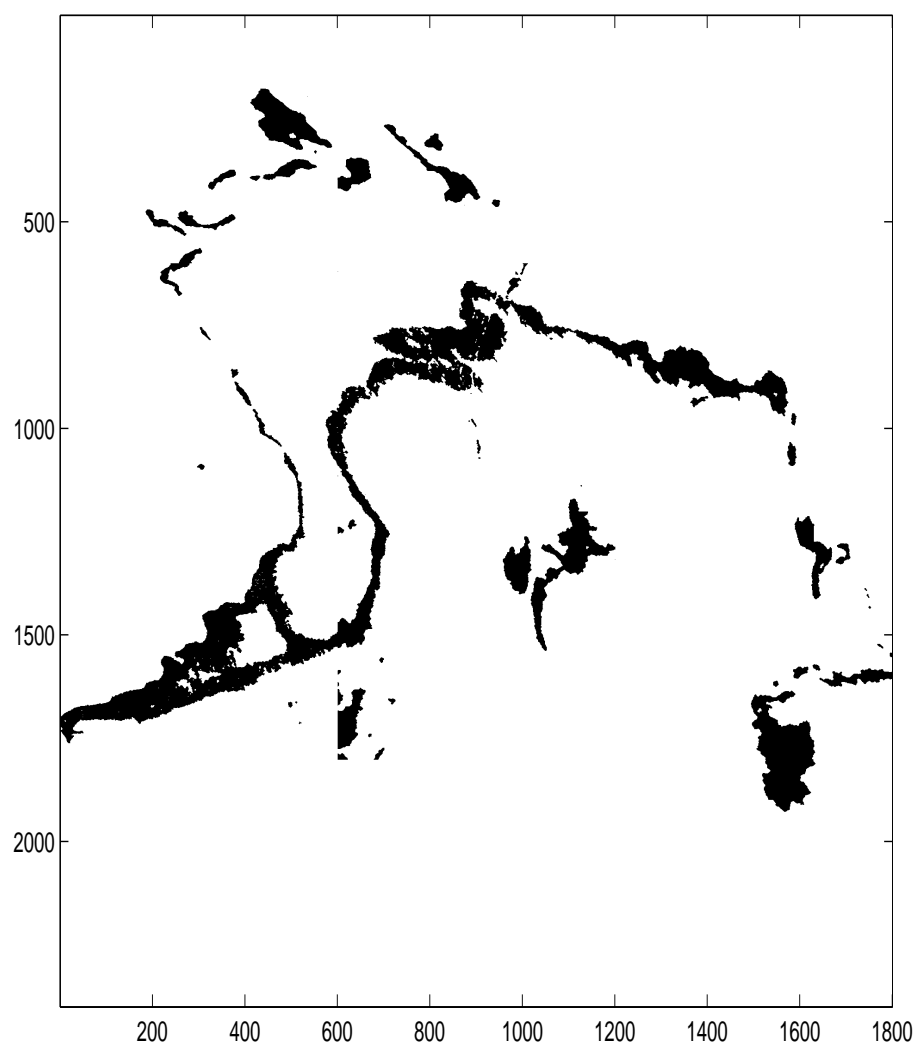


Figure 3.26: Display of the segmentation results of applying Algorithm 3 with Loopy- β -Estimation to Figure 3.25.

3. SEGMENTATION

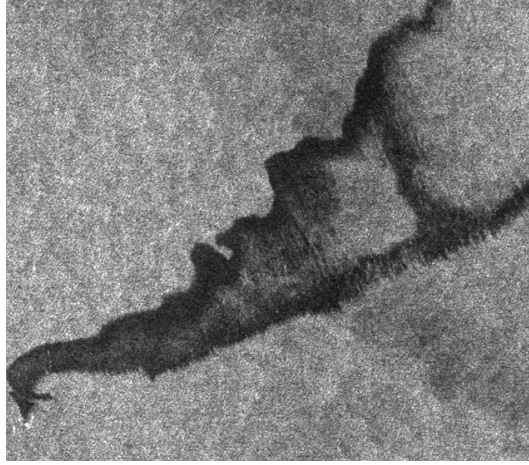


Figure 3.27: Zoom to one of the bottom tiles in which the Prestige ASAR image was divided. This tile has been chosen to provide further details on the algorithm steps.

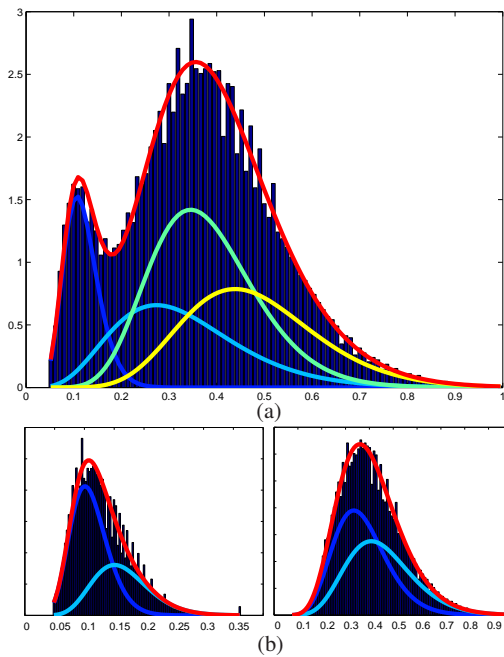


Figure 3.28: Results of applying the EM Gamma mixture estimation procedure to the tile depicted in Figure 3.27: (a) Histogram of the data values (normalized) with superimposed estimated Gamma mixture; (b) Distributions corresponding to the oil class (left) and water class (right) after nine iterations of Algorithm 3: Histogram and superimposed fitting.

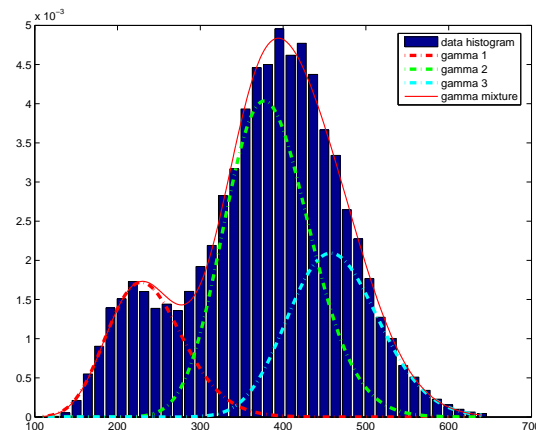


Figure 3.29: Histogram of the data values (normalised) with superimposed estimated Gamma mixture when the number of classes is set to $c = 3$.

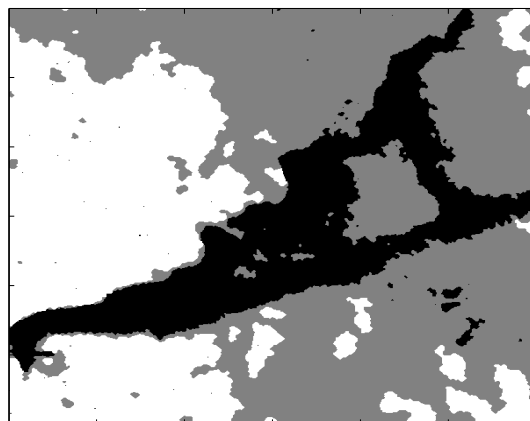


Figure 3.30: Display of the initial segmentation result of applying Algorithm 3 with Loopy- β -Estimation and three classes to the bottom left tile of Figure 17.

class parameters, as depicted in Figure 3.29. With this initialization, the first obtained segmentation using Algorithm 3 is displayed in Figure 3.30. After only nine iterations, all parameters have already converged to the segmentation given in Figure 3.31. When comparing this segmentation with the one provided by a state-of-the-art algorithm, namely by multiscale HMC model in [14], we consider to have obtained a very good result.

3. SEGMENTATION

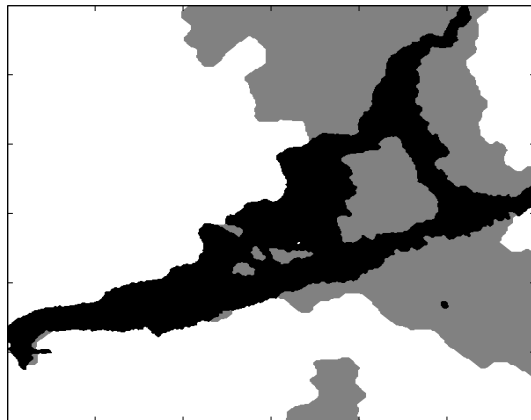


Figure 3.31: Display of the final segmentation result, after nine iterations, of applying Algorithm 3 with Loopy- β -Estimation and three classes to the bottom left tile of Figure 17.

3.7.2.6 Computational Complexity

The proposed algorithms display, in practical cases, a computational complexity of $O(N)$, with N being the number of pixels in the image. In fact, the most time-consuming steps in the algorithms are the α -Expansion and Graph-Cut segmentation routines [68]. These use the max-flow code implementation referred in [80] that has complexity $O(n^{2.5})$ in the worst-case, however, in most situations is $O(N)$. Both Algorithm 1 and Algorithm 3 converge in few iterations and, as an example, for images of the dimension used in the first simulation (64x64) (see 3.7.1.1), only a few seconds are needed to run the algorithms. For a 600x600 pixel tile, like those in the Prestige example in 3.7.2.5, Algorithm 3 is taking ≈ 1 minute, but this time performance could be improved by a more efficient implementation of our procedure, namely by improving the implementation of the Loopy- β -Estimation and by migrating our matlab code fully to C-code.

4

Classification

4.1 Lookalikes: an Overview

As it was already referred to at the beginning of this text, there is a number of oceanographic and atmospheric phenomena that gives rise to dark signatures in SAR images that may very easily be mistaken with oil spill signatures. In this section, we provide some examples of those phenomena. The given list is in no way complete and only some main types of lookalikes are described here. For a deeper and more complete view on this topic, see [3] and [2].

One important aspect of lookalikes is that they are normally local phenomena, related to local features like existing currents or orography. They are often also seasonal, like algae blooms, or ice. In the following, four examples of lookalikes, along a brief explanation of the causes why they are visible in SAR images, is given. One phenomena associated with false positives is bathymetry. They are typically associated with clear lines of high and low backscatter forming tails after the obstacle, if the depth change is abrupt. The origin are currents (usually tidal current), which flow over bottom features like sand banks, causing modulation of surface currents; the Bragg waves pass through these currents and change their amplitudes (illustrated by Figure 4.1 and by Figure 4.2).

Intertidal zones and sandbanks are also characterized by homogeneous dark areas, oft strips of intertidal mud or sand flat. They appear along shallow coastal areas and river mouths and are observed at low tide (see also Figure 4.1).

Upwelling phenomena also appear as dark area in SAR images. Its origin is colder

4. CLASSIFICATION



Figure 4.1: SAR image containing bathymetry signatures, see [1]. This is an ERS-1 image acquired on the 8th July 1995, showing the Subei Shoal off the coast of China (north of Shanghai). The dark areas are the sea areas that have fallen dry during ebb tide.

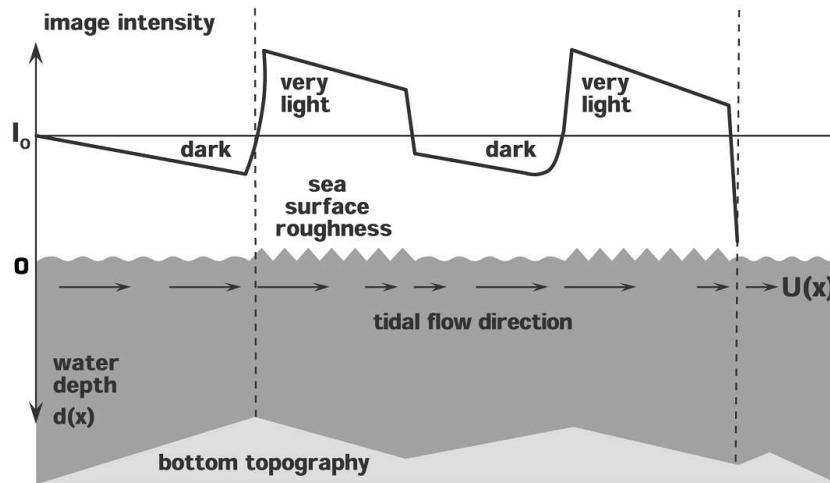


Figure 4.2: Physical explanation of the signature origin of bathymetry structures, see [1].

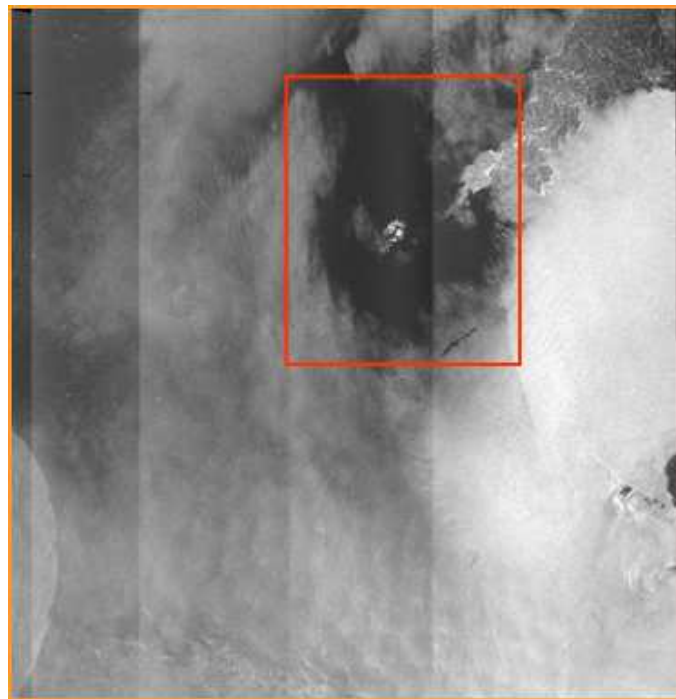


Figure 4.3: SAR image containing upwelling signature around St. Martin island group. The image is an ASAR_WSM acquisition from the 4th of May 2007 at 10:46 (courtesy of Edisoft).

4. CLASSIFICATION

water from deeper water columns ascending to the sea surface. Under certain conditions, water of the upper layer moves away from the coast in either hemisphere and is replaced by water upwelling from below this layer. This typically occurs during Summer in the North and also in the Spring and Autumn for further south. The affected area usually has a larger concentration of nutrients and high biological productivity implying that the amount of surface active substances secreted by marine plants and animals, which float to the sea surface and create there a surface film, are greatly enhanced. Figures 4.3 and 4.4 show an example of an upwelling

As a last example, a case of natural films is displayed in Figure 4.5 can also completely hamper the usability of a SAR image for oil spill detection.

4.2 Classification Methods

In the following, we are mostly using the same notation as in [45]. Our goal is to leverage a set of n training samples in order to design a classifier that is capable of distinguishing between m classes on the basis of an input vector x , where $x = [x_1, \dots, x_d]^T \in R^d$ are simply the d dark patch features. By using the “Leave-One-Out” method, we remove one item at a time from the $n + 1$ element dataset and use the remaining n elements for training the classifier. In our case the dataset contains 140 elements ($n = 140$), we have just two classes ($m = 2$), and $d = 35$ features when wind is considered and $d = 34$ when not. We adopt the common technique of representing the class labels using a “1-of- m ” encoding vector $y = [y^{(1)}, y^{(2)}, \dots, y^{(m)}]$ such that $y^i = 1$ if x corresponds to an example belonging to class i and $y^i = 0$ otherwise. The n training samples that we use in each cycle of the “Leave-One-Out” can thus be represented as a set of training data $\mathcal{D} = [(x_1, y_1), \dots, (x_n, y_n)]$. In each cycle of the “Leave-One-Out”, after training the classifier using the data \mathcal{D} , we test the classifier in the remaining item. The classification results are the mean values of all performed tests.

In this work we have exploited two different approaches:

- Approach 1 (AP1): Apply a feature selection method first and then test different classifiers using the selected features.
- Approach 2 (AP2): Apply a method where feature selection and classification are performed side-by-side, namely the so called Sparse Multinomial Logistic

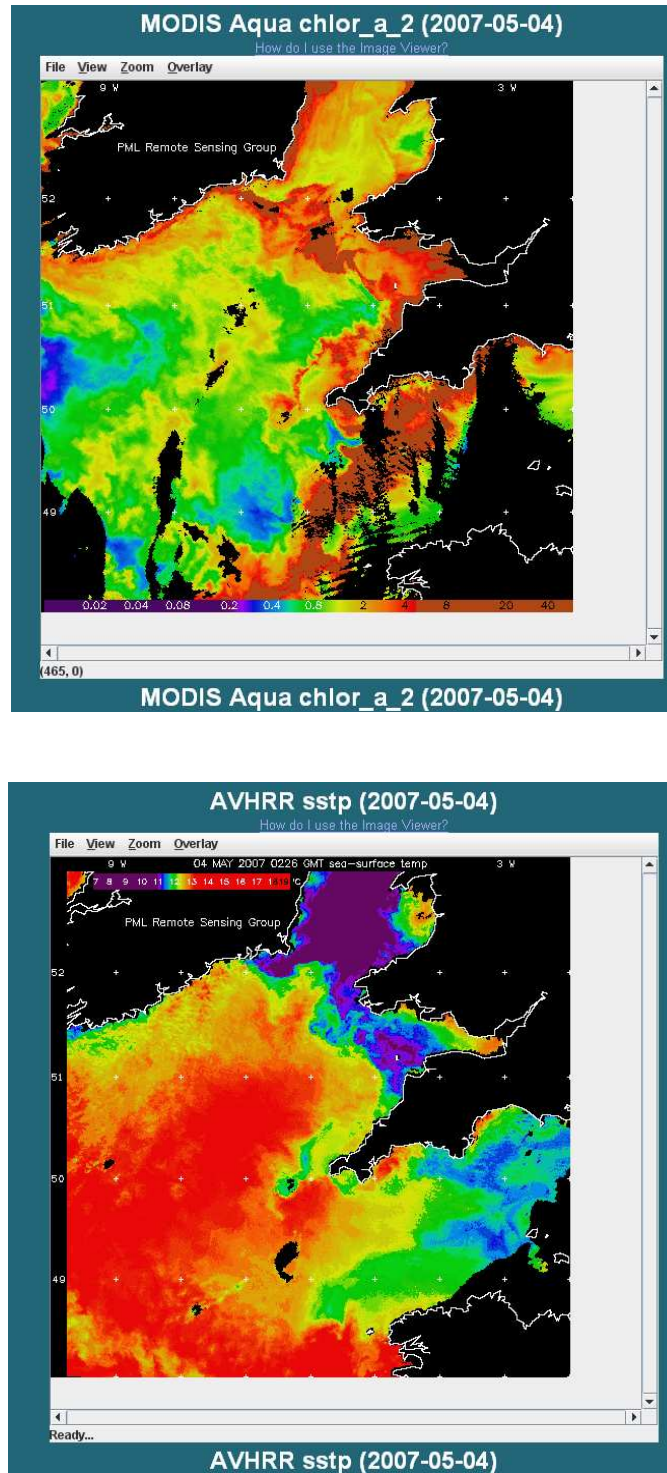


Figure 4.4: Chlorophyll and Sea Surface Temperature (SST) images correlating with SAR signatures (image from the Multi View for UK Waters, from the Plymouth Marine Laboratory).

4. CLASSIFICATION



Figure 4.5: SAR image of the area of the Baltic, see [1]. The sea is partially covered with biogenic slicks that are abundant at this time of the year because of the spring plankton bloom.

Regression (SMLR), (see [45]).

The feature selection step is important because many of the features we have computed are redundant or strong correlated. On the other hand, due to the limited number of samples in our database, using too many features would ultimately cause a decrease of performance due to overfitting.

Feature selection methods essentially divide into wrappers, filters, and embedded methods. Wrappers utilize the learning algorithm of interest as a black box to score subsets of variable according to their predictive power. Filters select subsets of variables as a pre-processing step, independently of the chosen classifier. Embedded methods perform variable selection in the process of training and are usually specific to given learning algorithm (see [81]). Following these definitions we can see that AP1 uses a filter and AP2 an embedded type selection.

We have tested the two approaches in two different scenarios: with and without wind information. By doing so, we intended to assess the true relevance of wind for the classification process. In fact, wind is not always available or its resolution or accuracy is not adequate. Especially in the case of lookalikes, which often occur near the coast, wind speed models do not provide good estimates and SAR extracted values must be taken into consideration with some reserve. Considering these operational constraints, it is of interest to have a quantitative analysis of the importance of wind availability for this problem.

4.2.1 AP1

In AP1, we have tested two different suboptimal feature selection algorithms: the Forward Feature Selection (FFS) (see [81]) method and the Backward Feature Selection (BFS) (see [81]) method. The choice of using suboptimal algorithms was taken considering the computational effort. In a forward selection method one starts with an empty set and progressively adds features yielding to the improvement of a performance index. In a backward elimination procedure one starts with all the features and progressively eliminates the least useful ones.

Both procedures are reasonably fast and robust against overfitting and provide nested feature subsets. However, as we shall see, they may lead to different subsets and, depending on the application and the objectives, one approach may be preferred

4. CLASSIFICATION

over the other one. In particular backward elimination procedures may yield better performances but at the expense of possibly larger feature sets. However if the feature set is reduced too much, the performance may degrade abruptly [64]. In this work, we have used the matlab toolbox PRTools (see <http://www.prtools.org/>), that provides FFS and BFS routines. The evaluation criteria was the sum of the Mahalanobis distances. After the feature selection, we used standard classifiers provided also by PRTools. We have tested the following:

1. Logistic regression (LOGC)
2. Linear Bayes Normal Classifier (LDC)
3. Quadratic Bayes Normal Classifier (QDC)
4. K-Nearest Neighbor Classifier (KNNC)
5. Parzen Windows (PARZENC)
6. Support Vector Machine (SVMC) with a Gaussian Kernel

Logistic regression is adequate when we have a dependent variable y which takes binary values, which is also our case in this work (1:= oil, 0:= lookalike). We then assume that y follows a binomial distribution ($y \sim \text{Bin}(p, n)$), where p is the probability of success (being oil) and n is the number of trials (number of dark patches/samples). The mean value of y is np , and if we normalize the variable it is simply p , taking values between 0 and 1.

The model in logistic regression proposes that we use as dependent variable the logarithm of the odds ratio (so-called logits). Odds are defined as $\text{Odd} := p/(1 - p)$, and logits are given by expression

$$\text{logit}(p) = \ln \left(\frac{p}{1 - p} \right), \quad (4.1)$$

and they are modeled as a linear function of the z_i , the set of explanatory variables (the features), that might inform the final probability:

$$\text{logit}(p) = a + \beta z, \quad (4.2)$$

where a is called the intercept, $\beta = (\beta_1, \beta_2, \dots)$ are called the regression coefficients, $z = (z_1, \dots)$ is the vector of the features z_i and where $p = \Pr(y = 1|z)$.

The logit is then converted into a probability using the following expression (the logistic function):

$$p = \frac{e^{\text{logit}}}{1 + e^{\text{logit}}}. \quad (4.3)$$

The logistic model automatically assures that p is bounded by 0 and 1, which is not the case with normal linear regression. The parameters of the model are a and β and can be obtained for example using Ridge Regression. We used the implementation of the PRTools. An interpretation of the coefficients, in the case of a dichotomous explanatory variable (z_j is 0 or 1), is that odds for group with $z_j = 1$ are $\exp(\beta_j)$ higher, other parameters being equal.

The classifiers used in this work referred to as LDC and QDC are common used Bayesian classifiers. They are based on the prerequisites that we can quantify as a cost the “damage” involved when an object is wrongly classified. A second prerequisite, when using Bayesian classifiers, is that the expectation of this cost can be used as an optimization criteria. The cost function is in our case, where we have two classes, a 2x2 matrix $C(\hat{c}, c_k)$, where c is the class and can take the values c_1 and c_2 .

It can be demonstrated [82] that the expectation of the cost that the classifier assigns a class \hat{c}_i to a measurement vector z (containing the features) which actually corresponds to an object with true class c_k , is

$$R(\hat{c}_i|z) = \sum_{k=1}^K C(\hat{c}_i|c_k)P(c_k|z), \quad (4.4)$$

where K is the number of classes and $P(c_k|z)$ is the posterior probability. This expression is called the conditional risk and by averaging it over all possible all possible measurements we obtain the overall risk, which we would like to minimize in this approach.

As a conclusion, a Bayesian classifier assigns a class $\hat{c}_{Bayes}(z)$ to a measurement vector z , such that

$$\hat{c}_{Bayes}(z) = \operatorname{argmin}_{c \in \mathcal{L}} \{R(c|z)\}. \quad (4.5)$$

4. CLASSIFICATION

The linear and quadratic classifiers used result from further assumptions:

- a uniform cost function is defined, where a unit cost is assumed when an object is misclassified, and zero cost when the classification is correct;
- the conditional probability densities $p(z|c_k)$ are modeled as Gaussian functions.

With the above two assumptions, the classifier is called a quadratic classifier and if we make a further simplification that the covariance matrices in the Gaussian functions are class independent the classifier is called linear.

The K-Nearest Neighbor algorithm is the simplest approach for two-class classification. It is a non-parametric model, which classifies a sample by assigning it the label most frequently represented among the K nearest samples. It uses directly the training set without explicitly estimating probability densities. For classifying a new sample, a distance function is needed to determine which K members of the training set are closest to it. Once the K-nearest training instances have been found, their class assignments are used to predict the class for the new instance, by a majority vote. It can be shown that the performance of the K-NNR approximates the optimum as K increases, but this asymptotic optimality only holds true if the training set is dense. In practice, the demand on the size of the training set is very high, implying increased computational complexity. A suitable choice is to make K proportional to $\sqrt{N_k}$, where N_k is the number of samples belonging to class k [82].

Parzen windows classification is a technique for nonparametric density estimation, which can also be used for classification. It can be regarded as a generalization of the k-nearest neighbor technique. The basic idea is that the knowledge gained by the observation of sample z_i is represented by a function h centered at z_i (the so-called kernel of the estimator) and with an influence restricted to a small vicinity. This function represents the contribution of the observation data z_i to the estimative of the conditional probability $p(z|c = c_k)$. For obtaining the final estimate, all contributions for all training data are summed together [82]. The kernel can be regarded as an interpolation function that interpolates between the samples of the data set. With Gaussian kernels, the weight decreases exponentially with the square of the distance, so far away points are practically irrelevant. The width σ_h of the Gaussian function

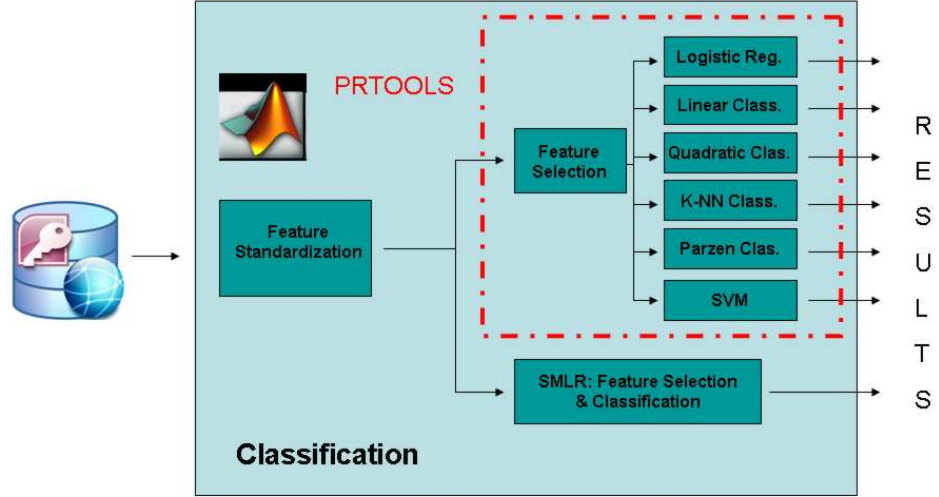


Figure 4.6: This image depicts the main steps undertaken in the Classification, as well as the algorithms and toolbox used.

determines the relative weighting of near and far points and it can be chosen smaller as the number of training samples increases. A classification based on Parzen estimation implies first the determination of the σ_h value. Then, for each sample z in the test set the density for each class is computed:

$$\hat{p}(z|c_k) = \frac{1}{N_k} \sum_{z_j \in T_k} \frac{1}{\sigma_h^N \sqrt{(2\pi)^N}} \exp\left(-\frac{\|z - z_j\|^2}{2\sigma_h^2}\right), \quad (4.6)$$

where N is the number of features and T_k are the subsets into which we partition the labeled training set T_s , each one containing N_k samples, all belonging to class c_k . The sample is assigned to the class with maximal posterior probability:

$$\hat{c} = c_k \text{ with } k = \operatorname{argmax}_{i=1, \dots, K} \left\{ \hat{p}(z|c_i) \hat{P}(c_i) \right\} \quad (4.7)$$

Please refer to [82] for more details on the classifiers and to the documentation of PRTools [83] for details on the implementation.

4. CLASSIFICATION

4.2.2 AP2

The SMLR algorithm is based on multinomial logistic regression and adopts a Laplacian sparsity-promoting prior in order to learn a classifier that incorporates weighted sums of basis functions and results in better generalization capability. Under a multinomial logistic regression model (see [45]), the probability that x belongs to class i is written as

$$P(y^i = 1|x, w) = \frac{\exp(w^{(i)T} x)}{\sum_{j=1}^m \exp(w^{(j)T} x)}, \quad (4.8)$$

for $i \in 1, \dots, m$, where $w^{(i)}$ is the weight vector corresponding to class i and the superscript T denotes vector/matrix transpose. In our case, because we just have two classes the regression is called logistic regression. The weight vector are estimated from the training data \mathcal{D} . To perform maximum likelihood (ML) estimation of w , we would simply maximize the log-likelihood function:

$$l(w) = \sum_{j=1}^n \log P(y_j x_j, w) = \sum_{j=1}^n \left[\sum_{i=1}^m y_j^{(i)} w^{(i)T} x_j - \log \sum_{i=1}^m \exp(w^{(i)T} x_j) \right]. \quad (4.9)$$

On the other hand, $l(w)$ can be made arbitrarily large when the training data is separable, so that we adopt a maximum a posteriori (MAP) estimate, following a Bayesian framework. We introduce a sparsity-promoter Laplacian prior,

$$p(w) \propto \exp(-\lambda \|w\|_1), \quad (4.10)$$

where $\|w\|_1 := \sum_l |w_l|$ denotes the l_1 norm, and maximize the posterior distribution instead:

$$\hat{w}_{MAP} = \arg \max_w L(w) = \arg \max_w [l(w) + \log p(w)]. \quad (4.11)$$

For estimating w , a bound optimization algorithm, described in [45] in detail is used. When applying SMLR, the Laplacian prior forces w to zero or close to zero for many of the entries, resulting in an intrinsic feature selection mechanism. The parameter λ is called regularization parameter and by increasing its value, more components from w tend to zero.

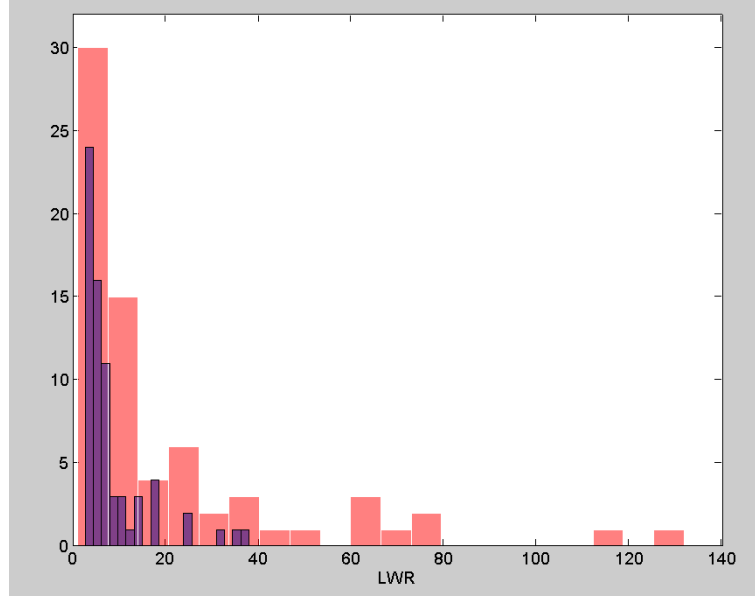


Figure 4.7: Histogram of Length To Width Ratio values; Red=oil, blue=lookalikes.

4.3 Experimental Results

4.3.1 Examples of Extracted Features

In this subsection we illustrate the physical meaning of some relevant features, providing examples from the used data set. One interesting example is the “Length To Width Ratio” (LWR), as many of the detected oil spills originate from discharges of moving vessels, presenting a linear shape. In the empirical guidelines provided to oil spill detection operators, linear shape is considered a strong indication of oil spill. Figure 4.7 depicts the histogram of the LWR values calculated for the data set used in the classification. Figure 4.8 and Figure 4.9 present examples of two dark patches, one oil spill and one lookalike respectively, with very different LWR values.

Another characteristic, which is also used by the operators as an important indication of an oil spill is the so-called “homogeneity of the surroundings”. Guidelines to operators state that an homogeneous area around the dark patch increases the probability that it is an oil spill. One feature which is correlated with this is the “Intensity Standard Deviation Ratio” (ISDR). Figure 4.10 depicts the histogram of the ISDR values calculated for the data set used in the classification. Figure 4.11 and Figure 4.12

4. CLASSIFICATION

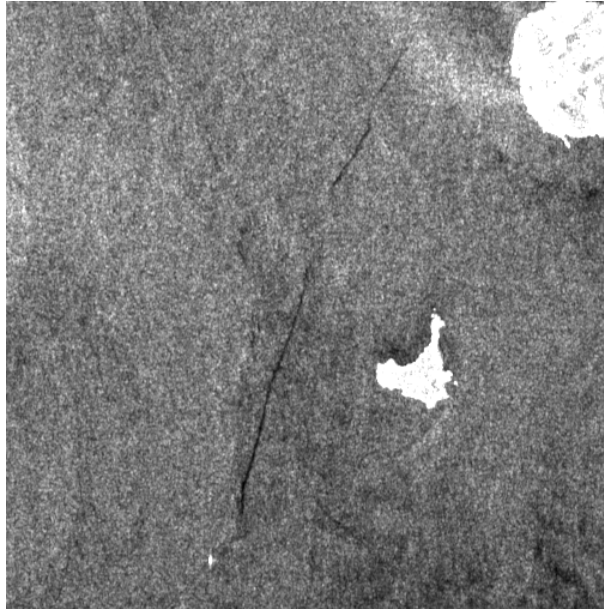


Figure 4.8: Example of oil slick from ongoing discharge of moving vessel, with LWR=118 (Length=30.74 km, Width=0.26 km).

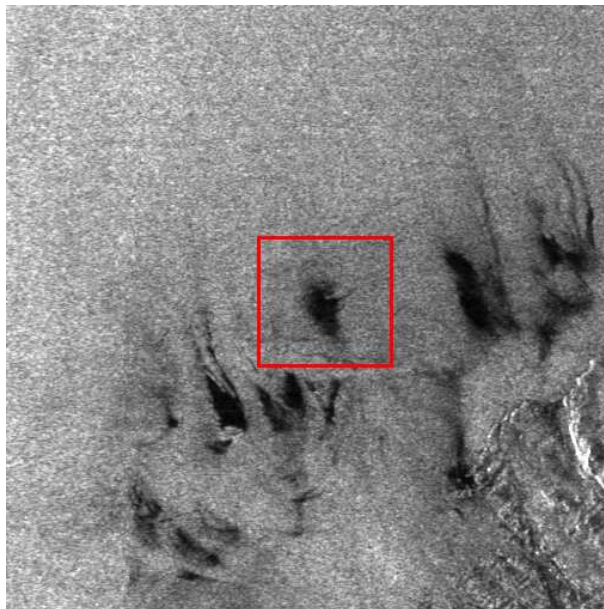


Figure 4.9: Red square: Example of lookalike with LWR=2.7 (Length=3.02 km, Width = 1.1 km).

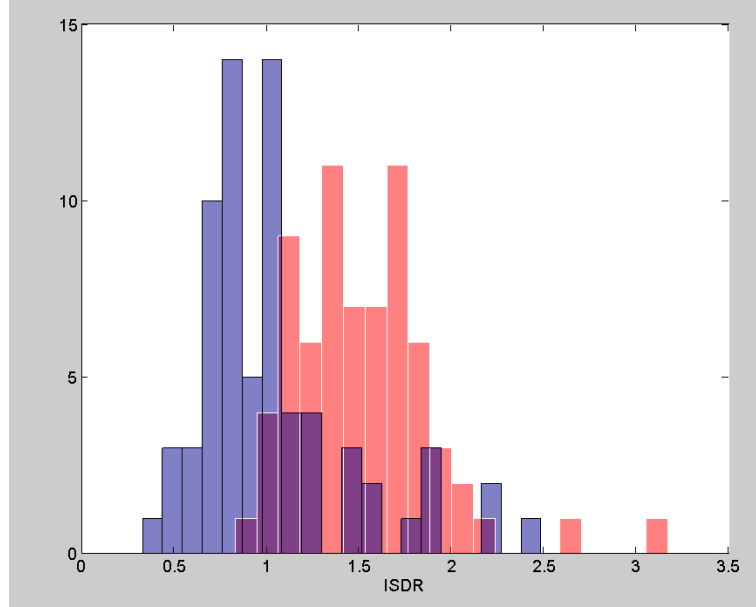


Figure 4.10: Histogram of Intensity Standard Deviation Ratio values; Red=oil, blue=lookalikes.

present examples of two dark patches, one oil spill and one lookalike respectively, with very different ISDR values.

A common reason for inhomogeneous surroundings is the presence of natural films, which disappear by medium to high wind speed. This associated with the fact that low wind areas are also typicall lookalikes, explains why lookalikes are oft linked with low wind speeds, as we can see from Figure 4.13 a certain number of lookalikes are indeed associated with low wind areas.

When the wind is not used as feature, the minimum intensity value of the dark patch (MinObj) is also a good discriminator of lookalikes due to low wind areas.

4.3.2 AP1

We have run the feature selection methods BFS and FFS varying the selected feature set size from 1 to the maximum value (35 when using wind, 34 when not using wind) and applied a number of different classifiers, as described in subsection 4.2.1.

4. CLASSIFICATION

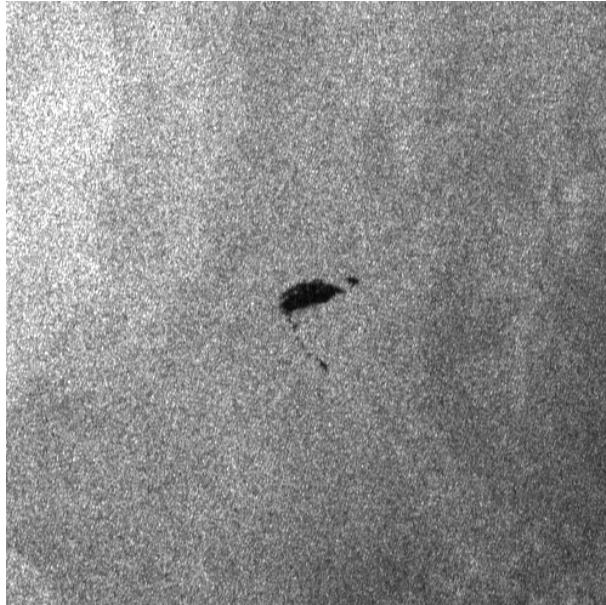


Figure 4.11: Example of oil slick with with ISDR=3.17, corresponding to a very homogeneous surrounding.



Figure 4.12: Example of lookalike with ISDR= 0.33, corresponding to an inhomogeneous surrounding.

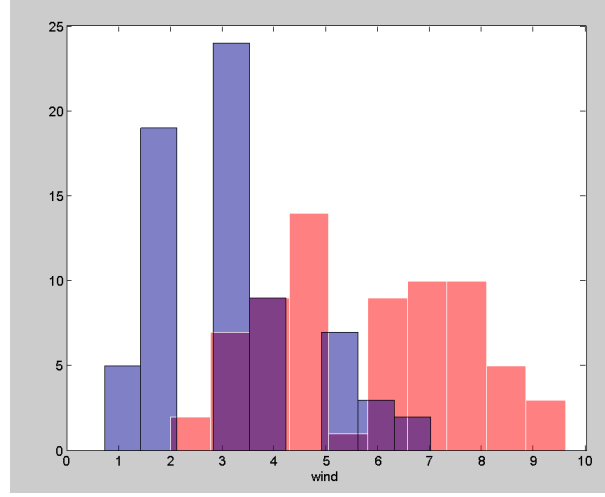


Figure 4.13: Histogram of wind values associated with the lookalikes and oil spills of the data set used for classification; Red=oil, blue=lookalikes.

Table 4.1: Classification Results for AP1 with wind information

Classifier	BFS	FFS
LOGC	OA-test = 96.1 NrFeat = 11	OA-test = 93.1 NrFeat = 9
LDC	OA-test = 97.0 NrFeat = 15	OA-test = 94.1 NrFeat = 19
QDC	OA-test = 93.1 NrFeat = 5	OA-test = 93.1 NrFeat = 15
KNNC	OA-test = 92.2 NrFeat = 3	OA-test = 91.2 NrFeat = 14
PARZENC	OA-test = 92.2 NrFeat = 3	OA-test = 91.2 NrFeat = 5
SVMC	OA-test = 93.1 NrFeat = 9	OA-test = 92.2 NrFeat = 13

4.3.2.1 With Wind

Table 4.1 provides an overview of the obtained results, when wind speed is also used as feature. For the two feature selection methods and for each classifier, the maximum obtained OA-test and the correspondent respective number of selected features is given.

For LOGC and LDC classifiers, the results can be visualised in more detail in Figure 4.14 and Figure 4.15.

From Table 4.1, we can see that a good classification method could be LOGC with 11 features given by BSF feature selection, or LDC with 15 features also given by BSF. The corresponding features for this two methods are given in Table 4.2 , where they are ranked by relevance.

4. CLASSIFICATION

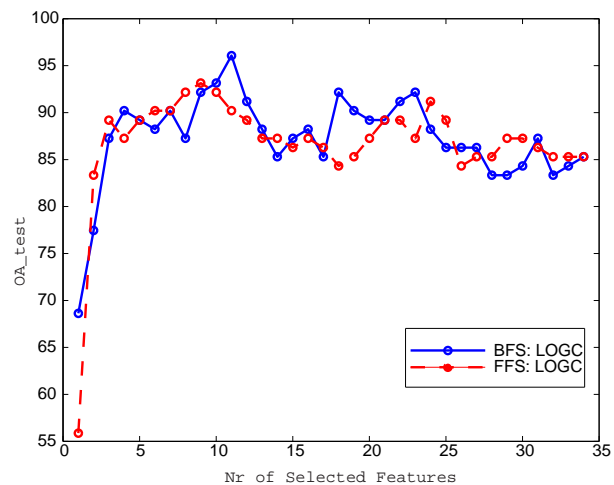


Figure 4.14: Evolution of OA-test with the number of selected features for LOGC classifier using wind information. Comparison between the BFS and FFS feature selection methods.

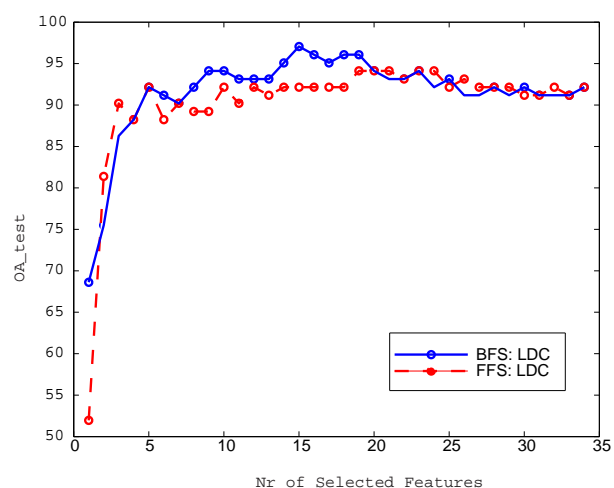


Figure 4.15: Evolution of OA-test with the number of selected features for LDC classifier using wind information. Comparison between the BFS and FFS feature selection methods.

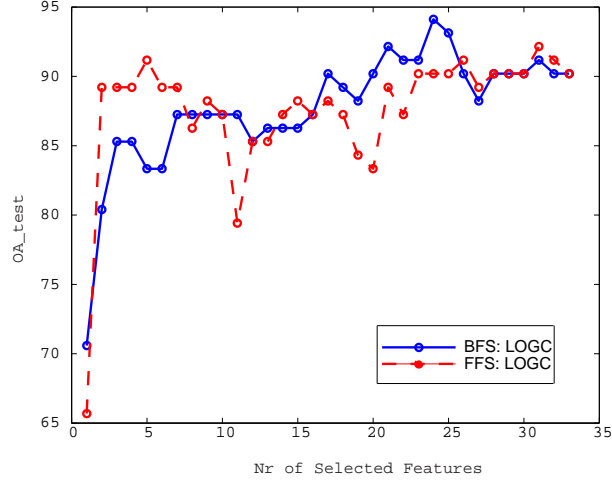


Figure 4.16: Evolution of OA-test with the number of selected features for LOGC classifier when no wind information is used. Comparison between the BSF and FFS feature selection methods.

4.3.2.2 Without Wind

Table 4.3 provides an overview of the obtained results when no wind information is used. For the two feature selection methods and for each classifier, the maximum obtained OA-test and the correspondent respective number of selected features are again given.

For LOGC and LDC classifiers, the results can be visualised in more detail in Figure 4.16 and Figure 4.17.

From Table 4.3, we see that two methods that could be used in this scenario are LDC with 18 features and QDC with 14 features. The number of features needed for LOGC is too high to be accurately estimated using our small sized training dataset. For QDC, the selected features (using BFS) are also listed in in Table 4.2.

4.3.3 AP2

We have run the SMLR algorithm varying the regularization parameter λ and have analysed the overall accuracies measures, as described in Section 1.2. The “OA-train”

Table 4.2: AP1 Best Results: Features selected for LOGC, LDC and QDC - ranked by relevance.

For LOGC (with wind)	For LDC (with wind)	For QDC (without wind)
Max Slick Value	Perimeter	Min Slick Value
Inside Slick Radar Backscatter	Max Slick Value	Max Slick Value
Max Contrast	Outside Slick Radar Backscatter	Intensity Standard Deviation Ratio
Width	Max Contrast	Width
Length To Width Ratio	GLCM Homogeneity	Ellipse-Asymmetry
Wind Speed	Width	GLCM Correlation
Perimeter	Length To Width Ratio	GLCM Dissimilarity
ISRI ISRO Ratio	Wind Speed	ISRI ISRO Ratio
Max Gradient	ISRI ISRO Ratio	GLCM Contrast
Inside Slick Standard Deviation	Max Gradient	GLCM Entropy
Gradient Standard Deviation	Mean Gradient	Mean Gradient
	Gradient Standard Deviation	Outside Slick Radar Backscatter
	Inside Slick Standard Deviation	Perimeter
	Form Factor	Length To Width Ratio
	GLCM Dissimilarity	

Table 4.3: Classification Results for AP1 without wind information

Classifier	BFS	FFS
LOGC	OA-test = 94.1 NrFeat = 24	OA-test = 92.2 NrFeat = 31
LDC	OA-test = 91.2 NrFeat = 18	OA-test = 91.2 NrFeat = 29
QDC	OA-test = 93.1 NrFeat = 14	OA-test = 89.2 NrFeat = 19
KNNC	OA-test = 91.2 NrFeat = 31	OA-test = 92.1 NrFeat = 20
PARZENC	OA-test = 90.2 NrFeat = 11	OA-test = 91.2 NrFeat = 5
SVMC	OA-test = 92.2 NrFeat = 28	OA-test = 94.1 NrFeat = 30

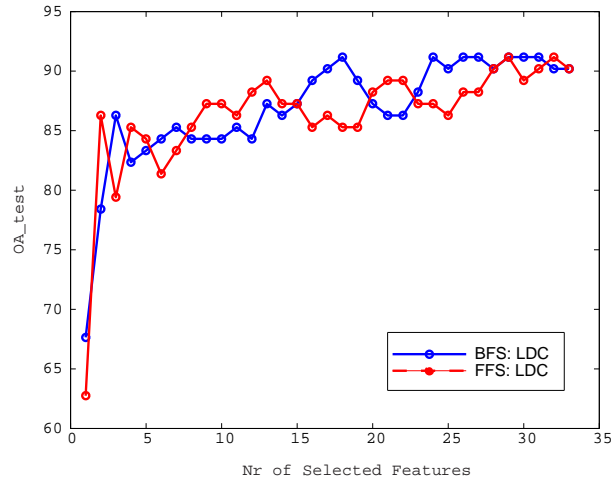


Figure 4.17: Evolution of OA-test with the number of selected features for LDC classifier when no wind information is used. Comparison between the BSF and FFS feature selection methods.

4. CLASSIFICATION

value has been calculated using the same mathematical expression as “OA-test”, but over the training data set instead of over the test elements.

4.3.3.1 With Wind

The algorithm was first applied using all the 35 features, including the wind speed. As we can see from Figure 4.18, we obtain a maximal OA-test value of 93.1 for a parameter value of $\lambda \approx 0.42$. Figures 4.19 and 4.20 show also the evolution of the values “OA-oil”, “OA-lookalike”, “OA-falsePositives” and “OA-falseNegatives” with the regularization parameter. As we can see from Figure 4.21, the value $\lambda = 0.42$ is also assigned to the minimal value of the Bayesian risk, given by expression 4.12, where we are considering the cost function for false positives and false negatives to be the same.

We can also confirm our expectation that an increasing value of λ results in more weight values w_i set to 0, and though to a reduced number of features relevant for the classification process. Figure 4.22 shows this aspect and we see that the value $\lambda = 0.42$ corresponds to 13 relevant weights. This means that only 13 of the estimated weights w_i take values considerably different from 0, as we can see from Figure 4.23, which shows the estimated w for one particular, representative Leave-One-Out cycle of the SLMR algorithm. The image also shows the histogram of the expression $x^T w$, where we can see the clear separation of the two classes, with just a small overlap, accounting for the false positives and negatives. The selected features, ranked by relevance, are listed in Table 4.4.

$$Risk = \frac{OA\text{-fN} + OA\text{-fP}}{2} \quad (4.12)$$

4.3.3.2 Without Wind

We repeated the AP2 procedure but without using the wind feature. The obtained results were very similar to those obtained using wind information: the regularization parameter corresponding to the best OA-test = 92.2 was $\lambda = 0.44$, with 15 relevant features. The selected features, ranked by relevance, are also listed in Table 4.4

Table 4.4: AP2 Best Results: Features selected for SLMR - ranked by relevance.

For SLMR (with wind)	For SLMR (without wind)
Min Slick Value	Compactness
Width	Min Slick Value
Ellipse-Width	Width
Compactness	Ellipse-Width
Wind Speed	ISRI ISRO Ratio
Length To Width Ratio	Inside Slick Radar Backscatter
ISRI ISRO Ratio	Outside Slick Standard Deviation
Intensity Standard Deviation Ratio	Mean Gradient
Mean Gradient	Length To Width Ratio
Complexity	GLCM Entropy
Outside Slick Standard Deviation	Area
GLCM Entropy	Complexity
Area	Gradient Standard Deviation
	Intensity Standard Deviation Ratio
	GLCM Correlation

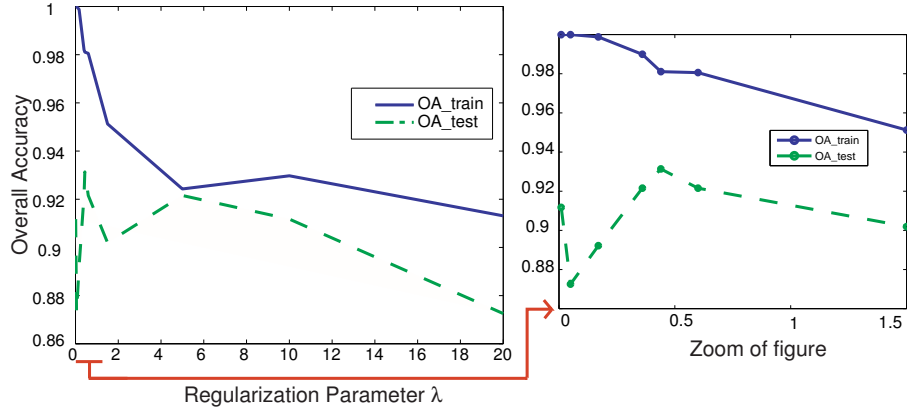


Figure 4.18: OA-test and OA-train from SLMR algorithm versus regularization parameter, when wind information is used.

4. CLASSIFICATION

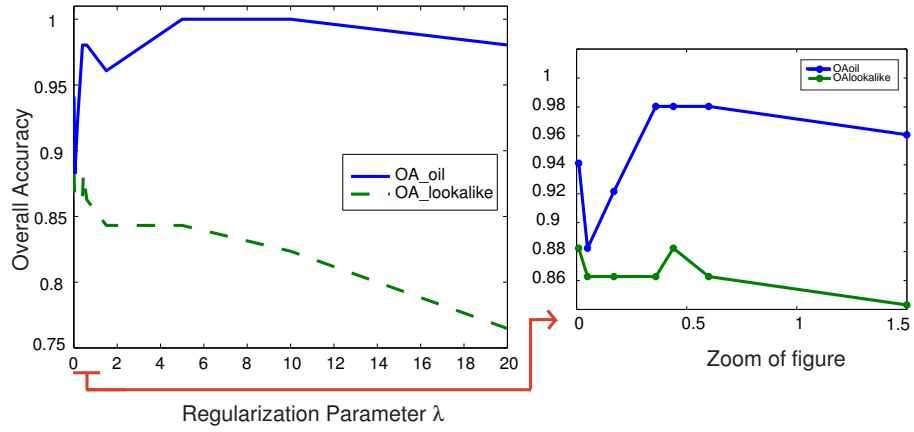


Figure 4.19: OA-oil and OA-lookalike from SLMR algorithm versus regularization parameter, when wind information is used.

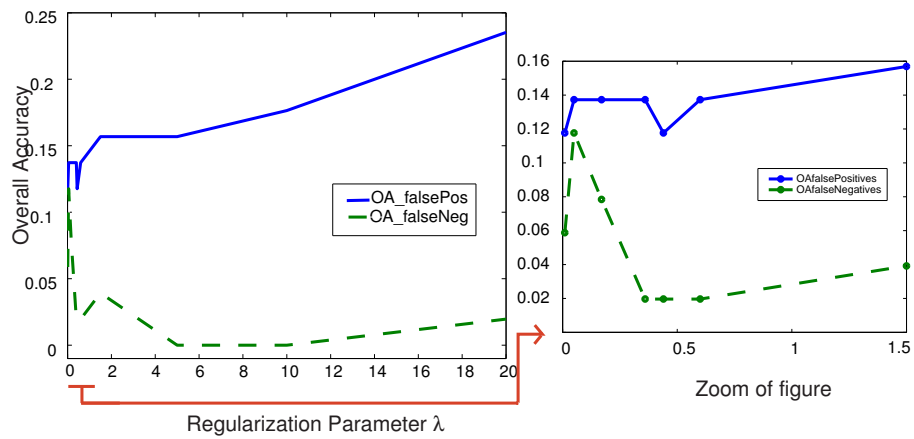


Figure 4.20: OA-falsePositives and OA-falseNegatives from SLMR algorithm versus regularization parameter, when wind information is used.

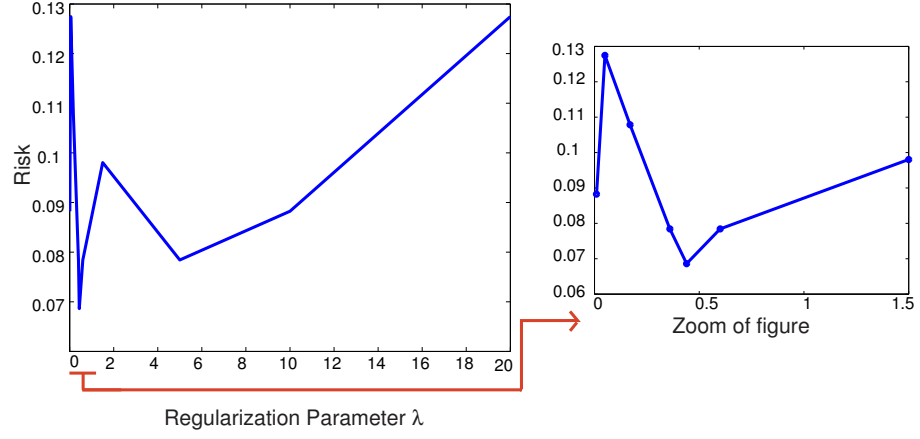


Figure 4.21: Risk versus regularization parameter, when wind information is used.

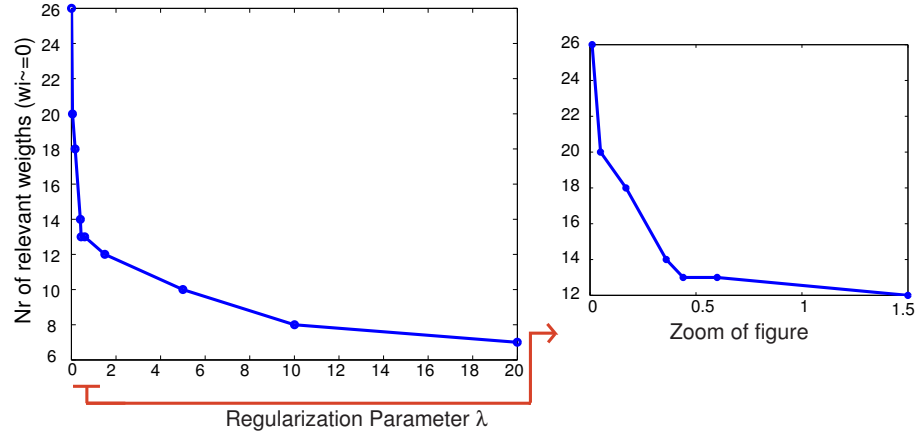


Figure 4.22: Number of Relevant Features ($w_i \neq 0$) versus regularization parameter, when wind information is used.

4. CLASSIFICATION

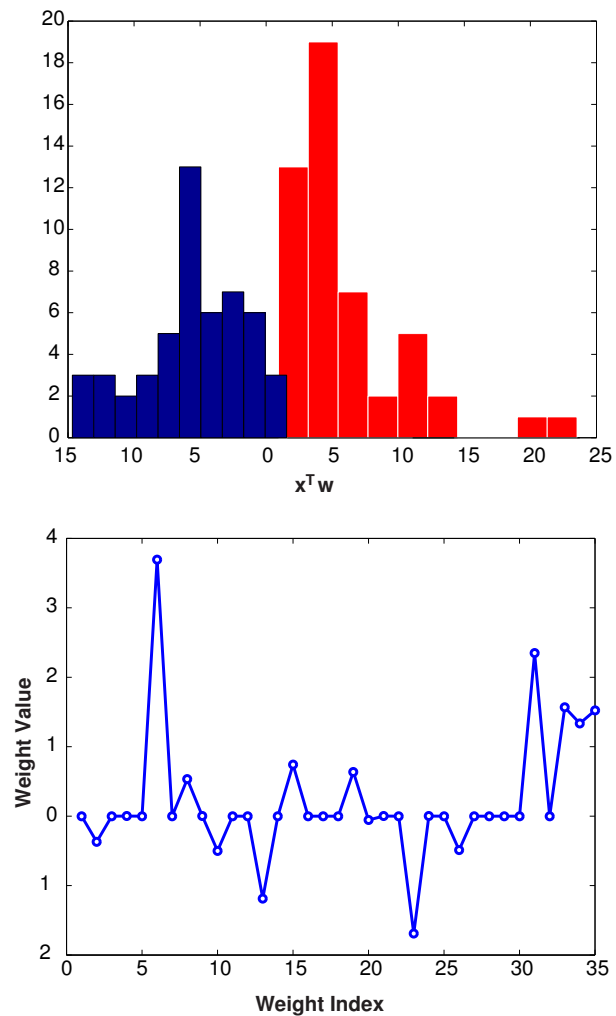


Figure 4.23: Top: Histogram of the expression $x^T w$, displaying a clear separation of the two classes, with just a small overlap, accounting for the false positives and negatives; Down: Estimated w for one particular, representative Leave-One-Out cycle of the SMLR algorithm.

5

Conclusions

5.1 Conclusions on Proposed Methodology for Oil Spill Detection

In what concerns the segmentation step, the results of applying the proposed methodology to simulated images with Gamma data models and to real SAR data are promising. The developed EM Gamma mixture estimation algorithm, when incorporated into the proposed segmentation algorithms, has proved to be an efficient tool for data modeling in SAR intensity images.

With the supervised algorithms, high OA accuracies have been achieved even for simulated images with high levels of noise. In general the Bayesian approach has resulted in an OA increase in the segmentation process between 10 and 15%, when compared to the segmentation using no prior information. Hereby, Algorithm 1 with LSF and Algorithm 1 with CD methods provided similar results, with a performance close to that obtained by setting the β value manually. On the other hand, the LSF estimation procedure seems to become less reliable for noisier images. When compared to Algorithm 2, using Loopy- β -Estimation, we see that this last method always provides equal or better results, outcoming Algorithm 1. Another advantage of Algorithm 2 is that it is usually faster than Algorithm 1, being a one-shot process. Both algorithms, by introducing prior information into the segmentation process, increase the OA significantly. As a conclusion, Algorithm 2 should be preferred to Algorithm 1, when using a supervised method for oceanic SAR images segmentation.

5. CONCLUSIONS

Algorithm 3, totally unsupervised, has been conceived as an improvement to Algorithm 1 and 2. When testing it on simulated data the obtained results were very good, although slightly worst than the supervised ones, as expected. In general, after a few iterations, the class and smoothness parameters converge to stable and meaningful values. By applying Algorithm 3 to real images containing documented oil spills, the segmentation has been considered successful. We could segment both linear and patch type oil spills. Furthermore, the applicability of the method to segment whole scenes, as well as to segment more than two classes, has also been demonstrated in a well known image from the Prestige accident. As a conclusion, we believe the presented methods are suitable to be used for segmenting oceanic SAR images. In particular for oil spill detection, Algorithm 3 seems to be a suitable method.

Based on observations that oil spills in the ocean are often dragged by the wind and align more or less perpendicular to its direction, an interesting future issue is the incorporation of wind information into our segmentation algorithms. By adopting anisotropic MRF in the prior, we intend to reflect this directional dependency of the clique potentials. In the practice, the smoothness parameter β is no longer considered to be a constant value but is clique-dependent according to the wind direction and/or velocity. For estimating the wind profile from the SAR data, state-of-the-art algorithms are used. We have run promising simulations, are currently testing this extension on real data, and expect to obtain interesting results on a near future.

We have tested two different approaches for automatic classification of dark patches in SAR images. For training and testing our algorithms we have first built a 140 dark patch database containing oil spills and lookalikes detected by experienced operators in the framework of the CSN service from EMSA. The used SAR images were from the Envisat satellite, and were of the type Wide Swath. In both approaches we assessed the problem of feature selection: by adopting standard feature selection methods, namely the BFS and the FFS, and then applying standard classifiers and by testing a new algorithm called SMLR, which performs feature selection and classification in parallel. From our results we can draw mainly the following conclusions:

- C1: The AP1 approach delivered the best results, with the highest accuracy corresponding to the LDC and LOGC methods using BFS feature selection (respectively 97.0% and 96.1%).

- C2: BFS delivered always better results than FFS for this particular classification problem.
- C3: The AP2 approach resulted in slightly lower accuracies than AP1 (93.1 instead of 97.0), for a similar number of features, but seemed to be more robust against the absence of wind information. In fact, removing the wind feature only resulted in a decrease of $\approx 1\%$ in the accuracy, and only in an increase of two more features in the final selected features set.
- C4: Wind Speed information used as feature seems to be a value-adding element in classification of oil spills using SAR images. Its use increased accuracy by $\approx 4\%$. In special the AP1 approach, when no wind information was used, required a much higher number of features to obtain comparable results to those when wind information was used.
- C5: We believe there is a clear evidence that automatic classification could be an option to the current semi-automatic procedure used in CSN for Envisat ASAR Wide Swath SAR images.

Although we believe to have obtained very good results when compared to the state-of-the-art in this matter, we recognize the limitation due to the reduced size of our database. In special the analysis regarding the wind relevance for the classification process using AP1 approach should be repeated with more data. In fact, the feature number size required for AP1 without wind was probably too high to be correctly learned from the training dataset. As a main conclusion, we outline that linear classifiers have achieved the best results, indicating that the classes in this problem are linearly separable when using the proposed feature space.

5.2 Perspectives on Oil Spill Detection

Based on the results obtained in this work, we consider that a completely automated operational oil spill detection chain is viable. On the other hand, if other ancillary information is available, a number of possible improvements can be implemented in order to improve the base methodology proposed in this thesis. Especially the use of vessel traffic information could greatly enhance the oil spill detection accuracy. This

5. CONCLUSIONS

could be possible both by adding derived features (like the distance to closest vessel) or by generating so-called risk maps, based on vessel traffic density, that could be incorporated as prior information in the classification methods.

One vessel traffic information source that can provide valuable ancillary data for oil spill detection is the Automatic Identification System (AIS). This is a short range coastal tracking system, operating on the VHF Radio range, used on ships and by Vessel Traffic Services (VTS) for identifying and locating vessels by electronically exchanging data with other nearby ships and VTS stations. Information content of AIS messages include unique identification, position, course, and speed. This information may also be delivered via satellite, in order to overcome the constrain that AIS messages can only be received if vessels are within 40 NM of the AIS network.

Another possible source of vessel information is the Long range identification and tracking (LRIT) system, which was established as an international system on 19 May 2006 by the International Maritime Organization (IMO), is satellite based and also overcomes many limitations of the AIS system, including security issues and coverage limitations.

Furthermore, very recent researches indicate that the use of dual and multipolarisation data for discriminating between oil spills and lookalikes could be a promising technique. Pointing in this direction, there is the work in [84] where a methodology using the so called co-polar phase difference for distinguishing oil spills from biogenic lookalikes was described and demonstrated using TerraSAR-X dual polarisation data.

6

Acronyms

ASAR Advanced Synthetic Aperture Radar

AMI Active Microwave Instrument

AP Alternating Polarisation

BP Belief Propagation

CSA Canadian Space Agency

CSN CleanSeaNet

DHT Directional Hysteresis Thresholding

EEZ Exclusive Economic Zone

EM Expectation Maximization

EMSA European Maritime Safety Agency

ENC Electronic Nautical Charts

EO Earth Observation

EOLI-SA Earth Observation Link Stand Alone

ESA European Space Agency

EU European Union

6. ACRONYMS

FCT Fundação para a Ciência e Tecnologia

GM Global Monitoring

GMES Global Monitoring for Environment and Security

GSHHS Global Self-Consistent High-Resolution Shoreline Database

HMC Hidden Markov Chains

IM Image

ITOPF International Tanker Owners Pollution Federation Limited

MERIS Medium Resolution Imaging Spectrometer Instrument

MDL Maximum Descriptive Length

MODIS Moderate Resolution Imaging Spectroradiometer

MRF Markov Random Fields

NEST Next ESA SAR Toolbox

NRCS Normalized Radar Cross Section

OA Overall Accuracy

OMW Ocean Monitoring Workstation

ROI Region Of Interest

SAR Synthetic Aperture Radar

SST Sea Surface Temperature

WV Wave

WS Wide Swath

Bibliography

- [1] C. R. Jackson and J. R. Apel, *Synthetic Aperture Radar Marine User's Manual*, Commerce Dept NOAA, 2005. 1, 4, 5, 29, 30, 86, 87, 90
- [2] *SAR Ocean Feature Catalogue*, ESA, October 1994. 1, 4, 85
- [3] W. Alpers, "The tropical and subtropical ocean viewed by ers sar," last modified (2009), available at <http://earth.esa.int/applications/ERS-SARtropical>. 3, 30, 85
- [4] *Oil Tanker Spill Statistics:2009*, ITOPF, 2009. 3
- [5] ESA, "Esa oil slick earth watching," available at <http://earth.esa.int/ew>. 3, 30
- [6] *Report on the investigation of the grounding of the vessel CP Valour in Baia da Praia do Norte, Faial, Azores*, MAIB, December 2005. 3
- [7] KSAT, "Satellite detection and identification of possible oil spills," available at <http://www.ksat.no/Downloads/Oil-spill-example.pdf>. 4, 7
- [8] SATLANTIC, "Ocean monitoring workstation," available at <http://www.satlantic.com>. 4
- [9] X. Li et al., "Oil spill response utilizing sar imagery in the gulf of mexico," in *Proceedings of the SeaSAR*, 2010. 4
- [10] R. Solberg A. Solberg, G. Storvik and E. Volden, "Automatic detection of oil spills in ers sar images," *IEEE Transactions on Geoscience and Remote Sensing*, vol. 37, no. 4, July 1999. 7, 11, 12, 35

BIBLIOGRAPHY

- [11] G. Mercier and F. Girard-Ardhuin, “Partially supervised oil-slick detection by SAR imagery using kernel expansion,” *IEEE Transactions on Geoscience and Remote Sensing*, vol. 44, no. 10, pp. 2839–2846, February 2006. 7, 27, 29
- [12] R. Barstow, “Envisat-1 products specification-asar products specification,” *ESA publications*, vol. 8, August 2007. 8
- [13] C. Brekke and A. Solberg, “Oil spill detection by satellite remote sensing,” *Remote Sensing of Environment*, vol. 95, pp. 1–13, 2005. 8, 70
- [14] S. Derrode and G. Mercier, “Unsupervised multiscale oil slick segmentation from SAR images using a vector hmc model,” *Pattern Recognition*, vol. 40, pp. 1135–1147, 2007. 8, 49, 83
- [15] A. Gambardella M. Migliaccio and M. Tranfaglia, “SAR polarimetry to observe oil spills,” *IEEE Transactions on Geoscience and Remote Sensing*, vol. 45, no. 2, pp. 506–511, February 2007. 8
- [16] T. Kanaa et al., “Detection of oil slick signatures in SAR images by fusion of hysteresis thresholding responses,” in *Proceedings of IGARSS*, 2003, vol. 4, pp. 2750–2752. 9
- [17] P. Réfrégier F. Galland and O. Germain, “Synthetic aperture radar oil spill segmentation by stochastic complexity minimization,” *IEEE Geoscience and Remote Sensing Letters*, vol. 1, no. 4, 2004. 9
- [18] S. Y. Wu and A. K. Liu, “Towards an automated ocean feature detection, extraction and classification scheme for SAR imagery,” *International Journal Remote Sensing*, vol. 24, no. 5, pp. 935–951, 2003. 9
- [19] K. Topouzelis, “Oil spill detection by sar images: Dark formation detection, feature extraction and classification algorithms,” *Sensors*, , no. 8, October 2008. 9
- [20] M. Migliaccio A. Gambardella, G. Giacinto and A. Montali, “One-class classification for oil spill detection,” *Pattern Anal Applic*, July 2009. 9, 11, 12, 13, 45

- [21] H. Espedal and T. Wahl, “Satellite sar oil spill detection using wind history information,” *International Journal of Remote Sensing*, vol. 20, no. 1, pp. 49–65, 1999. 11, 12, 32
- [22] R. Holte M. Kubat and S. Matwin, “Machine learning for the detection of oil spills in satellite radar images,” *Machine Learning*, vol. 30, no. 3, pp. 195–215, 1998. 11, 12
- [23] C. Brekke A. Solberg and P. Husøy, “Oil spill detection in radarsat and envisat sar images,” *IEEE Transactions on Geoscience and Remote Sensing*, vol. 45, no. 3, pp. 746–755, March 2007. 11, 12, 71
- [24] J. Lichtenegger F. Del Frate, A. Petrocchi and G. Calabresi, “Neural networks for oil spill detection using ers-sar data,” *IEEE Transactions on Geoscience and Remote Sensing*, vol. 38, no. 5, pp. 2282–2287, September 2000. 11, 44
- [25] F. Del Frate and L. Salvatori, “Oil spill detection by means of neural networks algorithms: a sensitivity analysis,” in *Proceedings of IGARSS 2004*, 2004. 11, 12
- [26] F. Del Frate E. Angiuli and L. Salvatori, “Neural networks for oil spill detection using ers and envisat imagery,” in *Proceedings of SeaSAR 2006*, 2006. 11, 12
- [27] et al. B. Fiscella, A. Giancaspro, “Oil spill detection using marine sar images,” *International Journal of Remote Sensing*, vol. 21, no. 18, pp. 35613566, 2000. 11, 12
- [28] M. Marghany, “Radarsat automatic algorithms for detecting oil spill pollution,” *International Journal of Applied Earth Observation and Geoinformation*, vol. 3, pp. 191196, 2001. 11, 12, 45
- [29] A. Giancaspro W. Biamino E. Parisato R. Ravera F. Nirchio, M. Sorgente and P. Trivero, “Automatic detection of oil spills from sar images,” *International Journal of Remote Sensing*, vol. 26, no. 6, pp. 11571174, March 2005. 11, 12
- [30] F. Nirchio et al., “A generalised algorithm for oil spill detection on ers and envisat sar images,” in *Proceedings of Envisat Symposium 2007*, 2007. 11, 12, 40

BIBLIOGRAPHY

- [31] F. Collard F. Girard-Ardhuin, G. Mercier and R. Garello, “Operational oil-slick characterization by sar imagery and synergistic data,” *IEEE Journal of Oceanic Engineerin*, vol. 30, no. 3, pp. 487-495, July 2005. 11, 12
- [32] C. Cartalis I. Keramitsoglou and C. Kiranoudis, “Automatic identification of oil spills on satellite images,” *Environmental Modelling and Software*, vol. 21, pp. 640-652, 2006. 11, 12
- [33] P. Pavlakis K. Topouzelis, V. Karathanassi and D. Rokos, “Detection and discrimination between oil spills and look-alike phenomena through neural networks,” *Journal of Photogrammetry and Remote Sensing*, vol. 62, pp. 264–270, 2007. 11, 12
- [34] D. Stathakis K. Topouzelis and V. Karathanassi, “Investigation of genetic algorithms contribution to feature selection for oil spill detection,” *International Journal of Remote Sensing*, vol. 30, no. 3, February 2009. 11, 12, 13, 45
- [35] K. Topouzelis D. Stathakis and V. Karathanassi, “Large-scale feature selection using evolved neural networks,” *Proceedings of SPIE*, vol. 65, 2006. 11, 12
- [36] S.Z.Li, *Markov Random Field Modeling in Computer Vision*, Springer-Verlag, Tokyo, 1995. 16, 48, 50, 55, 56
- [37] S. Geman and D. Geman, “Stochastic relaxation, Gibbs distributions and the Bayesian restoration of images,” *IEEE Trans. Patt. Analysis and Mach. Intel.*, vol. PAMI-6, no. 6, pp. 721–741, 1984. 16
- [38] S. YuE M. Berthod, Z. Kato and J. Zerubia, “Bayesian image classification using Markov random fields,” *Image and Vision Computing*, vol. 14, pp. 285–295, 1996. 16
- [39] H. Derin P. Kelly and K.D.Hartt, “Adaptive segmentation of speckled images using a hierarchical random field model,” *IEEE Transactions on Acoustics, Speech, and Signal Processing*, vol. 36, no. 10, pp. 1628–1641, 1988. 16
- [40] G. Vézina H. Derin, P. Kelly and S.G.Labitt, “Modeling and segmentation of speckled images using complex data,” *IEEE Transactions on Geoscience and Remote Sensing*, vol. 28, no. 1, pp. 76–87, 1990. 16

- [41] P.C.Smits and S.G.Dellepiane, “Synthetic aperture radar image segmentation by a detail preserving Markov random field approach,” *IEEE Transactions on Geoscience and Remote Sensing*, vol. 35, no. 4, pp. 844–857, 1997. 16
- [42] N. Laird A. Dempster and D. Rubin, “Maximum likelihood estimation from incomplete data via the EM algorithm,” *Journal of the Royal Statistical Society B*, vol. 39, pp. 1–38, 1977. 16, 53, 56
- [43] W. Freeman J. Yedidia and Y. Weiss, “Understanding belief propagation and its generalizations,” in *Proceedings of International Joint Conference on Artificial Intelligence*, 2001. 16, 48, 58
- [44] C. M. Bishop, *Neural Networks for Pattern Recognition*, Oxford University Press, 1995. 17
- [45] M. Figueiredo B. Krishnapuram, L. Carin and A. Hartemink, “Sparse multinomial logistic regression: fast algorithms and generalization bounds,” *IEEE Transactions on Pattern Analysis and Machine Intelligence*, vol. 27, no. 6, June 2005. 17, 88, 91, 96
- [46] ESA, *ASAR Product Handbook*, February 2007. 19, 21, 23, 24, 25, 26, 28
- [47] Thuy Le Toan, *Advanced Training Course on Land Remote Sensing*, September 2007. 19, 20
- [48] I. Cumming and F. Wong, *Digital Processing of Synthetic Aperture Radar Data*, Artech House, Norwood, MA, 2005. 21, 23
- [49] C. Olmsted, *Alaska SAR Facility Scientific SAR User’s Guide*, July 1993. 22
- [50] J. Johannessen and V. Kerbaol, *Ocean Remote Sensing Training Course 2006-ASAR Principles/Applications*, September 2006. 23, 29
- [51] Canada Centre for Remote Sensing/Natural Resources Canada, “Educational resources for radar remote sensing,” available at <http://geogratis.cgdi.gc.ca/>. 21, 23
- [52] T. Lillesand, *Remote Sensing and Image Interpretation*, John Wiley and Sons, 2004. 23

BIBLIOGRAPHY

- [53] *ERS-1 System*, ESA, September 1992. 25
- [54] MDA, “Essential information solutions: Feature items,” available at <http://gs.mdacorporation.com/news/>. 30
- [55] JRC, “Oceanides database,” available at <http://oceanides.jrc.cec.eu.int/>. 30
- [56] NOWPAP CEARAC, “Oil spill monitoring by remote sensing,” available at <http://cearac.nowpap.org/project/index.html>. 31
- [57] W. Alpers, “Remote sensing of oil spills,” in *Proceedings of the symposium Maritime Disaster Management*, 2002. 32
- [58] T. Elfouhaily K. Katsaros Y. Quilfen, B. Chapron and J. Tournadre, “Observation of tropical cyclones by high resolution scatterometry,” *Journal of Geophysical Research*, vol. 103, pp. 7767-7786, 1998. 36
- [59] Unden et al, *HIRLAM-5 Scientific Documentation*, HIRLAM-5 Project, Norrköping, Sweden, December 2002. 36
- [60] Unidata, “Netcdf documentation,” available at <http://www.unidata.ucar.edu/software/netcdf/index.html>. 36
- [61] B. Rosich and P. Meadows, *Absolute Calibration of ASAR Level 1 products generated with PF-ASAR*, ESA publications, October 2004. 40
- [62] P. Wessel and W. Smith, “A global self-consistent, hierarchical, high-resolution shoreline database,” *Journal of Geophysical Research*, vol. 101, pp. 8741–8743, 1996. 40
- [63] Mryka Hall-Beyer, “The glcm tutorial home page,” available at <http://www.fp.ucalgary.ca/mhallbey/tutorial.htm>. 45
- [64] I. Guyon et al., *Feature Extraction: Foundations and Applications*, Springer, 2006. 46, 92
- [65] T. Silva J. B. Dias and J. Leitao, “Adaptive restoration of speckled SAR images using a compound random Markov field,” in *Proceedings of ICIP*, 1998, vol. 2, pp. 79–83. 47

- [66] R. Garello Y. Delignon and A. Hillion, “Statistical modelling of ocean SAR images,” *IEEE Proc.-Radar, Sonar Navigation*, vol. 144, no. 6, pp. 348–354, December 1997. 47, 50
- [67] N. Johnson and S. Kotz, *Distributions in Statistics: Continuous Univariate Distributions*, Wiley Interscience, 1969. 47, 50
- [68] V. Kolmogorov and R. Zabih, “What energy functions can be minimized via graph cuts?,” *IEEE Transactions on Pattern Analysis and Machine Intelligence*, vol. 26, no. 2, pp. 147–159, February 2004. 48, 52, 84
- [69] Y. Boykov, O. Veksler, and R. Zabih, “Fast approximate energy minimization via graph cuts,” *IEEE Transactions on Pattern Analysis and Machine Intelligence*, vol. 23, no. 11, pp. 1222–1239, 2001. 48, 52
- [70] J. Goodman, *Introduction to Fourier Optics*, McGraw Hill, Boston, 1996. 49
- [71] S. Wang Q. Jiang A. E. Zaart, D. Ziou and G. B. Béné, “SAR images segmentation using mixture of Gamma distributions,” in *Proceedings of Vision Interface*, 1999. 53
- [72] G. McLachlan and D. Peel, *Finite Mixture Models*, John Wiley and Sons, New York, 2000. 54
- [73] José M. Nascimento, *Unsupervised Hyperspectral Unmixing*, Ph.D. thesis, Instituto Superior Tecnico, 2006. 54
- [74] S. Kumar, J. August, and M. Hebert, “Discontinuity preserving surface reconstruction through global optimization,” in *EMMCVPR, LNCS*, 2005, vol. 3757, pp. 153–168. 57
- [75] M. Ibáñez and A. Simó, “Parametric estimation in Markov random fields image modeling with imperfect observations. a comparative study,” vol. 24, pp. 2377–2389, 2003. 59
- [76] L. Younes, “Parametric inference for imperfectly observed Gibbsian fields and some comments on Chalmond’s EM Gibbsian algorithm,” *Probability Theory and Related Fields*, vol. 82, pp. 625–645, 1989. 59

BIBLIOGRAPHY

- [77] L. Younes, “Parametric inference for imperfectly observed Gibbsian fields and some comments on Chalmond’s EM Gibbsian algorithm,” in *Proc. Stochastic Models, Statistical Methods and Algorithms in Image Analysis*, P. Barone and A. Frigessi, Eds., Berlin, Germany, 1991, vol. 47 of *Lecture Notes in Statistics*, pp. 240–258, Springer. 59
- [78] S. Lakshamanan and H. Derin, “Simultaneous parameter estimation and segmentation of gibbd random fields using simulated annealing,” *IEEE Trans. Patt. Analysis and Mach. Intel.*, vol. 11, pp. 793–813, 1989. 60
- [79] S. Deans, *The Radon Transform and Some of Its Applications*, Wiley, New York. 73
- [80] Y. Boykov and V. Kolmogorov, “An experimental comparison of min-cut/max-flow algorithms for energy minimization in vision,” *IEEE Transactions on Pattern Analysis and Machine Intelligence*, vol. 26, no. 9, pp. 1124–1137, 2004. 84
- [81] I. Guyon and A. Elisseeff, “An introduction to variable and feature selection,” *Journal of Machine Learning Research*, vol. 3, pp. 1157–1182, 2003. 91
- [82] F. van der Heijden et al., *Classification, Parameter Estimation and State Estimation*, Wiley, West Sussex, 2004. 93, 94, 95
- [83] R. Duin et al., “Prtools4, a matlab toolbox for pattern recognition,” available at <http://http://www.prtools.org/files/PRTools4.1.pdf>, 2007. 95
- [84] F. Nunziata D. Velotto, M. Migliaccio and S. Lehner, “On the terrasar-x dual-mode for oil slick observation,” in *Proceedings of the SeaSAR*, 2010. 114